

# Geant4 simulations and measurements of the performance of the SAGE spectrometer

Joonas Konki



Pro Gradu  
University of Jyväskylä  
Department of Physics  
December 20, 2011  
Supervisor: Dr. Paul Greenlees



# Acknowledgements

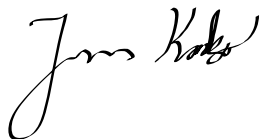
First of all, I would like to thank my supervisor Research Professor, Dr. Paul Greenlees for the endless guidance, answers to my many difficult and confusing questions and problems, and for choosing me to be part of this interesting and challenging project.

I also want express my gratitude to Mr. Daniel M. Cox, Dr. Karl Hauschild, and Dr. Philippos Papadakis for the large amount of work they have done for the simulations of the electron transportation and detection part, the JUROGAM II detectors, and the electromagnetic field simulations, respectively. Without their continuous efforts for the simulations, during the measurements and afterwards, this work would not have been possible at all and especially not in such a short time scale.

Thanks to everyone in the Gamma-RITU research groups and to all who were present in the lab for the experiments. You have all helped in one way or another during the years with the short discussions and information sharing. The comfortable and relaxed working environment would not be possible without the nice colleagues that you all are. Special thanks go to Pauli Peura for helping me to produce the nice 3D plots of the simulated electromagnetic fields, Juha Sorri for inviting me to some nice activities not related to physics (indoor football, snow football tournament etc.) and Panu Rahkila for providing support related to e.g. Grain.

Lopuksi haluan kiittää rakkaita vanhempiani, isovanhempiani, ja siskojeni kaikista neuvoista, loputtomasta tuesta ja kannustuksesta koko elämäni varrella. Suuret kiitokset myös kaikille ystäväilleni ja opiskelijatovereilleni kaikista yhdessä vietetyistä hetkistä ja hauskoista kokemuksista.

Jyväskylä, Finland, December 2011,



Joonas Konki

# Tiivistelmä

SAGE on uusi spektrometri, jonka avulla on mahdollista mitata samanaikaisesti fuusiohöyrystymis-reaktioissa syntyneiden rekyyliytimien viritystilojen purkautuessa emittoituvia konversioelektroneita ja gammasäteilyä. Sisäinen konversio on kilpaileva prosessi viritystilan purkautumiselle tavallisen gamma-hajoamisen kautta, missä konversioelektronit emittoituvat joltain ytimen elektronikuorelta. Konversioelektronit kuljetetaan kohtioalueelta pois keloissa kulkevan suuren sähkövirran muodostaman magneettikentän avulla, ja niiden liike-energia mitataan noin 1 metrin päähän ylävirtaan sijoitetun 1 mm paksun ja 90 osaan segmentoidun pii-ilmaisimen avulla. Pääkelan sisälle asetettu ja muusta järjestelmästä sähköisesti eristetty metallinen sylinterimäinen korkeajännitevälli estää mm. matalaenergisten delta-elektronien pääsyn ilmaisimelle asti, ja vähentää siten haitallista taustaa ja ilmaisimen laskentataajuutta. Tämä on oleellista hiukkassuihkuilla tehtävissä kokeissa, missä suuri laskentataajuus johtuu mm. matalaenergistä sekundaari-, Auger- ja delta-elektroneista sekä jarrutus- ja röntgensäteilystä.

Tähän tutkielmaan liittyen, SAGE spektrometrinä kehitettiin yhteistyössä pienen kansainvälisen ryhmän voimin simulaatio-ohjelmisto C++ ohjelmointikielellä. Apuna käytettiin vapaasti saatavilla olevaa ja laajasti monenlaisiin säteilyyn liittyvissä sovelluksissa hyödynnettyä Monte Carlo -menetelmään perustuvaa Geant4 simulaatio- ja ohjelmointikirjastoa, jonka alkuperä on tunnettu hiukas- ja ydinfysiikan tutkimuslaitos CERN, Sveitsissä. SAGE spektrometrin Geant4 simulaatiossa yhdistettiin nyt ensimmäistä kertaa sen elektronien kuljetukseen ja mittaukseen liittyvät osat ja gammasäteilyn havaitsemiseen käytettävä JUROGAM II ilmaisinjärjestelmä samaan simulaatiokoodiin. JUROGAM II koostuu kahdenlaisista germanium-ilmaisimista sekä niiden ympärillä olevista BGO Compton-suojista. Nämä geometrisesti monimutkaiset ja hankalasti mallinnettavat suojat havaitsevat germanium-kiteistä sironneita fotoneita, minkä vuoksi ne lisättiin myös Geant4 simulaatioon, jotta saadut tulokset vastaisivat paremmin todellisuutta.

Tässä työssä määritettiin kokeellisesti SAGE spektrometrin elektronien havaitsemistehokkuuksia eri energioilla mittaamalla avointa  $^{133}\text{Ba}$ -lähdettä ja gammasäteilyn havaitsemistehokkuuksia kalibroituja ja suljettuja  $^{133}\text{Ba}$ - ja  $^{60}\text{Co}$ -lähteitä käyttäen. Lisäksi osoitettiin korkeajännitevällin toimivuus, ja määritettiin elektronien havaitsemisen tehokkuudet, kun käyttöjännite oli  $-25\text{ kV}$ . Mittauksella osoitettiin myös, ettei kelojen muodostama magneettikenttä vaikuta Compton-suojien valomonistinputkien toimintaan huomattavasti, eikä siten heikennä mitatun gammaspektrin laatua.

Kokeellisten tulosten avulla voitiin arvioida ja varmistaa SAGE:n uuden Geant4 pohjaisen simulaatiokoodin toimivuus vertailemalla eri energioilla mitattuja havaitsemistehokkuuksien arvoja simulaation avulla määritettyihin tehokkuuskäyriin. Tulosten todettiin olevan vertailukelpoisia ja siten simulaation antamia ennusteita voidaan pitää luotettavana. Lisäksi simulaation avulla määritettiin mm. havaittujen elektronien kulmajakaumia, useiden erilaisten elektromagneettisten kenttien ja kohtion paikan vaikutusta havaitsemistehokkuuksiin ja elektronien osumakohtiin ilmaisimessa. Hiukkassuihkuilla tehtävien kokeiden tulosten ennustamista varten simulaatiota on kuitenkin kehitettävä edelleen, ja lisäksi ohjelman antamia tuloksia on niiden luotettavuuden arvioimiseksi verrattava jonkin hyvin tunnetun reaktion tuottamaan mittausdataan.

## Abstract

The SAGE spectrometer combines a solenoidal magnetic field and a 1 mm thick segmented silicon detector with the JUROGAM II array of germanium detectors in conjunction with the RITU separator and the GREAT focal plane spectrometer setup. The magnetic field is used to transport internal conversion electrons produced at the target to the circular silicon detector of 90 individual pixels located upstream from the target. A high-voltage (HV) barrier is used to suppress the low-energy background caused by secondary and delta-electrons. The detector setup allows the prompt gamma rays and internal conversion electrons emitted at the target to be detected simultaneously in singles mode, electron-electron, gamma-gamma and electron-gamma and even triple coincidence modes.

A Geant4 simulation package was developed for the SAGE spectrometer to assist in the fine-tuning of the setup and to give a better understanding of the performance of the detectors. For the first time ever, the electron detection and transport parts were combined together with the JUROGAM II array of germanium detectors and their BGO Compton suppression shields in the same simulation code. The Compton suppression shields are used to veto events by detecting gamma rays that are scattered away from the germanium crystals and only deposit part of their energy. The shields were modelled as accurately as possible in the simulation to make the simulations of gamma-ray detection more realistic.

In this work the results from experimentally measured peak-to-total ratios of the JUROGAM II germanium detectors are compared to the ratios produced by the simulation. Furthermore, it was demonstrated that the magnetic field produced by the solenoid coils does not affect the operation of the photomultiplier tubes in the BGO shields of the Phase 1 detectors located closest to the main coil. The electron detection efficiencies of the SAGE spectrometer were determined from direct measurements of an open  $^{133}\text{Ba}$  source at the target position. The high-voltage barrier was used in some of the measurements, demonstrating that the low-energy electrons were suppressed as is expected when the barrier is working properly. Additionally, the gamma-ray detection efficiency of the JUROGAM II array was determined using sealed  $^{133}\text{Ba}$  and  $^{60}\text{Co}$  sources.

The measured gamma-ray and electron detection efficiencies were compared to the results that were obtained from the Geant4 simulation. This was done to verify that the simulation code is working properly and that it can be used to predict further results and aid in tuning the detector setup for offline experiments. In addition, the simulation was used to determine angular distribution of the detected electrons, and the effect of different field settings and the source location on the focusing of the electron distribution at the detector was investigated. More development is needed in order to use the simulation to predict results from in-beam experiments, and the results should be verified again with measured data from a reaction involving nuclei with well-known level schemes.



# Contents

<b>1</b>	<b>Introduction</b>	<b>1</b>
<b>2</b>	<b>Theoretical aspects</b>	<b>3</b>
2.1	Internal conversion . . . . .	3
2.2	Delta- and secondary electrons . . . . .	4
2.3	Equation of motion of a charged particle in an electromagnetic field . . . . .	6
2.4	The magnetic bottle effect . . . . .	7
2.5	Equations used in this work . . . . .	9
2.6	Error analysis . . . . .	10
<b>3</b>	<b>Experimental methods and apparatus</b>	<b>13</b>
3.1	Description of the measurement equipment . . . . .	13
3.1.1	The JUROGAM II array . . . . .	14
3.1.2	The SAGE electron transport system . . . . .	15
3.1.3	The SAGE silicon detector . . . . .	17
3.1.4	The RITU separator and the GREAT spectrometer . . . . .	18
3.1.5	Electronics and data acquisition . . . . .	19
3.2	Radioactive source measurements . . . . .	20
3.2.1	Measurements of sealed $^{60}\text{Co}$ sources with JUROGAM II . . . . .	20
3.2.2	Measurements of sealed $^{133}\text{Ba}$ and $^{152}\text{Eu}$ sources . . . . .	20
3.2.3	Measurements of an open $^{133}\text{Ba}$ electron source . . . . .	21
<b>4</b>	<b>Simulations</b>	<b>23</b>
4.1	Geant4 – the simulations toolkit . . . . .	23
4.2	Geant4 simulation package of SAGE . . . . .	24
4.2.1	Simulation geometry of SAGE . . . . .	25
4.2.2	Simulating events and a $^{133}\text{Ba}$ source in Geant4 . . . . .	28
4.2.3	Materials, physics lists and Geant4 library versions . . . . .	29
4.2.4	Simulated electromagnetic fields . . . . .	31
4.2.5	Simulation event data analysis tools . . . . .	34

<b>5</b>	<b>Data analysis and results</b>	<b>35</b>
5.1	The gamma-ray detection efficiency of JUROGAM II . . . . .	35
5.2	The efficiency of detecting electrons from a $^{133}\text{Ba}$ source . . . . .	37
5.3	The simulated and measured peak-to-total ratios of the JUROGAM II germanium detectors . . . . .	45
5.4	The effect of the solenoid magnetic field on the performance of JUROGAM II	47
5.5	Simulations of electron distributions at the detector and the effect of passive shielding . . . . .	49
5.6	Simulations of the distribution centroid and the source location . . . . .	51
5.7	Simulated angular distributions of the electrons . . . . .	53
5.8	Simulated detection efficiencies of 0-1000 keV electrons . . . . .	57
5.9	Examples of simulated spectra using realistic detector energy resolutions . .	60
<b>6</b>	<b>Conclusions</b>	<b>63</b>
	<b>References</b>	<b>65</b>



# 1

## Introduction

The SAGE (Silicon And GERmanium) spectrometer [1] combines a solenoidal magnetic field and a 1 mm thick segmented silicon detector with the JUROGAM II array of germanium detectors, that are presented schematically in Figure 1.1. The magnetic field of the solenoid coils is used to transport the internal conversion electrons produced at the target to a circular 90-element silicon detector located upstream of the target. The sizes of the individual pixels have been chosen to handle large count rates of mainly low energy electrons. A high-voltage (HV) barrier of up to  $-50$  kV is used to suppress the low-energy background caused by the secondary and delta-electrons that are produced at the target by the interactions of the ion beam particles with the target material. The detector setup allows the prompt gamma rays and internal conversion electrons emitted at the target to be detected simultaneously in singles mode and coincidence modes. It is a similar but improved design of another electron spectrometer device called SACRED [2, 3] that has been used at JYFL in the past. During in-beam experiments, the SAGE spectrometer is operated in conjunction with the RITU separator [4] and the GREAT focal plane spectrometer setup [5]. The measurement equipment is described in much more detail in section 3.1.

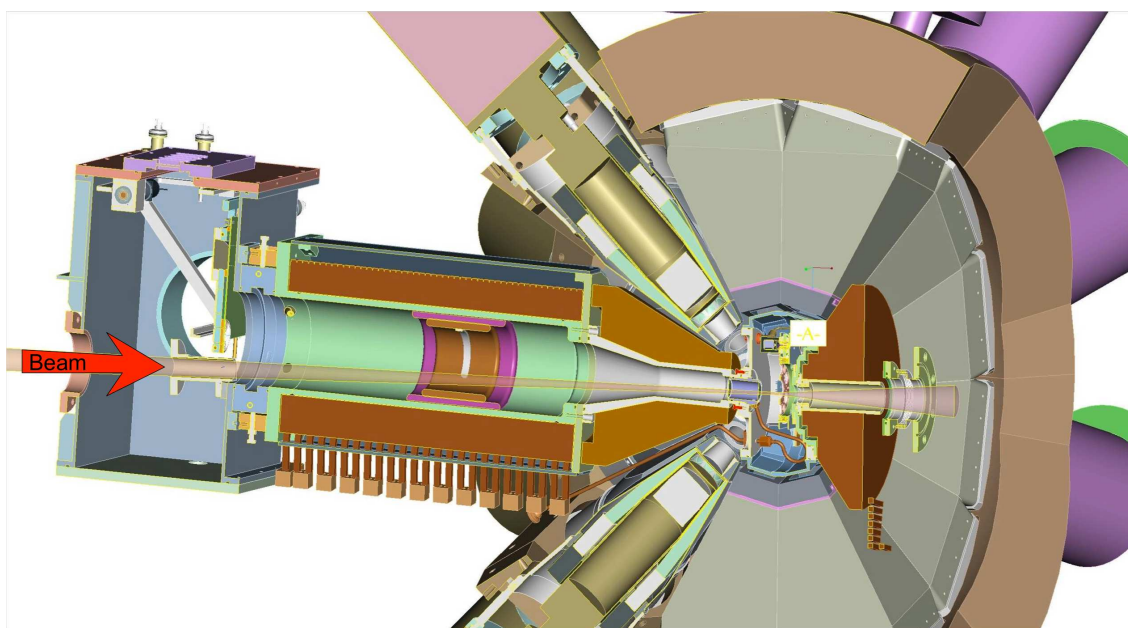


Figure 1.1: A cross-sectional view of the SAGE spectrometer as seen from above. The beam enters from the left next to the segmented silicon detector and inside the solenoid coils, target area is in the middle of JUROGAM II and RITU separator is to the right (not shown). There is a  $3.2^\circ$  angle between the beam and solenoid axes.

The K130 cyclotron at JYFL is used to accelerate the ions produced at the electron cyclotron resonance (ECR) plasma ion sources. The accelerated ion beam is guided to the experiment hall using dipole and quadrupole magnets and finally hits the target material that is placed at the target position. The in-beam experiments impose many challenges on the measurement equipment such as Doppler shifts of energies, energy loss in carbon foils and target material and intense background radiation from delta-, secondary and Auger electrons, bremsstrahlung, gamma rays and X-rays. These difficulties are not present to such an extent in measurements of radioactive sources.

In this work, nuclear reactions involving accelerated ion beams were not studied, only measurements of calibrated radioactive sources emitting electrons and gamma rays in their decays are made. However, the production mechanisms of the electrons are similar in the in-beam experiments. Therefore, the efficiency of a spectrometer like SAGE can be estimated by measuring a radioactive source placed at the target position. A radioactive source was measured using various field configurations, and the analysis of the measured data presented in this work was made by the author. Furthermore, the results obtained from a source measurement can be compared to results produced by a computer simulation that uses an accurate model of the same experimental setup and conditions. In this way, the quality of the simulation program can be evaluated. If the results are consistent, then the simulation can be used to predict and estimate the results of in-beam experiments and the extrapolation is more reliable.

The other part of this work was to participate in the development of a simulation code using C++ programming language and the Geant4 simulations toolkit [6] to simulate the whole SAGE detector setup. This was required in order to assist in fine-tuning the detector setup and to give a better understanding of the performance of the detectors. For the first time ever, the electron detection and transport parts are combined together with the JUROGAM II array of germanium detectors and their Compton suppression shields in the same simulation program that properly supports asymmetric parts in a three-dimensional geometry.

The Geant4 simulation package of SAGE was constructed by combining two earlier Geant4 simulation codes written for the JUROGAM II Phase 1 and Clover germanium detectors by Dr. Karl Hauschild and the model for the SAGE electron transport and detection part done by Mr. Daniel M. Cox. The simulations of the electromagnetic fields produced by the solenoidal coils and the HV barrier were made using the *OPERA 3D* [7] software by Dr. Philippos Papadakis. After the two geometries were combined and the electromagnetic field simulations worked correctly with the particle tracking system of Geant4, the rather complex geometry of the Compton suppression shields for the Phase 1 and Clover detectors were modelled and added by the author to make the simulation more realistic in the detection of gamma rays. Analysis of the event based output data from the Geant4 simulations were made using analysis codes developed by the author. A typical simulation run to produce an efficiency curve for energies 1-1000 keV takes about 8 hours of time from a single CPU. The effective total CPU time used to create the results presented in this work was roughly 150-200 hours. The SAGE Geant4 simulation package is described further in section 4.2

The current developments of the work done for the simulation package in collaboration with the others were recently submitted and are to be included in the conference proceedings of the Rutherford Centennial Conference on Nuclear Physics 2011, in *Journal of Physics: Conference Series* [8].

# 2

## Theoretical aspects

The SAGE spectrometer is used in experiments involving fusion-evaporation reactions to measure the electromagnetic transitions in the reaction products that proceed via emission of gamma rays and internal conversion electrons. These measurements provide a way to probe the complicated microscopic structure of the nuclei. Internal conversion can be the dominant process of de-excitation in heavy nuclei with high  $Z$  in low-energy transitions. Therefore, conversion electron spectroscopy is needed in addition to gamma-ray spectroscopy. Some of the most important theoretical concepts related to the underlying physics and the design of the spectrometer are presented in this chapter.

### 2.1 Internal conversion

The emission of internal conversion electrons [9, 10] (IC, ICE) can happen when a higher energy state of the nucleus decays to a lower state via an electromagnetic transition. An electron is emitted from one of the atomic orbitals of the nucleus. In an electromagnetic transition there is a change in the charge distribution of the nucleus, and the energy of the transition is transferred to the electron. Internal conversion is a completely separate and a competing process of de-excitation to gamma-ray emission, internal pair formation (IPF) above a 1022 keV energy threshold, emission of two gamma rays and other more rare processes. Electric monopole (E0) transitions (a decay of a  $0^+$  state to another  $0^+$  state, or between same spin and parity states  $J^\pi \rightarrow J^\pi$ ) can only proceed via internal conversion. In an E0 transition the emission of one gamma ray is strictly forbidden, because the photon has a spin of unity and angular momentum has to be conserved. The emission of two gamma rays is a higher order process and can be neglected in this discussion.

The internal conversion coefficient (ICC) is often used as a measure of the preferred mode of de-excitation by internal conversion or gamma-ray emission. It is defined as the ratio of the electron emission rate to the gamma-ray emission rate

$$\alpha = \frac{\lambda_e}{\lambda_\gamma}. \quad (2.1)$$

The decay rate is different for different electron shells and the total decay rate can be easily written as a sum of the partial decay rates  $\lambda_i$  corresponding to the different orbitals  $i$  as  $\lambda_e = \sum_i \lambda_i$ . Then the conversion coefficient is a sum of the partial conversion coefficients of the electronic shells

$$\alpha = \frac{1}{\lambda_\gamma} (\lambda_{eK} + \lambda_{eL_I} + \dots) = \alpha_K + \alpha_{L_I} + \dots \quad (2.2)$$

The total decay rate of an excited state can now be written as

$$\lambda_t = \lambda_\gamma + \lambda_e = \lambda_\gamma(1 + \alpha) = \lambda_\gamma(1 + \alpha_K + \alpha_{L_I} + \dots). \quad (2.3)$$

The emitted electron comes from one of the atomic orbitals of the nucleus when the electron interacts with the nucleus. Because the electron orbiting the nucleus in orbital  $i$  is bound with a binding energy  $B_i$ , the kinetic energy of the emitted internal conversion electron is the energy difference between the two states in the nucleus  $\Delta E$  minus the binding energy

$$E_e^i = \Delta E - B_i. \quad (2.4)$$

This means that for a given transition energy the energy of the emitted electron can have different energies depending on the atomic orbital (K, L<sub>1</sub>, L<sub>2</sub>, L<sub>3</sub>, M<sub>1</sub>, ... ) from which it is ejected from.

Usually, in an experiment the internal conversion electrons are emitted from a fast moving ( $\beta = v/c \approx 0.01-0.1$  in fusion-evaporation experiments) recoil nucleus, which means that the measured electron energies are Doppler shifted. The un-shifted electron energy in the rest frame of the recoiling nucleus  $E_e$  can be calculated from the equation [3]

$$E_e = \frac{E_e' + m_e - \beta \cos \theta' \sqrt{E_e'^2 + 2m_e E_e'}}{\sqrt{1 - \beta^2}} - m_e, \quad (2.5)$$

where  $E_e'$  and  $\theta'$  are the shifted electron energy and emission angle measured in the laboratory frame,  $m_e$  mass of the electron (511 keV) and  $\beta$  is the relativistic beta of the recoil  $\beta = v/c$  determined from the reaction kinematics. The angle  $\theta'$  is defined as the angle between the beam direction and the emitted electron.

Due to the design of the SAGE spectrometer it is not possible to determine the exact emission angle of the electron. Instead, an average emission angle  $\theta_{ave}$  can be used. This angle is energy dependent and can be estimated by simulating (or by measuring, which is very difficult) the angular acceptance of the spectrometer i.e. the initial angular distribution of the detected electrons. It should be noted that the angle of the recoiling nucleus is not taken into account in Eq. (2.5). This is justified because the angular acceptance of the RITU separator is about 8 msr, which requires that the recoils that are detected at the focal plane have had to travel in nearly the same direction as the beam into the separator. The maximum angle in the vertical direction is  $\pm 85$  mrad  $\approx \pm 5^\circ$  [11].

## 2.2 Delta- and secondary electrons

When an accelerated high-energy ion beam bombards the target or other material in its path, the vicinity immediately becomes a hostile area for various semiconductor detectors because of the large number of delta- and secondary electrons that are produced when the beam particles interact with the target material. Most of the beam particles do not interact at all with the target nuclei to produce the wanted fusion reactions, but will most likely collide and interact multiple times with the atomic electrons that are orbiting the target nuclei. The electrons that are ejected from the atomic shells via the Coulomb force between the beam nucleus and the electron are called delta-electrons [12, 13, 14].

Usually, the accelerated ion has positive charge, so the force between the ion and electron is attractive and the electron gets a kind of a “sling shot” away from the nucleus. Rather complicated kinematics is involved in solving the maximum energies, trajectories and cross-sections of these events, which can be two-, three- or n-body processes. The collision can also occur in inverse kinematics, where the electron is emitted from the incident beam ion. For heavy ions, heavy target material and high energy beams relativistic effects have to be taken into account in the calculations of the maximum delta-electron energies to properly estimate the high energy delta-electrons that are being emitted in large quantities at the target area. The maximum possible momentum transfer occurs in a so-called binary encounter collision [14, 15].

Binary encounter (BE) occurs when a projectile interacts with an electron of the target in a binary collision that corresponds to a two-body process i.e. a hard and head-on collision. In binary encounter electron emission, the interaction of the target nucleus with the electron is neglected. This can be done because the target is responsible for the initial velocity distribution of the electron, but does not play a major role in the emission process [14]. The simplest model to describe electron emission by charged particles is the Born approximation [16, pp. 371], which is similar to the impulse approximation of classical scattering theory. The Born approximation is obtained from quantum mechanics and perturbation theory and is applicable to weak projectile interactions. The interaction of the electron with the target nucleus is fully taken into account.

The Born approximation describes the binary encounter rather accurately due to the remarkable fact that the treatments of the two-body Coulomb problem give the same results in first-order and higher-order perturbation theory. For strong projectile-electron interactions caused by dressed particles (the shadowing effect of the electrons orbiting the nucleus) this is no longer true. When the projectile velocity is larger than the mean velocity of the bound electron, a binary collision gives rise to a distinct peak in the electron spectrum. The location of the peak is a function of the electron emission angle determined by two-body kinematics. From energy and momentum conservation it is straightforward to obtain the relation that the binary encounter peak has a maximum at an electron energy given by [14]

$$E_{BE} = 4 \frac{m_e}{m_p} E_p \cos^2 \theta_e \quad \text{for } 0 \leq \theta_e \leq 90^\circ, \quad (2.6)$$

where  $m_p$  and  $m_e$  are the masses of the projectile and electron,  $E_p$  the projectile kinetic energy and  $\theta_e$  is the electron emission angle. Equation (2.6) applies to an electron initially at rest. The binary collision peak reduces to a Dirac delta function and yields a single energy for a given angle of ejected electron. The peak vanishes at angles over  $90^\circ$ . The initial electron velocity causes the broadening of the peak and in addition the ejection of electrons at backward angles. Backward emission corresponds to a relatively slow projectile providing a Coulomb field to change the momentum direction of the orbital electron. In the inverse BE process the electrons are elastically scattered by the projectile and they can leave the target atom with a velocity as large as their initial velocity.

Including the initial velocity distribution of the electron one obtains from Born approximation for the BE peak energy the equation [14]

$$E_{BE} = 4 \frac{m_e}{m_p} E_p \cos^2 \theta_e - 2E_b \quad \text{for } 0 \leq \theta_e \leq 90^\circ, \quad (2.7)$$

where  $E_b$  is the ionisation energy.

As an example, to study  $^{254}\text{No}$ , the fusion-evaporation reaction  $^{208}\text{Pb}(^{48}\text{Ca}, 2n)^{254}\text{No}$  can be used, where the  $^{48}\text{Ca}$  beam bombards a  $^{208}\text{Pb}$  target with a beam energy of about 220 MeV chosen to maximise the cross-section of the 2n evaporation channel and suppress the 1n and 3n channels [17, 18]. Using Equation (2.7) in this case gives a maximum energy of the delta-electrons of about 10 keV. It is known from in-beam experiments, that the delta-electrons have much higher energy than this, so these simple theoretical descriptions alone do not reproduce the results from heavy-ion fusion experiments (See e.g. Figure 9 in Kankaanpää et al. [3]).

In addition to the delta-electrons, so called secondary electrons are produced at the target area due to interaction of the beam with the target material. The only difference here is that the emitted electron does not interact directly with the beam ion, but is emitted by interacting with some other “secondary” particle.

In Geant4, the term “secondary electron” means something different. It includes delta-electrons and other electrons that are emitted when a tracked particle loses energy in a medium. The simulation user can define a minimum range for a particle in a material when the secondaries are still produced, which means that when the energy is below the range, it is tracked assuming a continuous energy loss and no extra particles are created [19].

## 2.3 Equation of motion of a charged particle in an electromagnetic field

The operating principles of the SAGE spectrometer and its electron transport system are based on a novel application of many theoretical concepts of electromagnetism and the related dynamics. The dynamics of charged particles moving in electromagnetic fields are covered in detail in the many books of classical electrodynamics [20] and especially in books related to plasma physics and their applications [21]. Nevertheless, some of the basic properties are presented here to give a better understanding of the physical phenomena behind the construction of the spectrometer.

For a charged particle with mass  $m$  and charge  $q$ , the non-relativistic equation of motion of the particle in uniform and time-independent electric  $\vec{E}$  and magnetic  $\vec{B}$  fields is given by [20]

$$m\dot{\vec{v}} = q(\vec{E} + \vec{v} \times \vec{B}). \quad (2.8)$$

If only a uniform and static magnetic field of the form  $\vec{B} = B_z \hat{z}$  is present without an electric field ( $\vec{E} = \vec{0}$ ), we can easily separate the velocity of the particle  $\vec{v}$  into two components:  $\vec{v}_{\parallel}$  parallel to  $\vec{B}$  and  $\vec{v}_{\perp}$  perpendicular to  $\vec{B}$ , such that  $\vec{v} = \vec{v}_{\perp} + \vec{v}_{\parallel}$ . By making these substitutions, Equation (2.8) becomes

$$m\dot{\vec{v}} = q(\vec{v}_{\parallel} \times \vec{B} + \vec{v}_{\perp} \times \vec{B}) = q\vec{v}_{\perp} \times \vec{B}, \quad (2.9)$$

where the fact that  $\vec{v}_{\parallel} \times \vec{B} = (v_z \hat{z}) \times (B_z \hat{z}) = \vec{0}$  has been used. Equation (2.9) is a coupled differential equation for both of the cartesian components of the perpendicular velocity  $v_x$  and  $v_y$  ( $\vec{v}_{\perp} = v_x \hat{x} + v_y \hat{y}$ ), but it can be easily seen and shown [21, pp. 21] that the motion is the gyro-motion where the particle moves in a circle. The centre of this gyro-orbit is called the guiding center.

Adding the parallel velocity component to the description constitutes a helix path, where the guiding center moves along the magnetic field lines of  $\vec{B}$ . The radius of the circular motion in the helix path (Larmor radius) is given by

$$r_L = \frac{m |\vec{v}_\perp|}{|q| B_z}. \quad (2.10)$$

In a relativistic application, the transverse momentum in Equation (2.10)  $\vec{p}_\perp = m\vec{v}_\perp$  has to be replaced with the equivalent relativistic transverse momentum  $\vec{p}_\perp = \gamma m\vec{v}_\perp$ , where  $\gamma = 1/\sqrt{1 - (v/c)^2}$  is the Lorentz factor.

The relativistic equation of motion for a charged particle in a uniform and static magnetic field is

$$\frac{d}{dt}(\gamma m \vec{v}) = q \vec{v} \times \vec{B}. \quad (2.11)$$

The left hand side of Equation (2.11) becomes

$$m \frac{d}{dt}(\gamma \vec{v}) = m \gamma \frac{d\vec{v}}{dt} + m \gamma^3 \vec{v} \frac{(\vec{v} \cdot \dot{\vec{v}})}{c^2} = m \gamma \frac{d\vec{v}}{dt}, \quad (2.12)$$

because  $\gamma$  can be written as  $\gamma = 1/\sqrt{1 - (\vec{v} \cdot \vec{v}/c)^2}$  and for a particle moving in a magnetic field  $\vec{B}$  we get  $\vec{a} = \dot{\vec{v}} = \frac{d\vec{v}}{dt} \perp \vec{v} \Rightarrow \vec{v} \cdot \frac{d\vec{v}}{dt} = 0$ .

Substituting Eq. (2.12) into (2.11) and separating the velocity into parallel and perpendicular components gives almost the same equation as the non-relativistic Equation (2.9), with the only addition being the  $\gamma$  factor. Following a similar derivation as in the non-relativistic case, the relativistic version of the Larmor radius is obtained

$$r_L = \frac{\gamma m |\vec{v}_\perp|}{|q| B_z}. \quad (2.13)$$

As an example, consider a 300 keV electron ( $v/c \approx 0.78$ , relativistic) moving perpendicular to a uniform magnetic field of  $B_z = 0.1$  to 0.15 T. This magnetic field strength roughly corresponds to the value at the silicon detector of the SAGE spectrometer. Substituting these values into Equation (2.13) gives a radius of  $r_L \approx 14$  ( $B_z = 0.15$  T) or 21 mm ( $B_z = 0.1$  T). Inside the main solenoid the field strength is around 0.5 T, giving a radius of about 4 mm. Also the beam ions are influenced by the magnetic field in the same manner, but their velocity is lower, mass is at least 10 000 times larger and  $q$  is larger meaning that the Larmor radius and frequency are greatly reduced.

## 2.4 The magnetic bottle effect

When a particle moves in a non-uniform magnetic field along the z-axis in the direction of increasing magnetic field strength, the radius of its path becomes smaller according to Equation (2.13). This means that the perpendicular velocity  $\vec{v}_\perp$  increases. On the other hand, the total kinetic energy is conserved, which implies that then the parallel velocity component  $\vec{v}_\parallel$  has to decrease. If  $B_z$  becomes high enough, eventually the parallel velocity goes to zero and the particle is reflected back by the magnetic field. This effect is called the magnetic mirror effect.

It is possible to construct a device using a solenoid coil system such that at both ends of the coils the  $B_z$  value is higher than in the middle of the coils. This construction is a trap that confines charged particles between the two maxima of the magnetic field. This is known as the magnetic bottle effect, and is widely used in ion traps and plasma ion sources. In ion sources, the magnetic field is lowered at the other end of the “bottle” to extract ions whenever needed.

It can be shown that the condition for a charged particle to be reflected back by the magnetic field depends on the minimum  $B_z^{\min}$  and maximum  $B_z^{\max}$  strengths of the field and the perpendicular and parallel components of the particle velocity according to the equations [21, pp. 40]

$$\frac{|\vec{v}_{\parallel}|}{|\vec{v}_{\perp}|} < \left( \frac{B_z^{\max}}{B_z^{\min}} - 1 \right)^{1/2} \quad \text{or equivalently} \quad \frac{|\vec{v}_{\parallel}|}{|\vec{v}|} < \left( 1 - \frac{B_z^{\max}}{B_z^{\min}} \right)^{1/2}. \quad (2.14)$$

In the current SAGE electron transport system, solenoid coils are used in such a way that a field profile for  $B_z$  corresponding to that shown in Figure 2.1 is produced in the  $xz$ -plane. A magnetic bottle is formed at the target area that is located at the origin, with the downstream coil making the side closer to RITU (towards  $-z$ ) to have a higher  $B_z^{\max}$ , which means that it is easier for electrons to escape towards the detector. Close to the detector the magnetic field density becomes smaller and the radius of the helix increases. Inside the main coil the  $B_z$  remains roughly constant at around 0.5 T. This type of “bottle” profile is not ideal for electron spectroscopy, but is a consequence of combining the electron spectrometer with the JUROGAM II array.

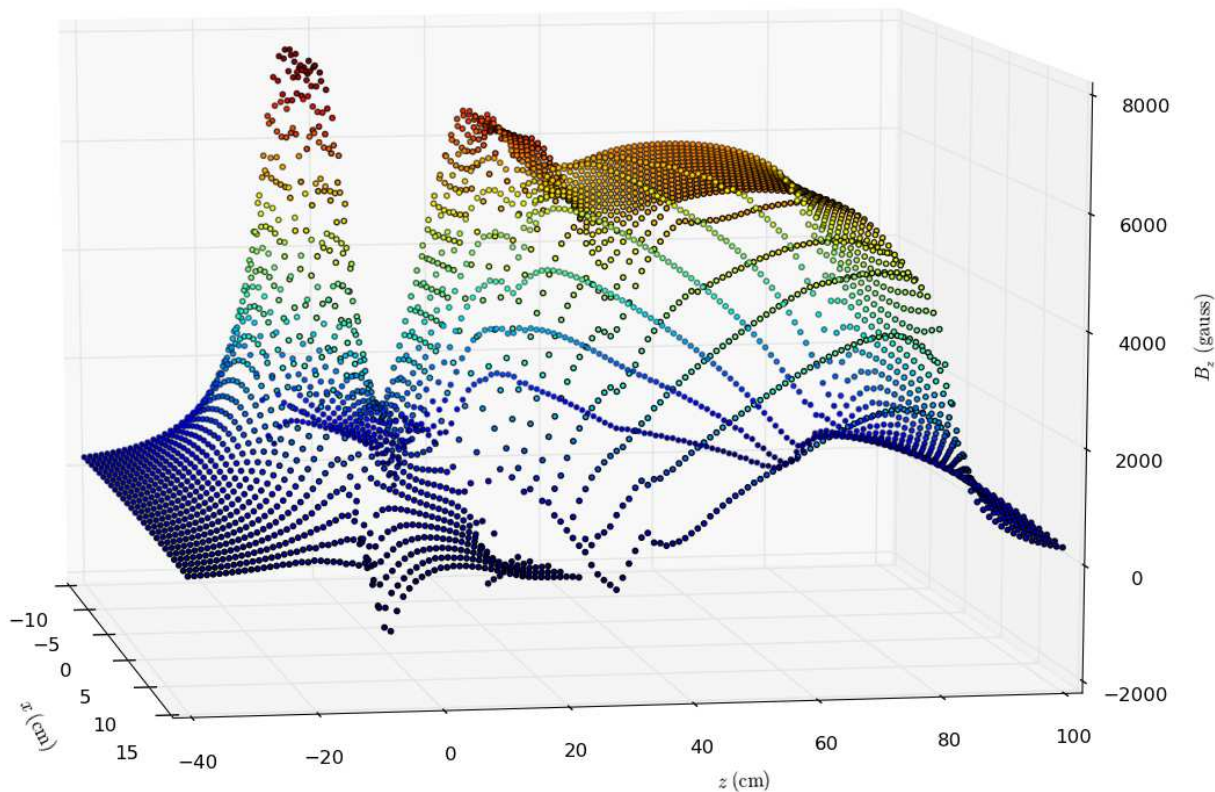


Figure 2.1: Magnetic field strength component  $B_z$  in the  $xz$ -plane at  $y = 0$ . The target is at the origin and the detector at around  $z = 95$  cm at an angle of  $3.2^\circ$  to the  $z$ -axis.



## 2.5 Equations used in this work

The equations that are used in this work to calculate various quantities and the derivations of the corresponding error formulae are presented in this section.

The absolute efficiency of a detector to detect gamma rays or electrons of energy  $E_{\gamma/e}$  from a radioactive source is

$$\epsilon(E_{\gamma/e}) = \frac{N_{E_{\gamma/e}}}{A \cdot \Delta t \cdot I_{\gamma/e}}, \quad (2.15)$$

where  $N_{E_{\gamma/e}}$  is the number of counts in the full energy peak ( $E_{\gamma/e}$ ) in the measured spectrum,  $A$  is the source activity (in Bq),  $\Delta t$  is the measurement time (in seconds) and  $I_{\gamma/e}$  is the absolute intensity of the gamma-ray or electron emission. When calculating the efficiencies from simulations,  $A \cdot \Delta t$  can be replaced with the total number of events (decays)  $N_d$  that were used.

On the other hand, if the efficiency of a detector at energy  $E_{\gamma/e}$  is known, then Eq. 2.15 can be used to determine the activity of a source emitting gamma rays/electrons with the same energy if also the absolute intensity of the transition at that energy is known. The activity is

$$A = \frac{N_{E_{\gamma/e}}}{\epsilon(E_{\gamma/e}) \cdot \Delta t \cdot I_{\gamma/e}}. \quad (2.16)$$

Especially, if two sources are the same (transition intensities are equal), the activity of a calibrated source  $A_{\text{calib}}$  is known, the measurement time is the same and the efficiency of the detector remains the same between the two measurements, the activity of the unknown source  $A_x$  can be solved from Eq. 2.15 to have a rather simple relationship

$$A_x = A_{\text{calib}} \cdot \frac{N_{E_{\gamma/e}}^x}{N_{E_{\gamma/e}}^{\text{calib}}}. \quad (2.17)$$

The activity of a source with initial activity  $A(t = 0) := A(0)$  decays exponentially as a function of time according to the relation

$$A(t) = A(0) \cdot \exp\left(\frac{-\ln 2 \cdot t}{t_{1/2}}\right), \quad (2.18)$$

where  $t_{1/2}$  is the half life and  $A(0)$  is the known activity at time  $t = 0$ . The activity of a calibration source is given with a date when it was determined along with an error estimation by the manufacturer of the radioactive source.

A peak-to-total ratio is a quantity that is defined as the ratio of counts in the measured full energy peak to the total number of counts in the spectrum. It is the usual way to quantitatively describe the spectrum quality obtained with a germanium detector or a large array of detectors. However, there is no clear definition of how the total number of counts should be determined from a spectrum. Especially at low energies the chosen threshold can have an enormous effect on the total number of counts because of noise, low-energy background radiation and other issues.

In some cases the total number of counts is defined as an integral from a low-energy limit of 100 keV to just above the 1332.5 keV peak of  $^{60}\text{Co}$ . This approach is useful if a

lot of noise is present in the low-energy part of the spectrum. In addition to the peak-to-total ratio, it is also possible to use a so called peak-to-valley ratio, which is useful e.g. whenever there are many large background peaks on top of the Compton continuum at lower energies in the spectrum. Any clean part of the Compton continuum (“a valley”) can then be chosen to represent the number of counts in the background instead of the full integral of the spectrum.

The equation for the peak-to-total ratio that is used in this work is

$$(P/T) = \frac{N_{\gamma}^{\text{peak}}}{N_{\gamma}^{\text{total}}}, \quad (2.19)$$

where the total number of counts in the spectrum is chosen to be those above 100 keV and up to 1350 keV.

The weighted average can be used to give one final result if many values for the same quantity  $g$  have been determined, using the errors  $\delta g_i$  as weight. The equation for the weighted average is [22]

$$g_{\text{wav}} = \frac{\sum_i w_i g_i}{\sum_i w_i}, \quad (2.20)$$

where the weights  $w_i$  of the quantities  $g_i$  are given by

$$w_i = \frac{1}{(\delta g_i)^2}. \quad (2.21)$$

The uncertainty of the weighted average in Equation (2.20) is given by

$$\delta g_{\text{wav}} = \frac{1}{\sqrt{\sum_i w_i}}. \quad (2.22)$$

## 2.6 Error analysis

The equations that were used to calculate the errors for the determined quantities are presented here. The law of error propagation [22] is used to derive the equations for the errors of the calculated quantities. If a quantity  $g = g(x_i)$  is a function of independent variables  $x_i$ , the total error of  $g$  is given by [22]

$$\delta g = \sqrt{\sum_i \left( \frac{\partial g}{\partial x_i} \delta x_i \right)^2}. \quad (2.23)$$

By assuming that the error in measuring the duration of the measurement  $\Delta t$  can be neglected (uncertainties in e.g. the source activity and determined peak areas are much more significant), the error for the absolute efficiency (2.15) derived using (2.23) is

$$\delta(\epsilon(E_{\gamma/e})) = \left[ \left( \frac{\delta N}{A \cdot \Delta t \cdot I_{\gamma/e}} \right)^2 + \left( \frac{N \cdot \delta I_{\gamma/e}}{A \cdot \Delta t \cdot I_{\gamma/e}^2} \right)^2 + \left( \frac{N \cdot \delta A}{A^2 \cdot \Delta t \cdot I_{\gamma/e}} \right)^2 \right]^{1/2}. \quad (2.24)$$

In the case of a simulated radioactive source, the activity and measurement time (number of events,  $N_d$ ) can be defined exactly, which means that their uncertainties are zero. This simplifies Eq. (2.24) to

$$\delta(\epsilon(E_{\gamma/e})) = \left[ \left( \frac{\delta N}{N_d \cdot I_{\gamma/e}} \right)^2 + \left( \frac{N \cdot \delta I_{\gamma/e}}{A \cdot \Delta t \cdot I_{\gamma/e}^2} \right)^2 \right]^{1/2}. \quad (2.25)$$

Furthermore, if the intensity is known exactly in the simulation, the only error contribution in the intensity (times the number of events) comes from the random number generator that is used to produce the events according to the pre-defined decay scheme. Modern random number generators used in Geant4 produce realistic distributions, so it is possible to neglect the error in the intensity, as long as the number of events used in the simulation is high “enough”. Now the error for the efficiency becomes

$$\delta(\epsilon(E_{\gamma/e})) = \left( \frac{\delta N}{N_d \cdot I_{\gamma/e}} \right). \quad (2.26)$$

The error for determining the source activity using Eq. (2.18) can be estimated by applying again the law of error propagation (2.23). The uncertainties of the half life and the elapsed time since the time the source was calibrated can be neglected, because the uncertainty in the initial activity  $\delta(A(0))$  dominates, and the following equation is obtained

$$\begin{aligned} \delta A(t) &= \left[ \left( \frac{\ln 2 \cdot A(0) \cdot \delta t}{t_{1/2}} \right)^2 + \left( \frac{\ln 2 \cdot A(0) \cdot t \cdot \delta t_{1/2}}{t_{1/2}^2} \right)^2 + (\delta A(0))^2 \right]^{1/2} \cdot \exp\left(\frac{-\ln 2 \cdot t}{t_{1/2}}\right) \\ &\approx \delta A(0) \cdot \exp\left(\frac{-\ln 2 \cdot t}{t_{1/2}}\right). \end{aligned} \quad (2.27)$$

For the peak-to-total ratio in Equation (2.19), the equation for estimating the error derived from the law of error propagation (2.23) is simply

$$\delta(P/T) = \left[ \left( \frac{\delta(N_{\gamma}^{\text{peak}})}{N_{\gamma}^{\text{total}}} \right)^2 + \left( \frac{N_{\gamma}^{\text{peak}} \cdot \delta(N_{\gamma}^{\text{total}})}{N_{\gamma}^{\text{total}^2}} \right)^2 \right]^{1/2}. \quad (2.28)$$



## Experimental methods and apparatus

All the measurements described in this work were performed at the Accelerator Laboratory of the Physics Department (JYFL) at the University of Jyväskylä, Finland. The SAGE spectrometer setup is located there at one branch of the beam line with a gas-filled separator and a focal plane detector setup. The experimental methods and equipment used in the measurements for this work, and the apparatus used in real in-beam experiments that are closely related to the SAGE spectrometer are shortly described in the next sections.

### 3.1 Description of the measurement equipment

The measurements in this work are made to determine the experimental electron detection efficiency of the SAGE spectrometer, and to verify the results given by the Geant4 simulation package developed for SAGE. The experimental efficiency is obtained from a direct measurement of a radioactive source. Further verification of the simulation package can be done in by comparing to results from in-beam experiments involving nuclei with well-known level schemes and intensities of the internal conversion electrons.

A schematic representation of the whole detector system is shown in Figure 3.1, to aid description of the experimental setup in the following sections.

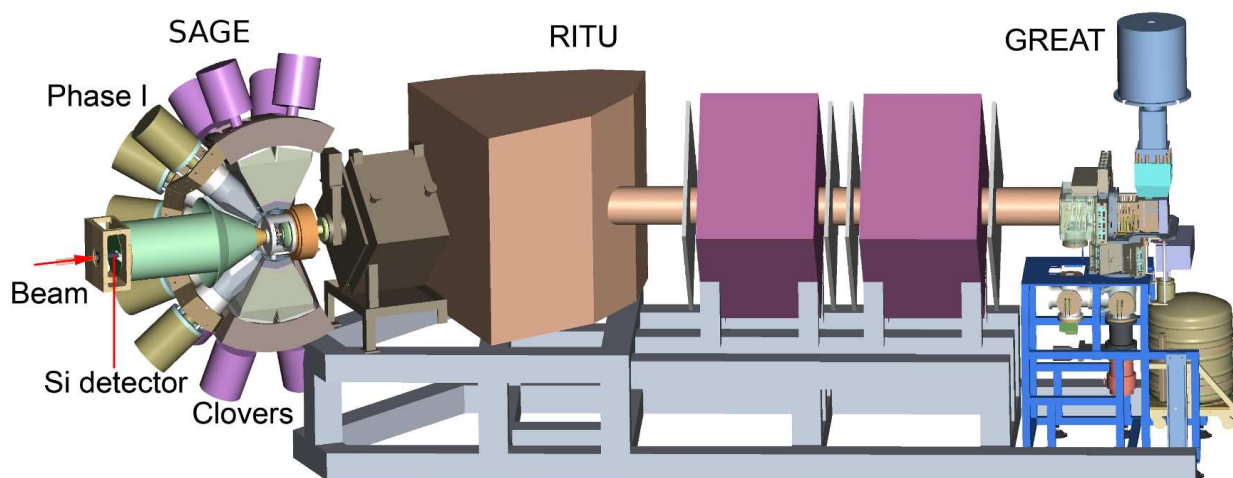


Figure 3.1: A schematic representation of the complete detector setup showing the SAGE electron and gamma-ray detectors in conjunction with RITU and GREAT. Image source: [1]

### 3.1.1 The JUROGAM II array

The prompt gamma-rays that are emitted at the target area in the experiments are detected with the JUROGAM II array. It is a recent upgrade to the previous JUROGAM array made in 2008, which now consists of 15 Phase 1 and GASP type detectors [23] (tapered) and 24 Clover detectors [24] that originate from the European EUROBALL arrays [25, 26]. All of the germanium detectors are equipped with Compton suppression shields made of bismuth germanate (BGO), and Hevimet<sup>1</sup> collimators are placed in front of the detectors.

The Clover detectors consist of 4 germanium crystals inside one cryostat, and they are placed in two rings around the target chamber at an angle of almost 90° with respect to the beam axis to reduce the Doppler broadening due to the smaller detector opening angles. The Phase 1 detectors are also placed in two rings of 10 and 5 detectors at the upstream side of the target chamber. However, in order to fit the mechanical structure of the SAGE electron transport system and the solenoid coils close to the target, the smaller ring of 5 Phase 1 detectors have to be removed. This also means that a small sacrifice of the gamma-ray detection efficiency has to be made. The angles of the detectors in the array are presented for the Phase 1 detectors in Table 3.1 and in Table 3.2 for the Clover detectors.

Table 3.1: The Phase 1 detector (T = tapered) angles in the JUROGAM II array. The angles are midpoint angles,  $\theta$  is defined with respect to the beam direction and  $\phi = 0$  is defined as vertically upwards, increasing in a clockwise direction when the array is viewed from a position upstream of the target.

Detector position	$\theta$ (°)	$\phi$ (°)
T01	157.6	0
T02	157.6	72
T03	157.6	144
T04	157.6	216
T05	157.6	288
T06	133.57	18
T07	133.57	54
T08	133.57	90
T09	133.57	126
T10	133.57	162
T11	133.57	198
T12	133.57	234
T13	133.57	270
T14	133.57	306
T15	133.57	342

In this work all the simulated and measured results for JUROGAM II are given with 24 Clover and 10 Phase 1 type detectors, as is the case whenever the electron detection and transport systems of SAGE are in use. For the full array including the additional first ring of 5 Phase 1 type germanium detectors, the efficiencies are slightly improved.

<sup>1</sup>Hevimet is a metallic alloy of 95% W (tungsten), 3.5% Ni (nickel), 1.5% Fe (iron) with a density of about 17.0 g/cm<sup>3</sup>.

Table 3.2: The Clover detector (Q = Clover) angles in the JUROGAM II array. The angles are midpoint angles,  $\theta$  is defined with respect to the beam direction and  $\phi = 0$  is defined as vertically upwards, increasing in a clockwise direction when the array is viewed from a position upstream of the target. The Clover detector crystals - a,b,c,d (blue, black, green, and red respectively) - are arranged in a clockwise fashion when viewed from the dewar side of the detector. The detectors are mounted such that c and d crystals are closest to  $\theta = 90^\circ$ . Each of the four crystals' midpoint angles subtend  $4.5^\circ$ .

Detector position	$\theta$ ( $^\circ$ )	$\phi$ ( $^\circ$ )
Q01	104.5	15
Q02	104.5	45
Q03	104.5	75
Q04	104.5	105
Q05	104.5	135
Q06	104.5	165
Q07	104.5	195
Q08	104.5	225
Q09	104.5	255
Q10	104.5	285
Q11	104.5	315
Q12	104.5	345
Q13	75.5	15
Q14	75.5	45
Q15	75.5	75
Q16	75.5	105
Q17	75.5	135
Q18	75.5	165
Q19	75.5	195
Q20	75.5	225
Q21	75.5	255
Q22	75.5	285
Q23	75.5	315
Q24	75.5	345

### 3.1.2 The SAGE electron transport system

The internal conversion electrons that are produced at the target area are transported away which facilitates suppression of the high background caused by the delta-electrons by using a high-voltage barrier (HV barrier) placed inside the main solenoid coil. A schematic representation of the SAGE detector setup is shown in Figure 3.2.

Three solenoid coils are placed in series around the target in such a way that the large electric current (700-1000 A) flowing in the coils produces a solenoidal magnetic field that can force the electrons to follow circular trajectories around the guiding centers that are moving along the magnetic field lines. The radius of the gyro-motion (or Larmor motion) depends on the kinetic energy of the electron due to the magnetic flux density in the beam direction. The resulting path of the gyro-motion and the uniform motion of the guiding center is called a helix. In this way the electrons are transported to the detector. A maximum magnetic flux density  $B_z$  of about 0.5 T is obtained in the middle of the coils.

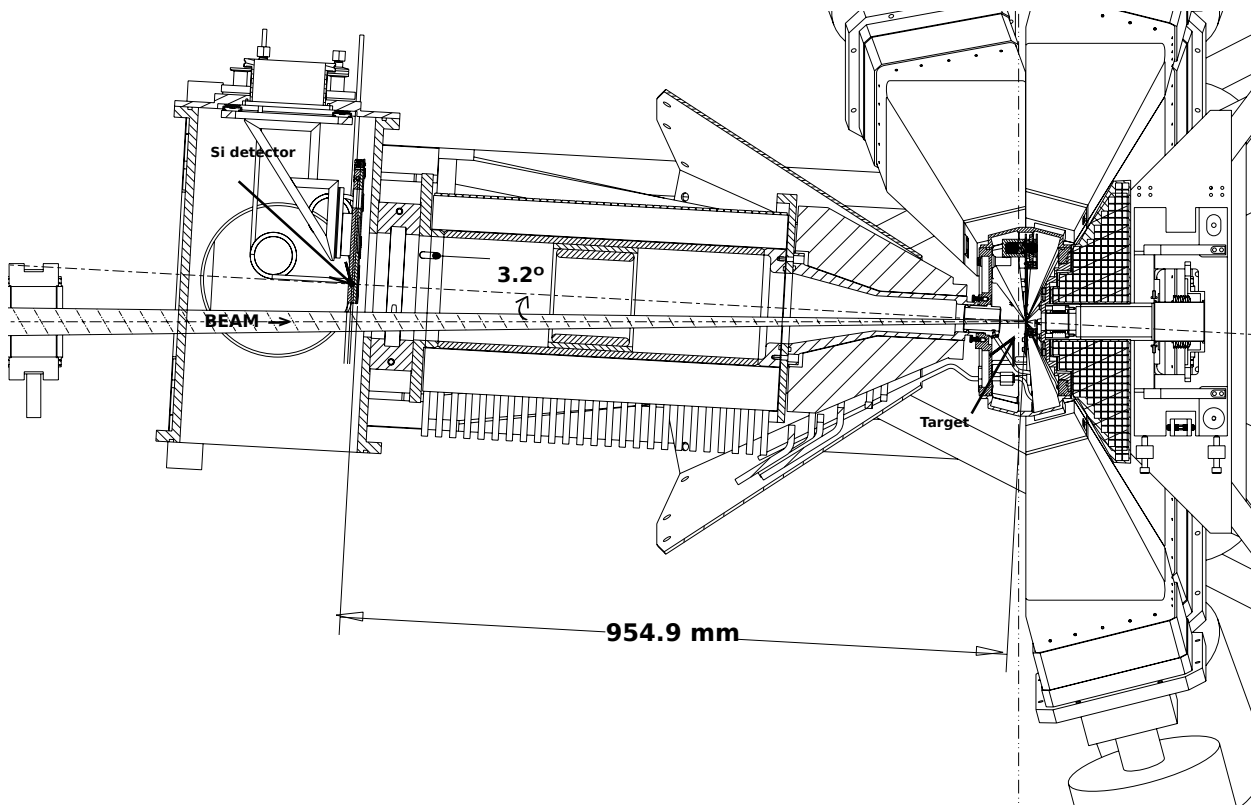


Figure 3.2: A schematic representation showing a cut of the SAGE detector setup as seen from the above. There is a  $3.2^\circ$  angle between the beam axis and the solenoid axis, and the two axes coincide at the target position. In this figure the HV barrier is visible inside the long main coil. RITU is to the right.

The HV barrier is designed to have a maximum potential difference of  $-50$  kV at its terminal. The voltage is applied to the cylindrical stainless steel electrode using a special horseshoe shaped connector. The edges of the electrode are rounded to prevent discharging. A cylindrical insulation sleeve made of Noryl surrounds the electrode and insulates it from the chamber. Due to the potential difference produced by the barrier, an electron with an energy of less than  $50$  keV will be slowed down and repelled, and electrons with higher energies will be slowed down and accelerated again on the other side of the barrier up to their original kinetic energy.

In addition to the coils, passive iron shielding had to be installed around the downstream and upstream coils to prevent the stray magnetic fields hindering the operation of the photomultiplier tubes (PMT) inside the Compton suppression shields of the JUROGAM II array. Because the large electric current heats the copper coils, water flowing inside the hollow coils is used for cooling purposes. The gas-filled separator volume is filled with helium at about  $1$  mbar, so two carbon foil windows of thickness around  $50 \mu\text{g}/\text{cm}^2$  at both ends of a cylinder with intermediate pumping in between have to be used to withstand the pressure difference and enable a high quality vacuum at the silicon detector chamber side. The mechanical and magnetic field designs, related simulations and the final chosen geometry of the SAGE setup are described in great detail in the PhD thesis of Dr. Philippos Papadakis [27].



### 3.1.3 The SAGE silicon detector

A segmented silicon detector is used in SAGE to detect and measure the energy of the conversion electrons that are emitted at the target position and transported by the magnetic field along the solenoid axis to the detector chamber. The thickness of the detector is 1 mm and the outer diameter of the active area is about 48 mm. The strip width is 1 mm for the pixels in the inner rings and 2 mm for the pixels in the 8 outer ring minus a  $70\ \mu\text{m}$  gap separating the pixels.

The detector is placed on a custom designed printed circuit board (PCB) that also accommodates 90 preamplifiers for the pixels. The preamplifiers are of type A1422 manufactured by Caen and they are placed equidistantly around the detector. A cooling plate is placed behind the PCB, which is refrigerated with circulating ethanol to keep the detector and preamplifiers cold.

The detector is segmented annularly and radially into 90 individual parts, as is shown in Figure 3.3, that also displays the numbering scheme of the detector pixels. This type of geometry is chosen in order to balance the count rate distribution more evenly to be able to cope with high count rates. The low-energy electrons that are produced abundantly mainly hit the centre of the detector, because of the energy dependence of the Larmor radius. The inner segments are smaller for this reason. Therefore, in this design it is crucial that the electron distribution is focused exactly at the centre of the detector.

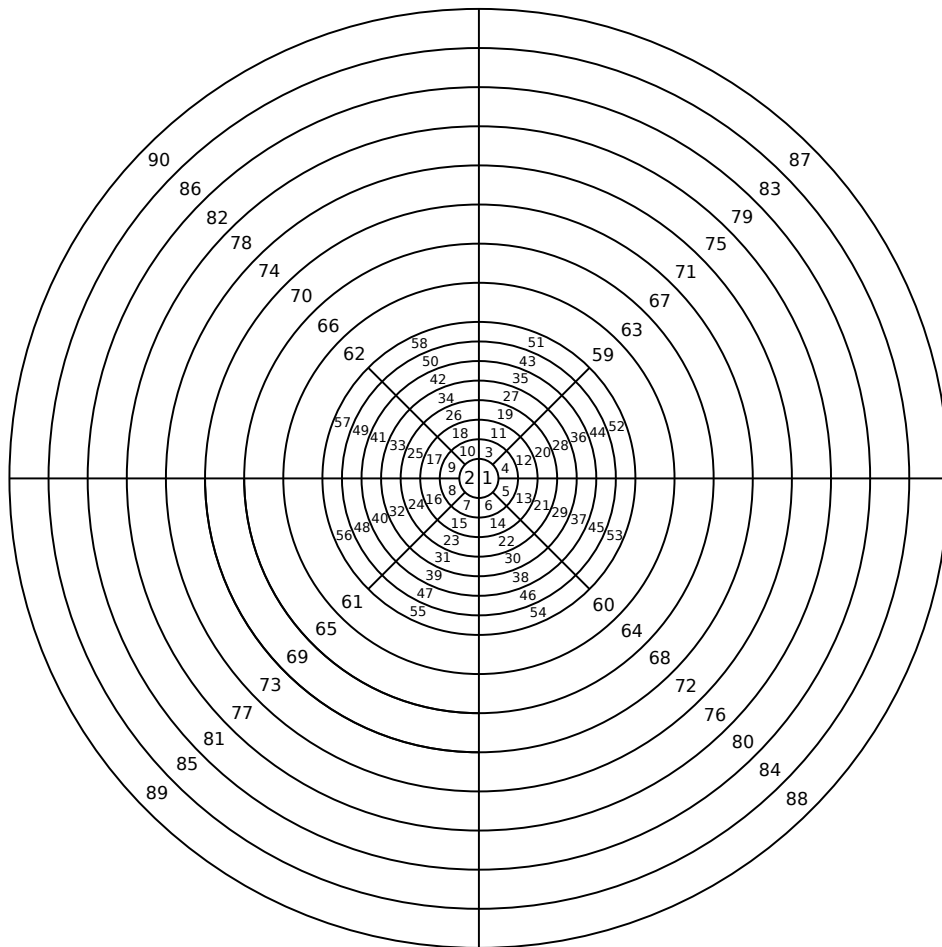


Figure 3.3: A schematic of the SAGE silicon detector geometry and the numbering scheme of the 90 individual pixels, as seen from the target position.

### 3.1.4 The RITU separator and the GREAT spectrometer

A gas-filled recoil-ion separator with a QDQQ magnet configuration called RITU [4, 28, 29] (Recoil Ion Transport Unit) is positioned downstream from the target along with the GREAT (Gamma Recoil Electron Alpha Tagging) focal plane spectrometer [5]. The separator is used to suppress the primary beam and separate the recoiling nuclei produced in fusion-evaporation reactions from scattered target nuclei and other contaminants. A schematic representation of the RITU separator with GREAT and the previously used JUROGAM array is presented in Figure 3.4. The support structure holding the two hemispheres of the JUROGAM array is also shown, which is still in use with the JUROGAM II array and enables the ball to be opened to allow access to the target chamber.

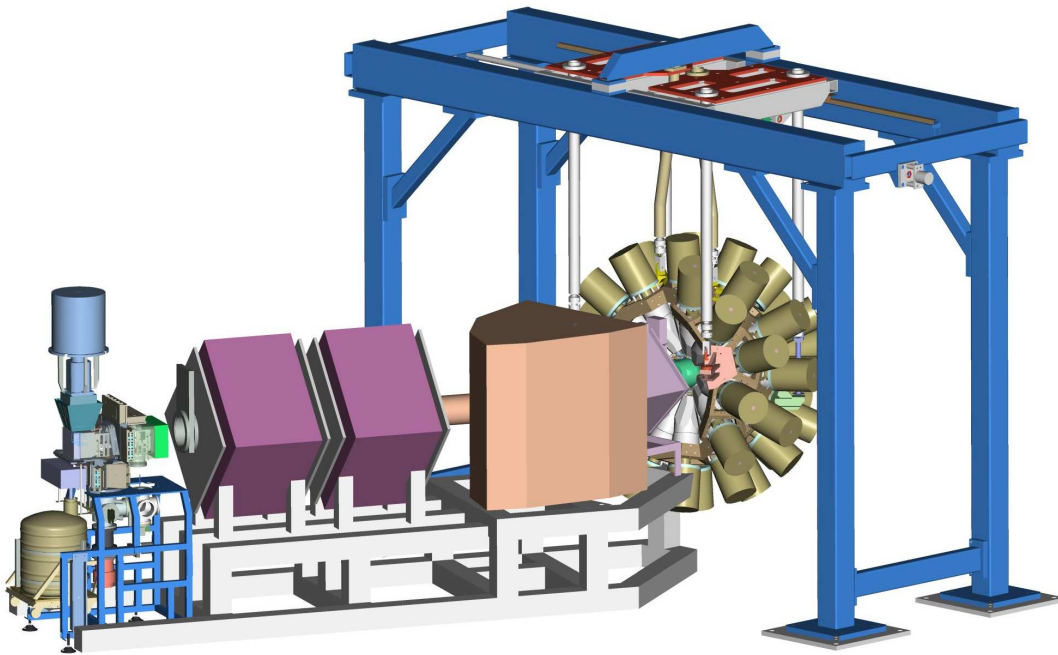


Figure 3.4: A schematic representation showing the RITU separator (middle) with the GREAT focal plane spectrometer setup (left) and the previously used JUROGAM array (right). The support structure holding the two hemispheres of the JUROGAM array is also shown.

The first quadrupole magnet Q1 is used as a vertical-focusing ion-optical element to improve the angular acceptance of the incoming fusion products before they get to the dipole magnet. In the dipole magnet, the primary beam is horizontally separated from the wanted fusion product using a strong vertical magnetic field. The two quadrupole magnets Q2 and Q3 behind the dipole magnet are used to adjust the vertical and horizontal focusing of the recoils at the focal plane. The maximum beam rigidity  $B\rho$  of RITU is 2.2 Tm and it is designed to have a good beam suppression in highly asymmetric reactions and high transmission of recoils with different charge states in the helium gas operation mode [11].

The focal plane spectrometer GREAT consists of two double-sided silicon strip detectors (DSSSD) placed side by side, a planar germanium detector, a large volume segmented Clover germanium detector, a gas filled multi-wire proportional counter (MWPC) and silicon pin-diodes. Usually, two more Clover type germanium detectors are operated on either side of the focal plane to provide more efficiency to detect gamma rays. The

GREAT spectrometer allows the use of the recoil-decay-tagging [30, 31, 32] (RDT) and similar methods for event selection, and measuring the energies of alpha decays, beta decays, gamma rays and X-rays that follow after the implantation of a fusion product in the DSSSD.

### 3.1.5 Electronics and data acquisition

The SAGE spectrometer is equipped with state-of-the-art digital front-end electronics made by Lyrtech for all the 90 silicon detector channels and the 106 germanium detector channels, making a total of 196 channels. A simplified schematic of a signal chain from the silicon detector and Caen preamplifier output to the Lyrtech VHS-ADC and finally to the tape server is shown in Figure 3.5. A similar signal chain is in use with the germanium detectors. The GO-boxes are simple gain and offset units to adjust the germanium and silicon signals to be able to use the full dynamic range of  $\pm 1.1$  V of the Lyrtech cards. The data acquisition system runs in a triggerless mode using the Total Data Readout (TDR) method [33], where every channel is read-out separately and timestamped using a 100 MHz synchronized clock signal (giving a time resolution of 10 ns at best) distributed from separate TDRi cards. This allows all the data to be collected from the detectors without losses caused by the dead-time or the read-out times, that are a problem when a conventional hardware trigger is used to force a read-out of the detectors and to create an event (common dead time mode). From the Lyrtech cards the data is either fed into the Event Builder, where the events are reconstructed and filtered using software triggers before saving them to disk or saved directly to the disk as raw data. The event data can be sorted online or offline using the Grain data analysis system [34].

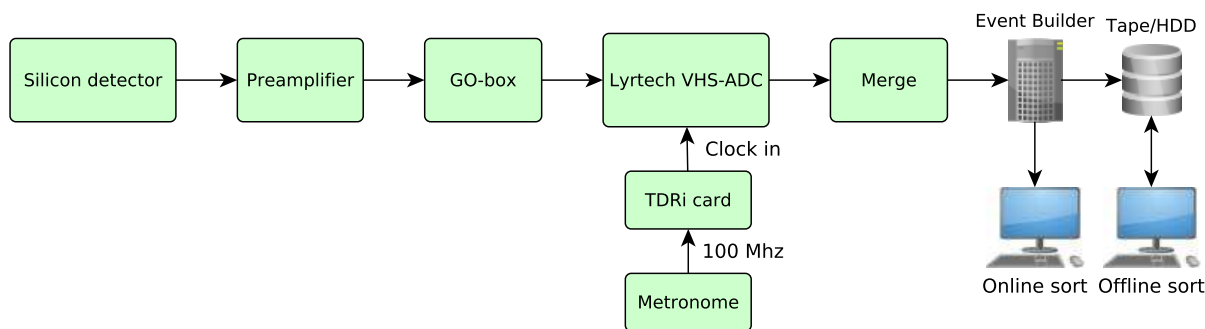


Figure 3.5: A simplified schematic of the signal chain from the silicon detector preamp output to the Lyrtech VHS-ADC card and tape server.

Pulse shape analysis is performed on the detector preamplifier output signals. An algorithm responsible for the AD conversion of the pulse heights (that are linearly proportional to the energy of the incoming radiation measured by the detector) is called the Moving Window Deconvolution [35, 36, 37] (MWD), which has been programmed as firmware in the Lyrtech cards. The MWD is a simple algorithm that was previously implemented in the electronics that are still in use with the EUROGAM PHASE III Cluster and the MINIBALL Cluster [38] detectors. The principle is that the original charge signal caused by the interaction of the gamma ray or electron with the detector is recovered from the typical exponentially decaying RC preamplifier signal by taking a moving average and performing a deconvolution operation. The moving average and decimation then averages out

the high frequency noise and generates a trapezoidal signal. The height of the trapezoidal signal is read-out from the flat top part of the pulse. After all of these operations, only the energy calibration is required to form a relationship between the channels (pulse heights) and the corresponding energies of the incoming radiation.

## 3.2 Radioactive source measurements

Details of the measurements that were performed in this work are presented briefly here. All the measurements were performed in the year 2011 at the Department of Physics Accelerator Laboratory (JYFL-ACCLAB) at the University of Jyväskylä, Finland. The source data for determining the electron detection efficiency was obtained during the re-commissioning runs of SAGE in October-November, 2011.

### 3.2.1 Measurements of sealed $^{60}\text{Co}$ sources with JUROGAM II

A calibrated  $^{60}\text{Co}$  point source of activity 401 kBq (1.4.2003) was placed at the target position and measured with the full JUROGAM II germanium array earlier this year (28.2.2011) in order to investigate the peak-to-total ratios of the detectors and the performance of the Compton suppression shields, as well as determine the absolute efficiency of the detectors and the array. The measurement time was 50 minutes (R25, during experiment J15). The relative uncertainty of the calibrated activity given by the manufacturer is 3%.

Another measurement of the gamma rays from a weaker 153 kBq (2.6.1986)  $^{60}\text{Co}$  source (JYFL-19) was made in June 2011, to investigate how the stray magnetic field affects the Compton suppression capability of the Phase 1 type germanium detectors located in the first ring in the JUROGAM II array, closest to the main coil. Different values of 0, 250, 500 and 750 amperes for the current in the coils were used, and the measurement time was 20 minutes 15 seconds in every measurement. The relative uncertainty of the calibrated activity given by the manufacturer is 3%.

### 3.2.2 Measurements of sealed $^{133}\text{Ba}$ and $^{152}\text{Eu}$ sources

Calibrated gamma-ray sources  $^{133}\text{Ba}$  (JYFL-82) and  $^{152}\text{Eu}$  (JYFL-81) placed at the target position were measured with JUROGAM II for energy and efficiency calibrations of the germanium array. The reported activities of the sources were 42.4 kBq (1.4.2003) for  $^{133}\text{Ba}$  and 40.1 kBq (1.4.2003) for  $^{152}\text{Eu}$ . Measurement R21 (1.11.2011) with a measurement time of 30 minutes, was used to determine the efficiency of JUROGAM II by measuring the gamma-ray yield from the source. Only the  $^{133}\text{Ba}$  source was present in the target chamber. In measurement R44\_0, both sources were inside the target chamber and the measurement time was 127 min. The relative uncertainties of the calibrated activities given by the manufacturer are 3%.

### 3.2.3 Measurements of an open $^{133}\text{Ba}$ electron source

The gamma rays emitted from an open  $^{133}\text{Ba}$  electron source (JYFL-90) placed at the target position were measured with the JUROGAM II array and the electrons with the silicon detector (1.11.2011, R20). In this way, the exact activity of the open  $^{133}\text{Ba}$  electron source could be determined from the gamma-ray yield. It was known that the reported activity of the source (375.9 kBq @ 15.12.2008) was no longer valid. The diameter of the active area of the source is 5 mm, and the half-life is  $t_{1/2} = 10.57 \text{ a} = 3858 \text{ d}$ .

Furthermore, various settings for the coil currents and the HV barrier voltage were used in the measurements that followed. A current of 800 A in the coils with 0 and  $-25 \text{ kV}$  at the HV barrier were chosen for this work (R50 84 min 5 s, R51 60 min, 9.11.2011) to determine the electron detection efficiency. In these measurements, the carbon foil unit and helium gas were not present in the target chamber. The pressure in the detector chamber was about  $10^{-6} \text{ mbar}$ , the silicon detector's ethanol cooling unit (Julabo) was set to  $-30^\circ\text{C}$  and the detector bias voltage was 80 V. All of the detector pixels were working, but not all of them were able to collect enough statistics to be able to perform a proper calibration, because the electron distribution was simply not hitting some pixels situated at the edges of the detector. In two runs (R50, R51, with and without  $-25 \text{ kV}$  HV barrier voltage applied, respectively) the target position was adjusted to +500 steps upward (about 4 mm) using the target wheel to get the distribution centred on the detector without making physical modifications to the detector holder mechanism. This alignment problem has since been resolved with a modification of the detector support structure.



# 4

## Simulations

Producing a realistic simulation of the trajectory of a charged particle passing through different types of matter and evaluating its energy loss along the path while it is moving in a spatially varying and complex electromagnetic field and physical geometry is not an easy task. Currently, it is only possible with very few computer programs that are readily available. The Monte Carlo method has become widely used for simulating interaction cross-sections (probabilities) of the passage of electromagnetic and particle radiation in matter, and is used, for example, in the well-known program SRIM [39] for calculating the stopping force (i.e. power) and range of charged ions in matter. One of the most widely used tools for simulating particle radiation is the Geant4 simulation toolkit [6]. Geant4 is an enormous collection of programming libraries, which provide a way to simulate a complete reproduction of an experimental situation and a measurement that involve radiation. The physics libraries in the toolkit that are used to determine energy losses are constantly being developed and evaluated with measured data to ensure good agreement with experimental results.

### 4.1 Geant4 – the simulations toolkit

Geant4 is a free<sup>1</sup> software toolkit to simulate the passage of different particles and electromagnetic radiation through matter using Monte Carlo methods. The toolkit makes it possible to track particles, visualise particle tracks, introduce and design complex geometries for detectors and environments, try out and develop physics models for different processes and interactions in a vast energy scale ranging from eV up to TeV energies. It has been developed by a large world-wide collaboration of research laboratories, national institutes and high-energy physics experiments including, for example, The European Organization for Nuclear Research (CERN). In recent years, the Geant4 toolkit has been widely used in applications [40] such as high-energy particle physics experiments (LHC - The Large Hadron Collider and the detector systems at ALICE, ATLAS, and CMS experiments, Tevatron and future particle accelerators and detectors), nuclear physics (germanium and silicon detector responses to radiation), space science (background radiation dose calculation, single-event upsets in electronics), medical physics [41] and radiation protection (radiation treatments using hadrons, PET imaging, radiation shielding and simulations of radiation effects in living tissues).

---

<sup>1</sup>The complete source code and binaries of the simulations toolkit is available at the Geant4 collaboration website: <http://geant4.cern.ch>

The new simulation toolkit was named Geant4 in order to distinguish it from its predecessor, the old Geant3 FORTRAN code developed originally at CERN. It has been completely rewritten using the modern object-oriented approach in the C++ programming language. Another improvement to the old version is the possibility to simulate low-energy electromagnetic processes and particles with energies less than 10 keV and down to about 250 eV. The power of the library is in its ability to handle complex geometries, particles moving in electromagnetic fields, simulation of detector response to enable more realistic simulations and prediction of experimental results. Although it was originally developed with high-energy physics experiments in mind, the models of the low-energy interactions and processes are constantly being developed [42] and evaluated with experimental results [43, 44].

## 4.2 Geant4 simulation package of SAGE

In the early design stage of SAGE, a Monte Carlo simulation code known as SOLENOID [2] was used to simulate the performance of the spectrometer [1, 27] using various configurations of the coils and the HV barrier. This code had been originally developed to simulate the superconducting conversion electron spectrometer SACRED [2]. However, with this simulation code it was only possible to simulate the electron transport and detection parts and was limited to two-dimensional cylindrical geometries for the detector system. In the final design of SAGE, a part of the setup lies on a different axis than the solenoid axis (the downstream coil is aligned with the beam axis), which cannot be represented perfectly in cylindrical geometry. Furthermore, there is a noticeable discrepancy in the measured electron detection efficiency for high energies ( $\geq 400\text{keV}$ ) compared to the simulated efficiency already in the case of SACRED, as can be seen in Fig. 5 in [3].

A more realistic reproduction of the detector setup is possible in Geant4, because it fully supports three-dimensional geometries and models, and also makes it possible to reproduce any non-symmetric parts of the geometry. In order to fully understand and fine-tune the electron spectrometer part of the detector system, a Geant4 simulation package of SAGE was developed [8].

Another advantage of using Geant4 is the possibility to combine the JUROGAM II array of germanium detectors in the same simulation with the electron transport and detection part for the first time. This was not possible in the SOLENOID code, which does not have germanium detectors. This makes it possible to try-out and introduce more complex events in the simulation as in a real recoil-decay tagging (RDT) experiment with simultaneous detection and emission of gamma rays, X-rays, internal conversion electrons, fusion-evaporation residues and the production of delta-electrons and secondary electrons from the interactions of the beam particles with the target.

In future, the simulation package can be improved further and used to predict the Doppler shift in the measured energies, compare experimentally measured fractions of detected electrons from different shells and to produce de-excitations of nuclei from user created level schemes to aid in the analysis of experimental data. A possibility to include the RITU separator and the focal plane detector setup of GREAT in the simulation package has also been discussed. Including the magnetic fields produced by the QDQQ magnets would enable combined RDT-like simulations, where the fusion recoils are detected in the silicon strip detectors at the focal plane and the prompt gamma rays and internal conversion electrons at the target position.



A typical view of the Geant4 Graphical User Interface (GUI) from the simulation is shown in Figure 4.1. Commands to simulate events and alter settings in the simulation can be given directly in the GUI window. The events from a “run” are visualised using OpenGL on the right on top of the three-dimensional geometry that can be freely rotated and zoomed around using the mouse. In more time consuming simulations, a batch mode of operation can be used from the command line, which runs faster and quietly without the visualisation.

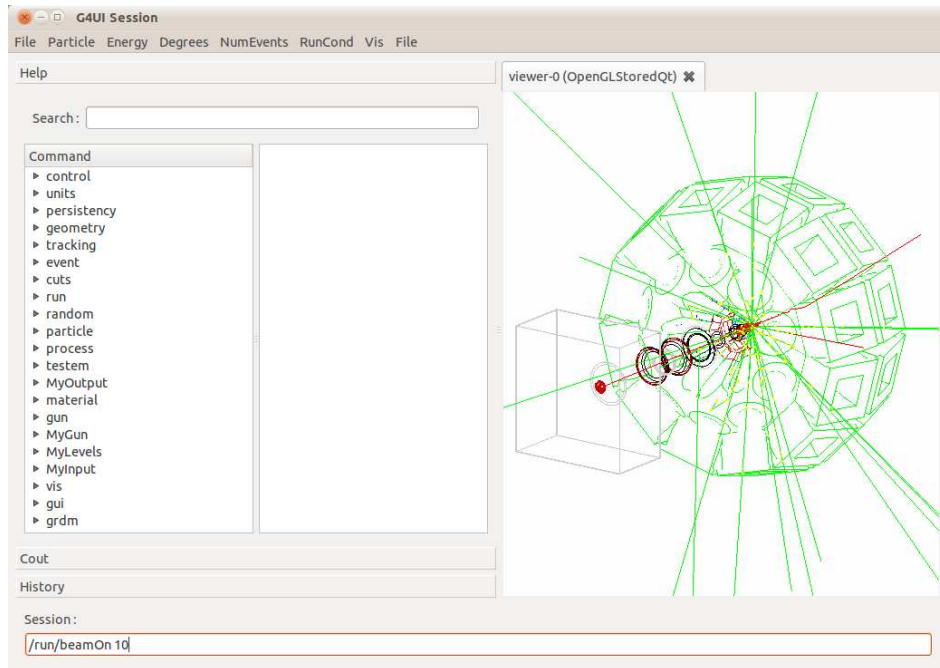


Figure 4.1: A typical view of the Geant4 GUI using Qt 4.0 and OpenGL to visualise detector geometry and particle tracks from events.

## 4.2.1 Simulation geometry of SAGE

The essential parts where electrons and gamma rays can interact have been modelled in the simulation package by coding them directly in pure C++ language using the primitive CSG solids, specific CSG solids and boolean solids in the geometry module [45] of Geant4. This is due to the unfortunate fact that there are no proper (or free) CAD import/export utilities available to enable a convenient method of designing models in a 3D CAD software and importing them to Geant4 afterwards. Using the still young Geometry Description Markup Language (GDML) based on XML with free CAD software (e.g. FreeCAD) was not investigated, but could be helpful in the future when more complex geometry is added to the simulation.

The complete simulation geometry of SAGE as it is modelled in Geant4 is presented in Figure 4.2. Only one half of the JUROGAM II array of germanium detectors and their BGO shields are shown and the electron spectrometer is drawn mostly in wireframe for illustration purposes. Included in the figure are the detector chamber, the silicon detector with 90 pixels corresponding to the same layout as in Figure 3.3, the beam line up to the target chamber, the complete HV barrier visible through the beam line with the “horse shoe” shaped connector, carbon foil (CF) unit at the entrance to the target chamber, the

target chamber with the complicated backplate face (towards RITU) and the target wheel. A separate volume with helium is placed inside the target chamber (not shown). Around the target chamber are the germanium detectors inside their BGO shield housings (green) and Hevimet<sup>2</sup> collimators (red). The Phase 1 detectors are on the left (1 ring, upstream side) with their aluminium end-caps shown in white and the Clover detectors on the right at a nearly 90° angle with respect to the beam axis (2 rings, crystals and the end-caps are not visible through the BGO shields).

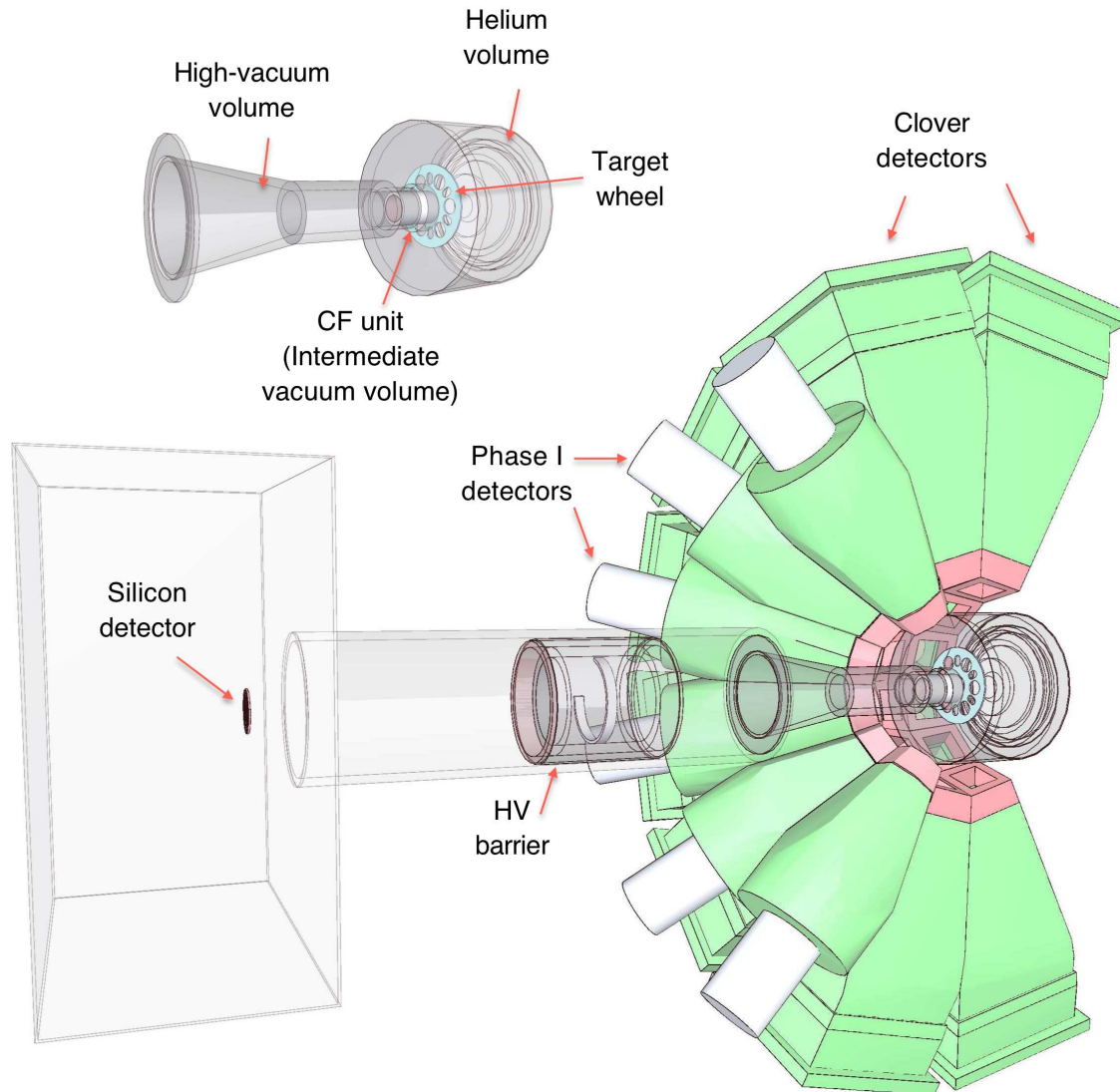


Figure 4.2: A schematic representation of the modelled simulation geometry. Only one half of JUROGAM II is shown for illustrative purposes. The main parts of the device are indicated in the figure.

Many simplifications have been made to the simulation geometry and not everything has been included as can be seen from Figure 4.2. For example, the physical copper coils producing the magnetic field, iron and lead shielding around the coils and the honeycomb-like spherical support structure of JUROGAM II are still missing. These objects do not affect the electron transport or detection in the simulation, but can scatter gamma rays into the germanium detectors and their Compton suppression shields making the peak-to-total ratios worse and cause false vetoes also in the simulation.

<sup>2</sup>Hevimet is a metallic alloy of 95% W (tungsten), 3.5% Ni (nickel), 1.5% Fe (iron), density 17.0 g/cm<sup>3</sup>.

The simulation models of the Compton suppression shields and the heavy-metal collimators for both types of germanium detectors are presented in Figures 4.3(a) and 4.3(b). Close-ups of the modelled BGO crystals inside the housings are shown in Figure 4.4, where also the germanium crystals and the passivated volumes (bore hole and lithium contact) inside the germanium crystals are visible. The BGO shields and crystals are modelled to match the design drawings very closely, but they are not perfect due to the difficult geometry involved and challenges imposed by the modelling done by hand-coding them in C++ using the primitive shapes available in the Geant4 geometry package. In reality, the crystals are composed of about 10 smaller pieces, but are modelled as a solid block in the simulation.

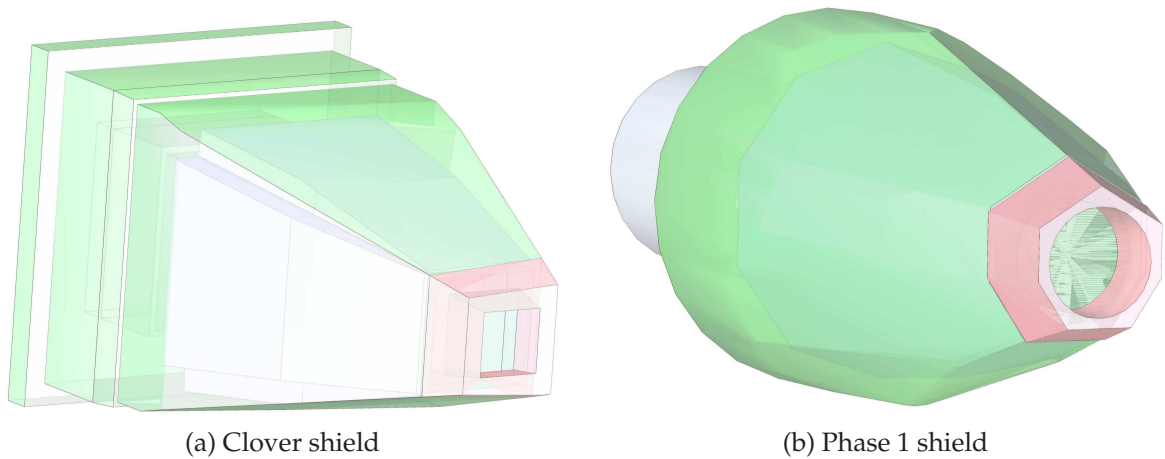


Figure 4.3: A schematic representation of the BGO Compton suppression shield housings (green) for (a) the Clover and (b) the Phase 1 detectors in the Geant4 simulation. Hevimet collimators are shown (red) and the BGO crystals inside as they are modelled in the simulation.

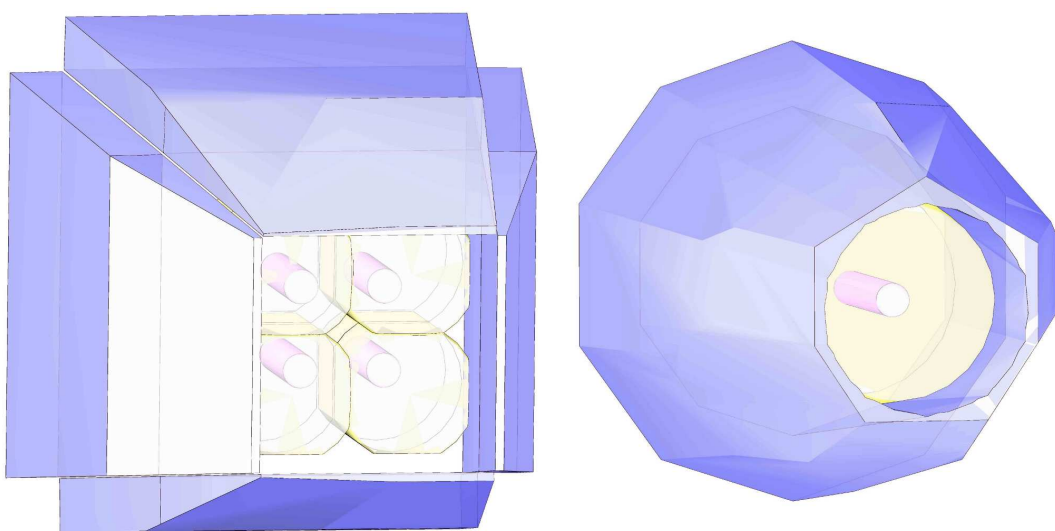


Figure 4.4: A schematic representation of the Clover (left) and the Phase 1 (right) BGO crystals and the germanium crystals as they are modelled in the simulation. The passivated volumes from the bore hole and lithium contact are visible.

## 4.2.2 Simulating events and a $^{133}\text{Ba}$ source in Geant4

Various types of events can be constructed by the user in a simulation run by using the `G4ParticleGun` class, that can produce any kind of particle defined in the Geant4 physics lists and “shoot” it in any direction. A simple event created using this method is shown in Figure 4.5, where electrons and gamma rays with energies of 100 keV are emitted in random directions from the target position. By using suitable random number generators, routines to read in level schemes from files and shooting the gamma rays, electrons and other particles with the `G4ParticleGun`, it is possible to produce simulations of a decaying nucleus with chosen relative intensities of the transitions. However, this is not an easy task and requires a lot of effort, especially if angular distributions are to be properly taken into account. Another promising possibility is a module called General Particle Source [46] (GPS), which unfortunately has not been developed for a while. Recently, a new class called `G4RadioactiveDecay` has been included in Geant4 to create simulations of the radioactive decay of known nuclei using the level and decay scheme data from the Evaluated Nuclear Structure Data File (ENSDF) [47] maintained by the National Nuclear Data Center, Brookhaven National Laboratory.

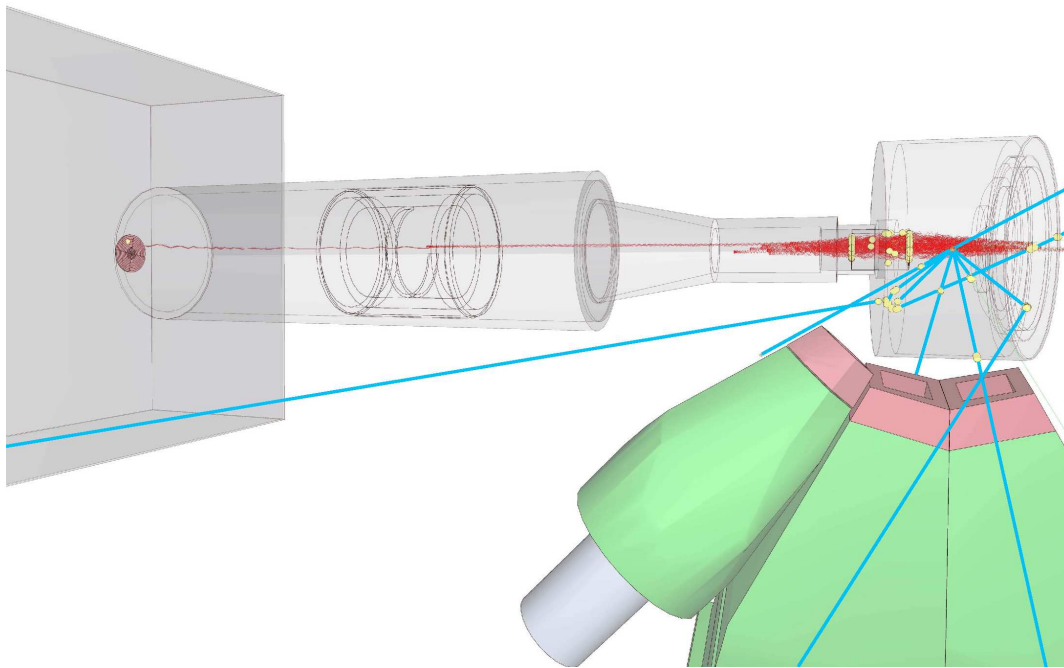


Figure 4.5: An example drawing of simulated events visualised in Geant4. Electrons are presented with red lines and gamma rays with blue. Only some of the electrons reach the detector while the others either interact with the surrounding materials (open circles) or are reflected back by the HV barrier. Note also the magnetic bottle effect of electrons being trapped in the magnetic field.

To use `G4RadioactiveDecay` in a simulation, the user only needs to enable the process in the physics list and use the `G4ParticleGun` to shoot out a nucleus with given  $A$ ,  $Z$  and excitation energy in an event. In these simulations, the `G4RadioactiveDecay` class was used to create the  $^{133}\text{Ba}$  source in the events. Major slow-downs in the simulation runs were observed whenever the decay happened in vacuum, because Geant4 also tracks the

daughter nucleus of the decay ( $^{133}\text{Cs}$ ) and does not allow it to de-excite until it interacts with something in the surroundings and is stopped completely. To speed up the simulation, the physical geometry of the source was also modelled in the simulation. The open  $^{133}\text{Ba}$  electron source consists of a circular, thin aluminised mylar foil as a backing and a very thin acrylic foil as a cover according to the manufacturer. The small aluminium support ring around the foils was not included. The source backing and cover solves the issue of slow simulation speeds, but also overestimates the effect on the detection efficiency of the electrons. Either the model or the material definitions need adjustments, and for this reason the source material was not included in the efficiency simulations.

The possibility to read-in user created level schemes for decays and de-excitations will be developed for the simulation package in the near future for increased reliability, accuracy of the results and the ability to investigate new physics cases in experiments, where the decay and level schemes are not always known beforehand.

Currently, it is not possible to keep track of time in the simulation, properly detect coincidences from multiple decays inside one event or timestamp the events that are saved. This will be required to be able to estimate the delta-electron background, create coincident de-excitations including possible isomeric states with longer life-times and include the RITU separator and the GREAT focal plane spectrometer in the same Geant4 simulation.

### 4.2.3 Materials, physics lists and Geant4 library versions

In Geant4 all the geometric shapes that are placed in the simulation's world (mother) volume have to have a material definition. Even the world volume has a material, usually defined as a very good vacuum (a very low-density gas, the Geant4 Galactic vacuum pressure is  $3 \cdot 10^{-18}$  Pa, temperature 2.73 K and the density is defined as the mean density of the universe  $1 \cdot 10^{-25}$  g/cm<sup>3</sup>). In this work, a more realistic vacuum of ambient air at  $1 \cdot 10^{-6}$  mbar pressure was used, which is the usual pressure present in the silicon detector chamber during the measurements. Other important material compositions used in the simulation are given in Tables 4.1 and 4.2.

Table 4.1: Compositions of the most relevant materials used in the simulations, part 1/2. An integer value denotes the number of atoms in the composition, otherwise elemental mass fraction. Densities and pressures are given for gases.

Element	Vacuum (Air)	He (gas)	C (foils)	Ge	BGO	Mylar	Acrylic
H						8	8
He		1					
C			1			10	5
N	0.7557						
O	0.2315				12	4	2
Ar	0.0128						
Ge				1	3		
Bi					4		
Density (g/cm <sup>3</sup> )	$1.28 \cdot 10^{-12}$	$0.1615 \cdot 10^{-6}$	2.3	5.32	7.13	1.397	1.18
Pressure (mbar)	$1.0 \cdot 10^{-6}$	1.0					



Table 4.2: Compositions of the most relevant materials used in the simulations, part 2/2. An integer value denotes the number of atoms in the composition, otherwise elemental mass fraction. Densities are also given.

Element	Silicon	Aluminium	Steel (stainless, 18-8)	Hevimet
Si	1			
Cr			8	
Ni			18	
Cu		0.035		0.035
Mg		0.005		
Mn		0.006		
Fe			74	0.015
Al		0.954		
W				0.95
Density (g/cm <sup>3</sup> )	2.33	2.8	8.0	17.0

Defining materials in a gas state is not that straightforward in Geant4, and can easily lead to mistakes in density and in the end cause large errors in the energy loss of particles travelling through the gas. The density of a gas at pressure  $p$  (Pa), with a molar mass  $M$  at temperature  $T$  (K) can be solved from the well-known ideal gas law

$$pV = nRT = mRT/M \Rightarrow \rho = m/V = pM/RT, \quad (4.1)$$

where  $R$  is the universal gas constant  $8.3144621(75) \frac{\text{J}}{\text{mol}\cdot\text{K}}$  [48]. Usually the densities for gases are given at STP conditions (293.15 K, 101.325 kPa), from which they are easy to scale to lower pressures.

The most recent Geant4 simulation toolkit and data file versions that were available were used in this work. The version numbers are: Geant4 4.9.4.p02, G4EMLOW 6.19 (low-energy EM physics processes [49]), PhotonEvaporation2.1 (photons that are emitted from de-exciting nuclei) and G4RadioactiveDecay 3.3 (responsible for producing the decaying nuclei and their decay schemes). A new version of Geant4 (4.9.5.b01, released June 30<sup>th</sup>, 2011) was available, but was not used because of the beta status. Many improvements have been introduced in the new version, maybe one of the most useful being the properly working trapezoidal shapes that can be used to create boolean solids to make designing more complex geometric shapes easier.

It should be noted that even though the decay schemes and intensities used in the PhotonEvaporation and G4RadioactiveDecay data libraries are from ENSDF, they are not in human readable form in the data files of Geant4, so they should be used with caution. There have been reports of the decay schemes being completely wrong for certain nuclei, such as <sup>133</sup>Ba and other decay schemes as was noted by Golovko et al. [50] in 2008. For some nuclei, the decay schemes have been verified successfully by comparing the results to previous Geant versions [51].

The standard physics list package usually provides good results for energies above 1 keV, and includes modelling and cross-sections of the physics processes [19] such as multiple scattering, ionisation, bremsstrahlung, Compton scattering, pair production, photo-electric effect, annihilation, synchrotron radiation, Cerenkov radiation, transition radiation and high-energy muon processes. In the case of electrons with energies above 1 keV, the

results obtained with both the standard physics models and the low-energy models are in good agreement with experimental data [43, 44]. The low-energy EM physics lists were tested with the SAGE simulation package by simulating a  $^{133}\text{Ba}$  source and comparing the obtained spectrum to one produced using the standard physics list, but the spectra were almost identical. Only slight differences could be seen as a bit more tailing at the low energy side of the peaks (at energies  $\leq 50$  keV). For this reason, the faster standard physics lists were used in the efficiency simulations. If the simulation package is used to simulate delta-electron production or other types of events, the effect of the low-energy physics lists should be checked again.

#### 4.2.4 Simulated electromagnetic fields

The electric and magnetic fields are an essential part of the SAGE spectrometer system. Therefore, a realistic model of the fields had to be included in the simulation to properly simulate the transportation of the electrons from the target area to the silicon detector. The field profiles created by the high electric potential at the HV barrier and the large electric current in the solenoid coils were simulated using the *Vector Fields OPERA 3D* simulation software [7]. In those simulations some of the surrounding materials like the passive shields around the coils have also been included, because they affect the field profile. Once the three-dimensional field profile has been simulated in *OPERA 3D*, it is output to a field data file that has the electric and magnetic field vector components corresponding to the spatial coordinates of the chosen grid points.

The field file can then be used as an input file for a user created field class in the Geant4 simulation, that creates a matrix from the tabulated values and returns the vector components of the fields at any given spatial coordinates in the simulation geometry by using quadratic or cubic interpolation of the three-dimensional grid. The accuracy of the interpolation is restricted mainly by the grid size defined in *OPERA 3D* for the output file. Higher accuracy is obtained with cubic interpolation, but the algorithm slows down the tracking of particles considerably. For this reason, the faster quadratic interpolation is used, still providing a very reasonable accuracy if the step and chord lengths are not chosen “too small”.

A three-dimensional plot of the interpolated magnetic field component  $B_z(x, y = 0, z)$  in the  $xz$ -plane (for the  $y = 0$  coordinates) is presented in Figure 4.6. The current in the solenoid coils was 1000 A. Similarly, an interpolated plot of the electric field component  $E_z(x, y = 0, z)$  produced by a  $-50$  kV voltage at the HV barrier is shown in Figure 4.7. The interpolation of the intermediate points between the grid points of the field file are done using the same class that is used in the Geant4 simulation. A quadratic interpolation was used to calculate the intermediate values of the magnetic field component  $B_z$  and the electric field component  $E_z$ .

In Geant4 it is possible to track particles that are moving in spatially varying and “smooth” electric and magnetic fields, but the fields have to be implemented in a user defined class providing the vector components of the fields at every spatial location in the simulation geometry. A differential equation solver is used in small steps to solve the equation of motion of the particle in a varying electromagnetic field as in Equation (2.8). The step length, chord length, intersection distances and other variables used by the chosen stepper (algorithm) can be defined by the user.

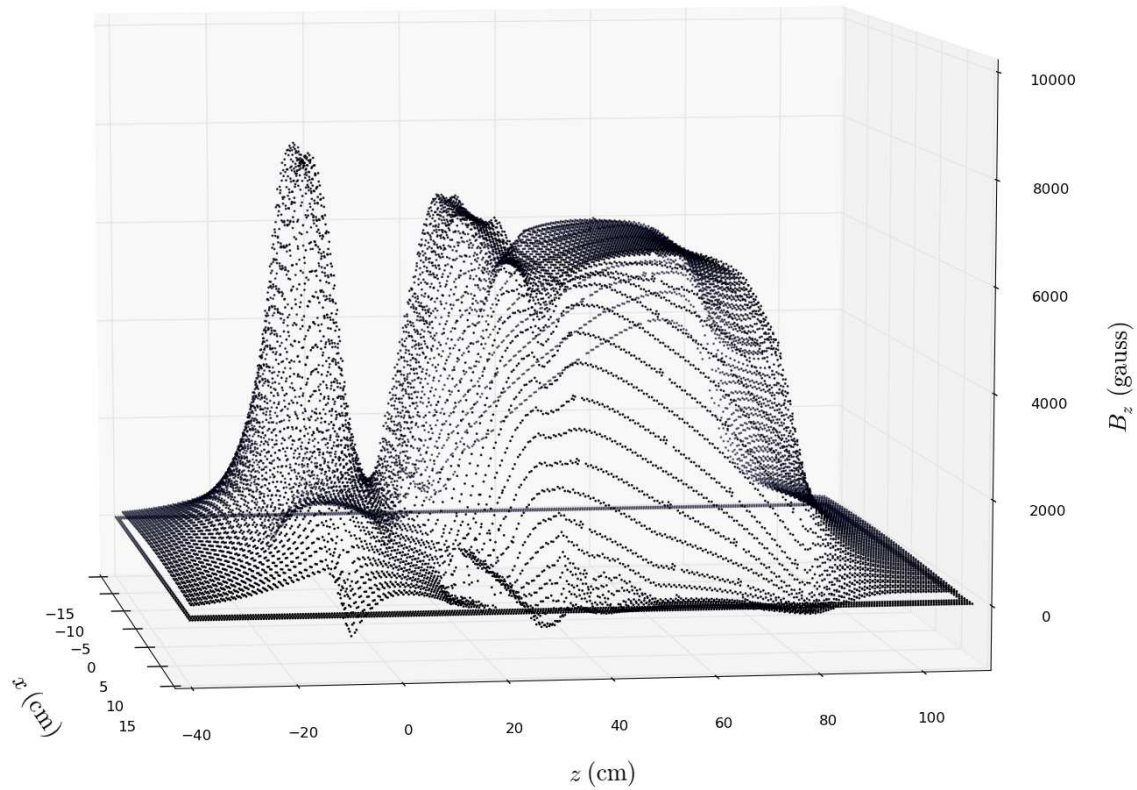


Figure 4.6: The interpolated magnetic field profile of the  $B_z$  component in the  $xz$ -plane at  $y = 0$ . The target is at the origin and the detector at around  $z = 95$  cm at an angle of  $3.2^\circ$  to the  $z$ -axis.

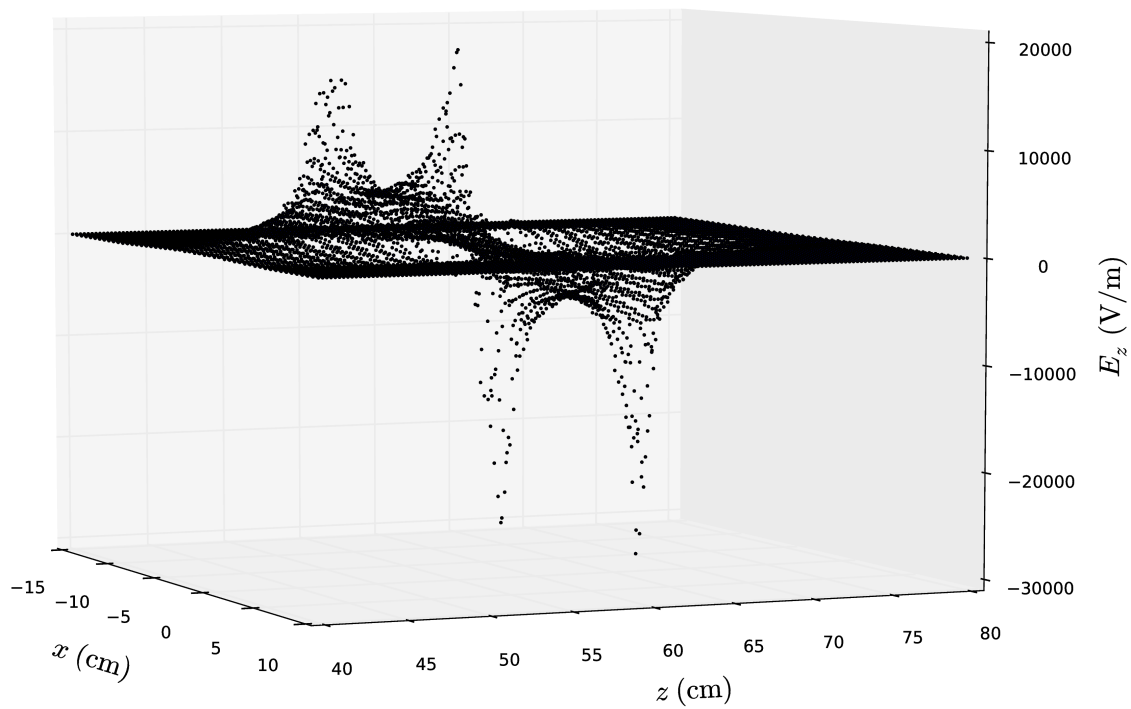


Figure 4.7: The interpolated electric field profile of the  $E_z$  component produced by a potential of  $-50$  kV at the HV barrier in the  $xz$ -plane. The interpolation is performed at the  $y = 0$  coordinates. The target is at the origin and the detector at around  $z = 95$  cm at an angle of  $3.2^\circ$  to the  $z$ -axis.



In the simulation package of SAGE, a stepper employing a 4<sup>th</sup> order (giving 5<sup>th</sup> order accuracy) Cash-Karp Runge-Kutta-Fehlberg 4/5 algorithm [52] was used for enhanced accuracy (G4CashKarpRKF45). This stepper was chosen because the simulation times did not seem to benefit from using a lower order Runge-Kutta stepper (G4SimpleRunge or G4ClassicalRK4).

The values that are used for the relevant stepper variables are displayed in Table 4.3. The chosen step length and other values may seem large at first sight (0.01-0.1 mm). Using smaller values does not increase the accuracy and only acts to slow down the tracking and create errors in the calculation, because the field matrix used in the interpolation has a grid size of 1 cm x 1 cm x 1 cm. The values are chosen as an optimal balance of speed and reasonable accuracy. The step length is chosen to be long enough to provide fast calculation without compromising the accuracy of the results. Examples of the electron tracks in the simulated field can be seen in Figure 4.5. The magnetic bottle effect can be seen with electrons being trapped in the target chamber area, and the radius of the helix track changes depending on the local magnetic field strength  $B_z$ .

Table 4.3: Values used for the variables of the stepper and the chord finder.

Variable:	Value
Variables	8
Minimum Step	0.01 mm
Delta Chord	1 mm
Delta Intersection	0.1 mm
Delta OneStep	1 mm
Min Epsilon Step	$1 \cdot 10^{-6}$
Max Epsilon Step	$1 \cdot 10^{-3}$

## 4.2.5 Simulation event data analysis tools

The output of the Geant4 simulation package of SAGE is a human-readable data file, that contains only those events, in which something was detected in any of the modelled detectors. To produce a spectrum of any kind, the event data has to be read through (i.e. “sorted”) by a separate analysis program. Analysis programs were created in the C++ programming language by the author and used in this work to analyse the Geant4 output. The programs use the AIDAJNI 3.2.6 adapter package [53] (a wrapper) to link together with JAIDA 3.2.1 [54], the Java implementation of the Abstract Interfaces for Data Analysis (AIDA). This process is schematically presented in Figure 4.8.

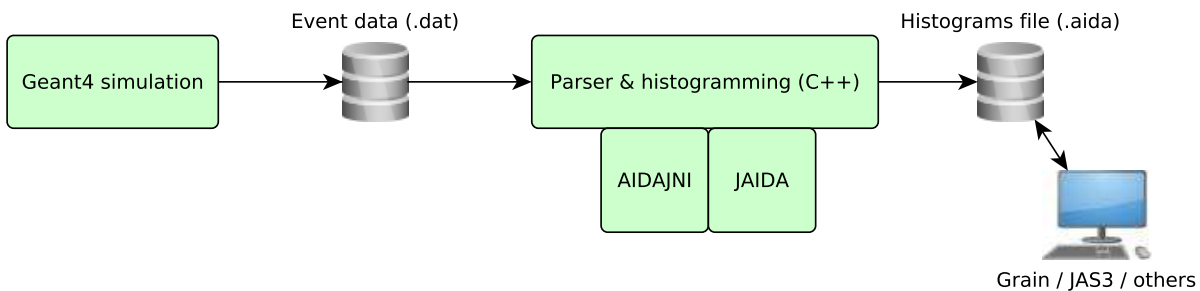


Figure 4.8: A simplified schematic of how the information obtained from the simulation is saved to event data on the hard-drive and later analysed by the sort program to create the histograms file, that finally can be viewed and analysed by the user.

The output of the analysis programs is an .aida file that is fully compatible with the current Grain data analysis system [34]. This makes it possible to use the same data analysis software to analyse and visualise the spectra that is used for real measurement data. Additionally, it is easy to output spectra from Grain in e.g. ASCII, GLE graphics and RadWare [55, 56] compatible formats.

Currently, the analysis tools are able to produce the spectra for individual detectors and sums of all detectors. The available spectra include gamma-ray singles, electron singles, gamma-gamma coincidences, electron-gamma coincidences and electron-electron coincidences including addback and Compton suppression with the BGO shields, if needed. The coincidences are determined in a simplified way by using only event numbering. It is also possible to create histograms and matrices of the initial angles and energies of the emitted particles. Many types of hitmaps for the silicon detector are available: a simple pixel map that displays the number of counts in each pixel as a 1D histogram, a polar map with a graphical display of the pixels as a 2D histogram and a more accurate 2D histogram of the  $x$ - and  $y$ -coordinates of the hitpoint from Geant4. The 2D polar map is made with the same algorithm as in the usual sort codes used to read through the real SAGE data in Grain. Examples of the 2D polar map and 2D hitmap can be seen in Figures 5.13(a) and 5.13(b). The accuracy given by the latter figure is not actually possible in a real experiment, but it is still included, because in a simulation it is readily available, and can give the location of the centroid of the distribution more precisely when simulating different field configurations.

## Data analysis and results

The methods used in the calculations and the final results that were obtained from the simulations and the measurements are presented in the following sections. The peak fitting and determination of the peak areas from the measured spectra were made using the RadWare software [56] (gf3), unless otherwise noted. In most cases, the data from the simulations was less complex and allowed the use of simpler integration routines incorporated in Grain [34] for data analysis.

### 5.1 The gamma-ray detection efficiency of JUROGAM II

In a simulation you are not limited to using calibrated radioactive sources that cover only part of the energy spectrum. It is possible to simulate the efficiency at any given energy. However, false vetoes, random pile-up and such effects are not present in these simple simulations, which can be a problem when using real sources emitting gamma rays of many different energies such as a combination of  $^{133}\text{Ba}$  and  $^{152}\text{Eu}$ .

To simulate the gamma-ray detection efficiency of SAGE and the JUROGAM II array consisting of 24 Clover detectors and 10 Phase 1 type detectors, 100 000 monoenergetic gamma rays for each energy in 25 keV steps in the energy range 25-2000 keV were emitted at the target position in random directions. The efficiency to detect a gamma ray of a given energy is then given by the number of the detected gamma rays in the full energy peak divided by the total number of emitted gamma rays, as given by Equation (2.15). The simulated gamma-ray detection efficiency curves of JUROGAM II are presented in Figure 5.1, with and without using the add-back method. The simulation gives an efficiency of about 4.9% at 1.3 MeV.

The measured gamma-ray detection efficiencies (using add-back) from calibrated  $^{133}\text{Ba}$  and  $^{60}\text{Co}$  sources are presented in Figure 5.1. The efficiencies from the  $^{60}\text{Co}$  source were determined using the activity method i.e. from the area of the peaks in the singles spectra of individual detectors and known activities of the calibrated sources. For example, the efficiency at 1.3 MeV is  $(4.4 \pm 0.1)\%$ . The measured values are lower than that given by the ideal simulation for various reasons described below.

One of the major causes for the discrepancy in the results are the dead-time, false vetoes and pile-up issues that are present in real measurements. These effects are not accounted for in the current simulation. Another important thing is that in reality all the germanium detectors are not perfect as in the simulations. Some of the detectors suffer from a very bad energy resolution due to neutron damage and some channels are not functioning at all. The germanium crystals can have slightly different sizes and can be located

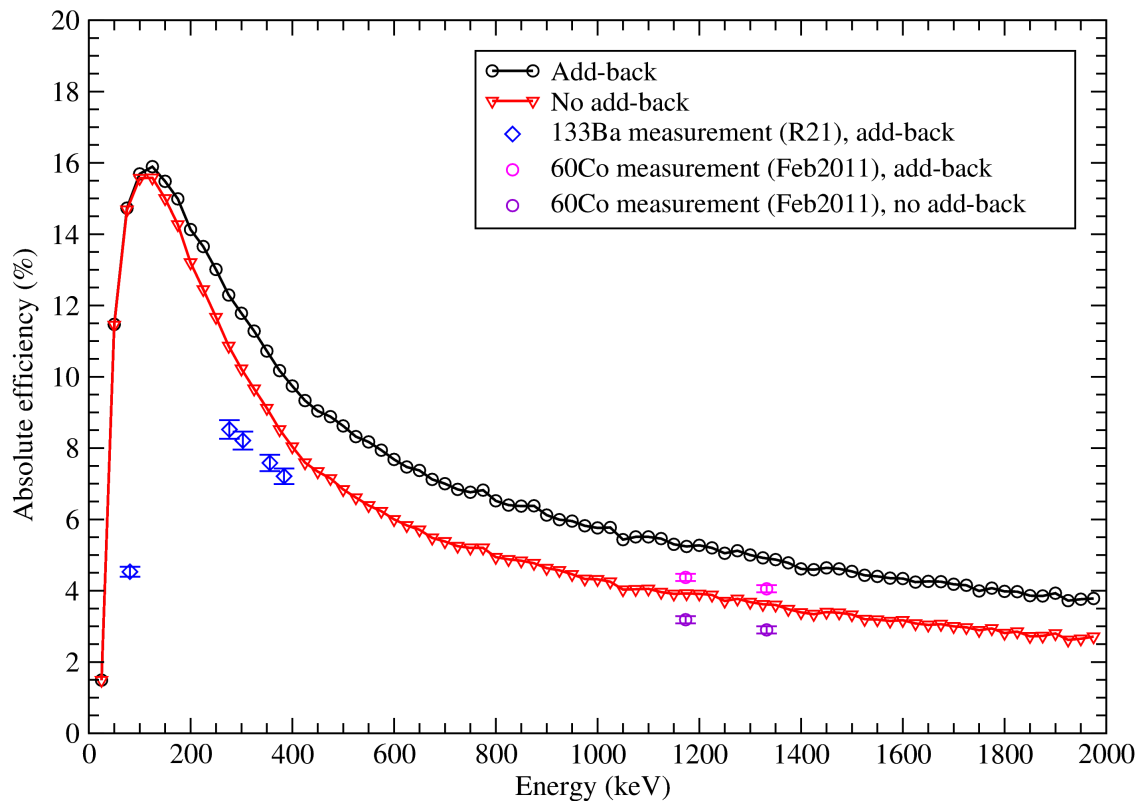


Figure 5.1: The simulated absolute photopeak efficiency of JUROGAM II and the measured efficiencies (with add-back) determined using sealed and calibrated  $^{133}\text{Ba}$  and  $^{60}\text{Co}$  sources.

closer to the end-caps. The efficiency of the GASP type detectors is better than that of the Phase 1 type detectors. Still, the correspondence between the measured values and the simulated curve is quite good and the shape of the curve is nicely reproduced.

Using the coincidence sum-peak analysis method (see e.g. [57, 58], and its usual applications to determine source activities [59, 60, 61]) and a  $^{60}\text{Co}$  source to determine the efficiency of the detectors at 1.3 MeV would eliminate the effects of dead-time, pile-up and other issues and would give a somewhat higher value for the efficiency. Usually the efficiencies that are reported for large arrays of germanium detectors are determined using this method, giving the most optimistic value. The exact value for JUROGAM II was not determined in this work using the sum-peak method, but is known to give a value of about 5.5-6.0% for the full JUROGAM II array. This value is very close to the estimates given here by the Geant4 simulation, when the contribution of the 5 Phase 1 detectors is taken into account. However, it is not that straightforward or justified to determine the efficiency for this array using the coincidence sum-peak method, because of the Clover detectors and the use of the add-back method for the crystals.

## 5.2 The efficiency of detecting electrons from a $^{133}\text{Ba}$ source

The decay scheme of  $^{133}\text{Ba}$  to the daughter nucleus  $^{133}\text{Cs}$  via electron capture from the Table of Isotopes [62] is presented in Figure 5.2 to assist in the following discussion of how to determine the efficiencies from a measurement of a  $^{133}\text{Ba}$  source.

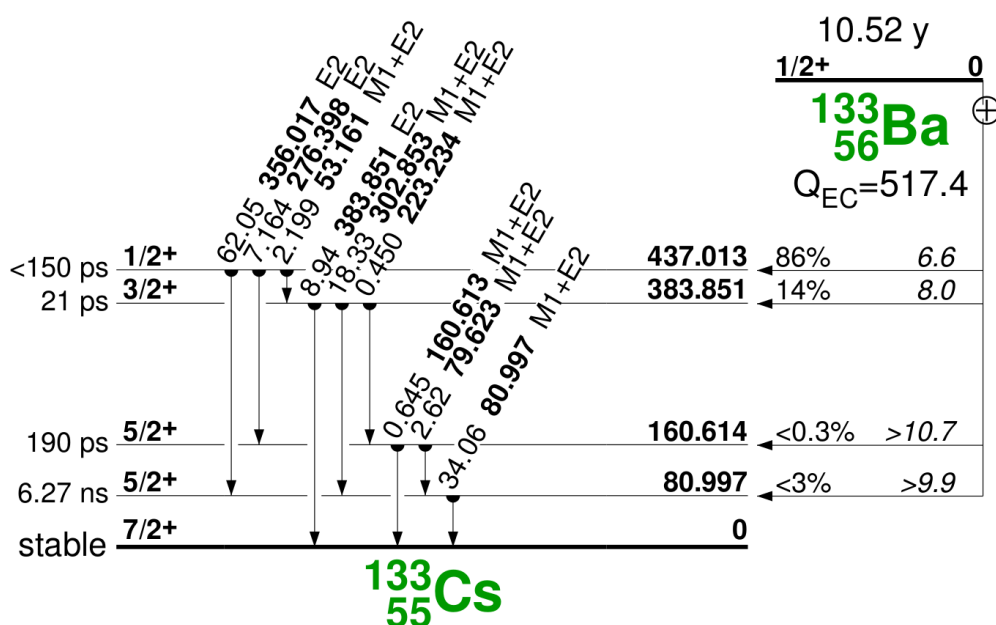


Figure 5.2: The experimental decay scheme of  $^{133}\text{Ba}$  from the Table of Isotopes [62].

In this work, the absolute intensities of the internal conversion electrons and gamma rays that are emitted from  $^{133}\text{Cs}$  following a decay of  $^{133}\text{Ba}$  and their uncertainties were adopted from the recommended experimental intensities presented in an article by Trzaska [63] from the year 1990. In many cases, the electrons emitted from, for example, different  $L$  shells  $L_1, L_2, L_3$  cannot be distinguished in these measurements because of the limited energy resolution of the used silicon detector, so the intensities corresponding to the same transition but from different atomic shells had to be summed. Similarly, the peaks can contain events, in which electrons are emitted from different transitions and different atomic shells, such that the final kinetic energy of the electrons are almost equal and again cannot be resolved in a measurement. A typical energy resolution in the measurements was about 4-5 keV (FWHM) at 320 keV.

The measured absolute efficiencies were determined from the measurements of an open  $^{133}\text{Ba}$  source without applying voltage at the HV barrier and also with a voltage of  $-25$  kV. The JUROGAM II array was closed in both measurements. The beam collimator in the detector chamber was modified in such a way that the detector could be moved closer to the beam axis and the source was placed about 4 mm higher to get a centred electron distribution at the detector. From the measurement of the calibrated  $^{133}\text{Ba}$  gamma-ray source it was possible to determine the efficiency of the JUROGAM II array to detect the 356 keV gamma rays,  $\epsilon(356 \text{ keV}) = (7.6 \pm 0.3)\%$ . Using the known gamma-ray detection efficiency, the unknown activity of the open source could then be determined by measuring the gamma-ray yield from the source with the JUROGAM II array and using Equation (2.16). The error was estimated from the derived Equation (2.27). The final result for the activity of the open  $^{133}\text{Ba}$  source was  $(147 \pm 5)$  kBq.

The electron detection efficiencies were calculated using Equation (2.15) and the error was estimated from the derived Equation (2.24). The experimental intensities from [63] were used, and summed to include all atomic shells for a given measured energy, if necessary. The final results without applied voltage at the HV barrier are shown in Figure 5.3 for energies 0-500 keV and in Figure 5.4 for energies 0-1000 keV. The efficiencies obtained with a voltage of  $-25$  kV at the HV barrier are shown in Figures 5.5 (0-500 keV) and 5.6 (0-1000 keV). In both cases, the measurement points at 45 keV have very large error bars due to background radiation due to e.g. bremsstrahlung and backscattering of the electrons from the detector causing difficulties in determining the areas of the peaks. The peaks actually have more fine-structure in them than only the 45 keV electrons from the open source.

An equation of the form

$$\epsilon(E_e) = A(1 - \sqrt{B/E_e}) \exp(-CE_e), \quad (5.1)$$

was fitted to the measurement points to guide the eye, where  $A$ ,  $B$  and  $C$  are parameters. The energy  $E_e$  was given in units of keV and the efficiencies in percent. This functional form without the exponential part was suggested in an article of SACRED by Butler et al. [2] for the effect that the HV barrier has on the detection efficiency (the factor  $B \approx$  the applied voltage at the barrier), but was lacking the proper exponential decay behaviour of the measured efficiency curves. For this reason, the exponential function was added. In addition, the measured efficiencies for detecting very low-energy electrons has to go to zero (and not to infinity), because of threshold, noise and other practical reasons, which gives a constraint for the parameter:  $B > 0$ .

The simulated electron detection efficiencies were determined by emitting 100 000 electrons of each energy (in 25 keV steps) in the 25-1000 keV energy range from the target position using a uniform angular distribution. The efficiencies corresponding to the conversion electron energies from  $^{133}\text{Ba}$  source were simulated separately using the experimental energies and 100 000 events of each energy were calculated. The number of detected electrons depositing their energy in the full energy peak were determined after a gaussian skew was applied to the spectrum in the analysis program to simulate an intrinsic resolution of 4 keV. The same settings for the coil current (800 A) and HV barrier (no HV voltage and  $-25$  kV) were used as in the measurement, the silicon detector was placed at  $2.6^\circ$  to make the distribution more centred as in the measurement. Realistic vacuum conditions (air at  $10^{-6}$  mbar) were used in the detector and target chambers without the helium and the CF unit. The earlier mentioned model of the source geometry was not included in these simulations to be able to focus mainly on the effect that the HV barrier has.

The numerical values of the efficiencies determined from the measurements and simulations are presented in Table 5.1. The experimental and simulated results in Figures 5.3-5.4 coincide remarkably well when the HV barrier is not used, especially at energies above 200 keV. However, at low energies the experimental efficiencies drop because of the limitations caused by electronics and noise. These problems are not present in the simulation and as a consequence of this the simulated efficiency is much higher.

Turning on the voltage at the HV barrier effectively reduces the efficiencies at low energies below 200 keV as can be seen in Figures 5.5-5.6. The energy threshold caused by this type of a barrier is not a straight cut, but rather a smooth adjustment to the low-energy end of the curve. Here, the simulated curve follows the shape of the measurement points very well especially at low energies. At energies higher than 200 keV the curves deviate

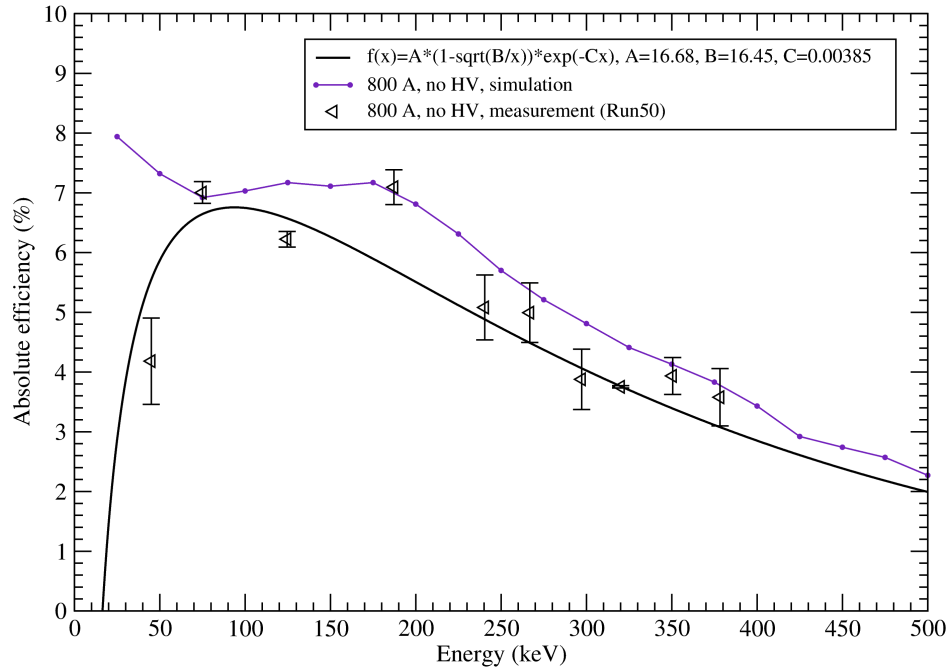


Figure 5.3: The measured absolute electron detection efficiency of SAGE obtained from a  $^{133}\text{Ba}$  source and compared to an efficiency curve from a simulation. A fit was made to the measured data to guide the eye. The current in the coils was 800 A and the HV barrier was not used. See text for more details.

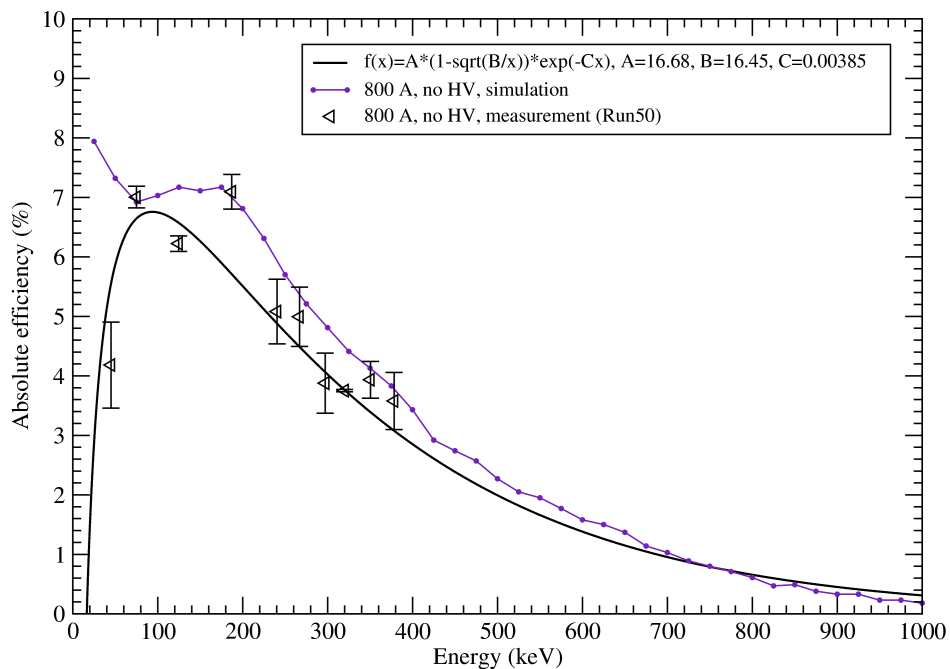


Figure 5.4: The measured absolute electron detection efficiency of SAGE obtained from a  $^{133}\text{Ba}$  source and compared to an efficiency curve from a simulation for energies 0-1000 keV. A fit was made to the measured data to guide the eye. The current in the coils was 800 A and the HV barrier was not used. See text for more details.

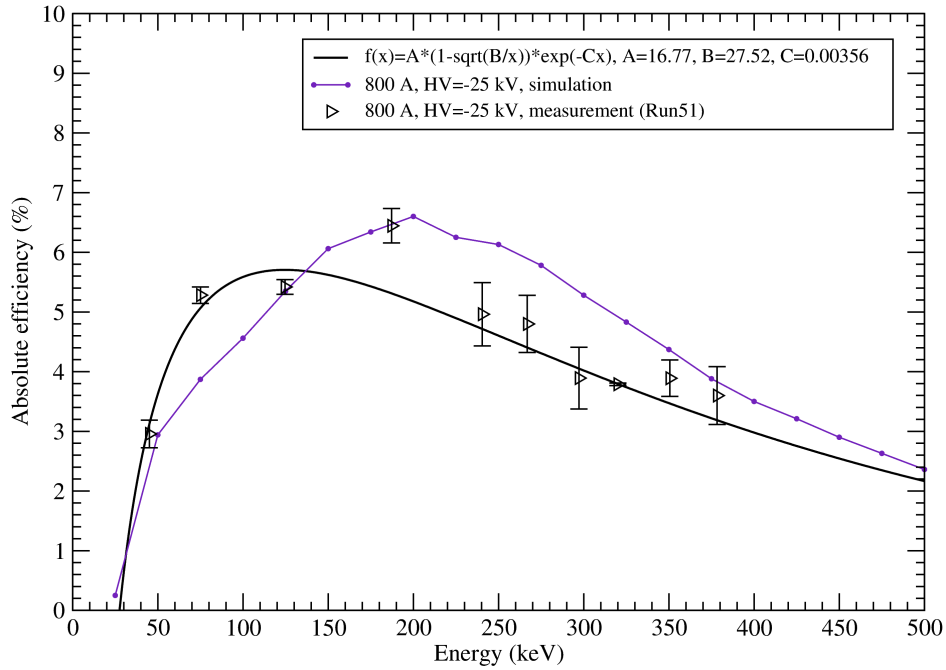


Figure 5.5: The measured absolute electron detection efficiency of SAGE obtained from a  $^{133}\text{Ba}$  source and compared to an efficiency curve from a simulation. A fit was made to the measured data to guide the eye. The current in the coils was 800 A and the voltage at the HV barrier was  $-25$  kV. See text for more details.

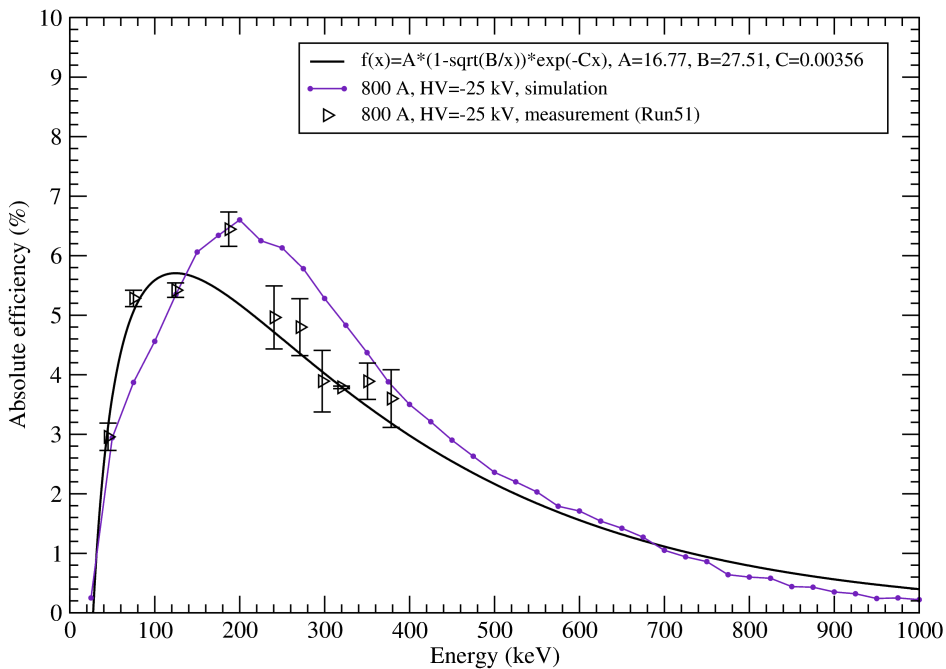


Figure 5.6: The measured absolute electron detection efficiency of SAGE obtained from a  $^{133}\text{Ba}$  source and compared to an efficiency curve from a simulation for energies 0-1000 keV. A fit was made to the measured data to guide the eye. The current in the coils was 800 A and the voltage at the HV barrier was  $-25$  kV. See text for more details.



Table 5.1: The simulated and measured electron detection efficiencies  $\epsilon$  for different energies, and the absolute intensities of electrons emitted from a  $^{133}\text{Ba}$  source adopted from [63].

Energy (keV)	Intensity	HV off (Run50)		HV -25 kV (Run51)	
		sim $\epsilon$ (%)	exp $\epsilon$ (%)	sim $\epsilon$ (%)	exp $\epsilon$ (%)
45	0.47946	7.5	$4.1 \pm 0.8$	2.6	$3.0 \pm 0.3$
75	0.07156	7.2	$7.0 \pm 0.2$	4.0	$5.28 \pm 0.14$
124.628	0.001427	7.5	$6.22 \pm 0.14$	5.4	$5.42 \pm 0.13$
187.249	0.000324	7.4	$7.1 \pm 0.3$	6.6	$6.4 \pm 0.3$
240.413	0.00328	6.5	$5.1 \pm 0.6$	6.2	$5.0 \pm 0.6$
266.868	0.00692	5.8	$5.0 \pm 0.5$	5.8	$4.8 \pm 0.5$
297.2	0.001	5.3	$3.9 \pm 0.6$	5.3	$3.9 \pm 0.6$
320.032	0.01308	4.9	$3.75 \pm 0.02$	4.9	$3.79 \pm 0.04$
350.5	0.0037	4.3	$3.9 \pm 0.4$	4.3	$3.9 \pm 0.4$
378.3	0.000255	3.8	$3.6 \pm 0.5$	3.9	$3.6 \pm 0.5$

more, and the simulated curve does not quite fit inside the error bars of the measurement points.

As an example showing the effect of the HV barrier, the efficiency difference at 75 keV with and without the HV barrier is about 30% in the measurement and 40% in the simulation. This effect is demonstrated in the measured source spectra of Figure 5.7. The length of the measurements was different, but the spectra were normalised using the 320 keV peak area. This can be done, because the efficiency at 320 keV remains nearly constant even with the HV barrier turned on, as can be seen in Table 5.1. It can be clearly seen that the HV barrier is working and the 45 keV peak is suppressed much more than the 75 keV peak, indicating a smooth effect on the efficiency. The barrier affects also electrons with energies higher than the potential at the barrier, depending on the angle of the incident electron and edge effects of the field.

At higher energies the simulated efficiencies are slightly higher than the experimental values, but it should be remembered that the simulation gives an upper limit of what can be achieved in an ideal situation. Another thing is that the analysis of real measurement data is more complicated than the data from the simulations. A more realistic simulation in this case would be to simulate a decay of  $^{133}\text{Ba}$ , apply an intrinsic resolution to each detector, take into account the electronics related effects and noise and then analyse the data using the same methods as with the measured data. For the high energy part of the curves, more measurement points are needed to check the validity of the simulation at high energies and to make a better fit to the experimental data. This could be done, for example, with an open  $^{207}\text{Bi}$  electron source that has a maximum energy for the emitted electrons at about 1 MeV.

It is not surprising that the experimental and simulated results do not agree perfectly at low energies, because the Geant4 package was initially developed for high energy physics. Nevertheless, considering that this is a simulation of a very complex device employing electric and magnetic fields and many mechanical components that can never be modelled or placed exactly as they are in reality, the Geant4 simulation package of SAGE works very well. It re-produces the experimental results overall very closely. Even when the fields and the geometry are adjusted only a little, the differences can be seen in the simulated results immediately.

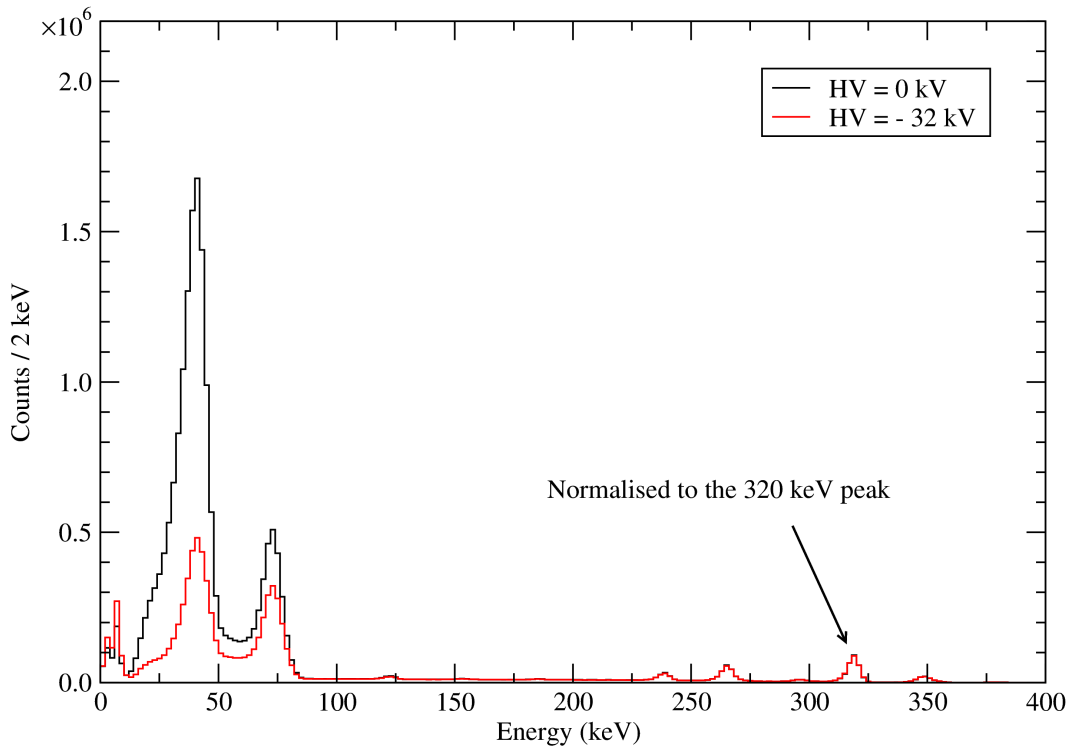


Figure 5.7: The measured  $^{133}\text{Ba}$  source singles spectrum with the HV barrier at 0 and  $-32$  kV voltage. The two spectra were normalised using the 320 keV peak area, because the measurement time was different.

Because the low-energy part of the electron singles spectrum is contaminated with background events from backscattering, X-rays, bremsstrahlung and other effects, the fitted area of the 45 keV peak is not accurate. The uncertainty in the peak area can make a very large difference in the value obtained for the efficiency. The efficiency at 45 keV can be determined more accurately by looking at electron-gamma coincidences if the measurement time is long and the coincidence signature is strong “enough”, similar to the gamma-gamma coincidences [64, 65, 66]. The measured electron detection efficiencies for the low-energy electrons at 45 keV were cross-checked using electron-gamma coincidences.

All the measured coincident events of the type electron-gamma or electron-electron were sorted into an e-g or e-e matrix, respectively. The electron-gamma matrix from the measurement with  $-25$  kV at the HV barrier can be seen in Figure 5.8(a) and the electron-electron matrix in Figure 5.8(b). A time gate of 400 ns was used as a condition for the events to be accepted as coincident signals. This is a quite wide time gate, as most of the events in the electron-gamma time spectrum were well within a 200 ns window. Using too wide a time gate can increase the background but on the other hand ensures that also the low-energy signals are counted in the spectra.

The projection of the measured gamma-ray energies from Figure 5.8(a) is presented in the upper part of Figure 5.9. The good energy resolution of the germanium detectors is not apparent in the electron-gamma matrix, because of the scale chosen for the z-axis such that the channels with low number of events are visible. The energy resolution (FWHM) in the projection to the gamma-ray energy axis is about 2.5 keV at an energy of 356 keV. When an energy gate is placed at the gamma-ray energy of 356 keV, the lower spectrum of coincident electrons can be projected from the matrix. The insert shows the very low back-

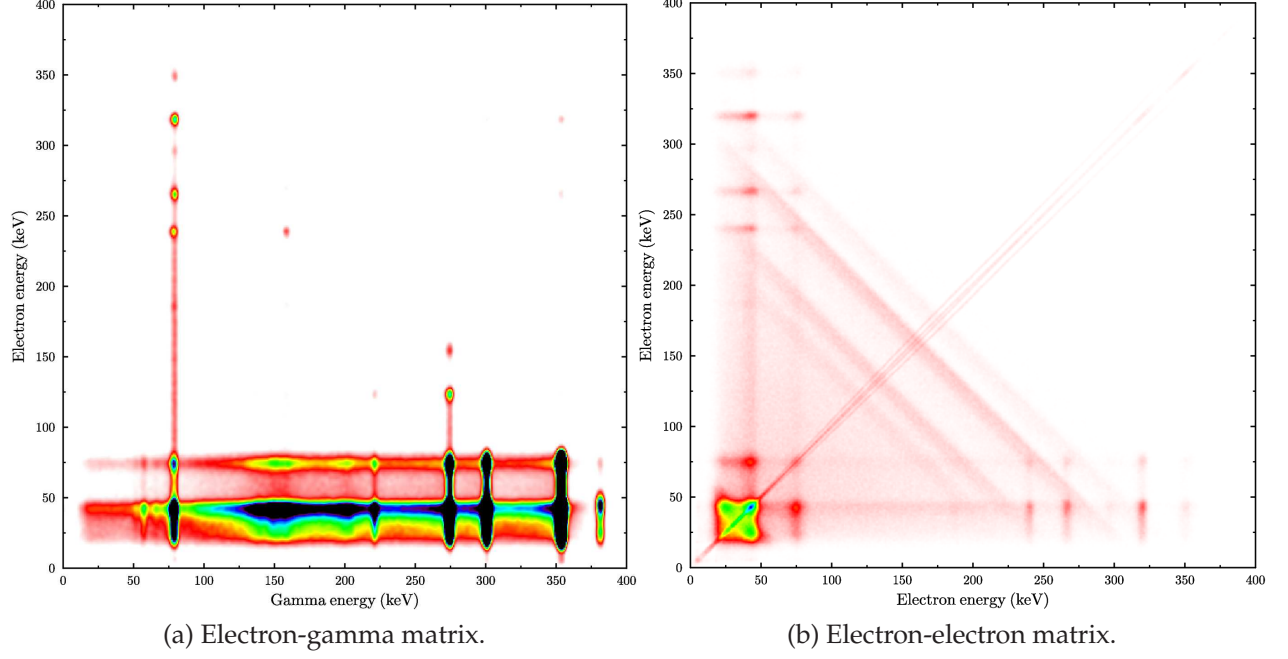


Figure 5.8: Coincidence matrices of (a) electron-gamma and (b) electron-electron from the measurement of the open  $^{133}\text{Ba}$  source with  $-25$  kV at the HV barrier. The darker the colour is, the more events there are.

ground relative to the 45 and 75 keV peaks. Notice that these two peaks still contain fine structure, but now both of the peaks correspond to an event where the 356 keV transition to the first excited state in  $^{133}\text{Cs}$  decays by internal conversion, with the electron emitted either from the  $K$  (45 keV) or the  $L$  shell(s) (75 keV).

The absolute intensity for the decays to result in the emission of a 356 keV gamma ray can be seen in Figure 5.2 and is about  $I_\gamma(356) = 0.6205$ . The intensity of the coincidence signatures  $I_{e+\gamma}$  can be calculated from the known experimental conversion coefficients of the transition (80.997 keV) from the first excited  $5/2^+$  state to the  $7/2^+$  ground state [63]. For the transition where the electron is emitted from the  $K$  shell, it is

$$I_{e+\gamma}(45 + 356) = I_\gamma(356) \cdot \frac{\alpha_K}{1 + \alpha_K + \alpha_L} \approx 0.319, \quad (5.2)$$

and for the  $L$  shell

$$I_{e+\gamma}(75 + 356) = I_\gamma(356) \cdot \frac{\alpha_L}{1 + \alpha_K + \alpha_L} \approx 0.049. \quad (5.3)$$

In this simple case, the number of events that are expected in the gamma-gated electron spectrum and in the peak corresponding to the (356 keV gamma ray + 45 keV ( $K$ ) electron) coincidence signature can be written as

$$N_{e+\gamma}(45 + 356) = A \cdot \Delta t \cdot I_{e+\gamma}(45 + 356) \cdot \epsilon_\gamma(356) \cdot \epsilon_e(45) \cdot W(\theta), \quad (5.4)$$

where  $A$  is the activity of the source,  $\Delta t$  is the measurement time,  $\epsilon_\gamma(356)$  is the gamma-ray detection efficiency at 356 keV,  $\epsilon_e(45)$  is the electron detection efficiency of 45 keV electrons and  $W(\theta)$  is the angular correlation function with  $\theta$  as the angle between the

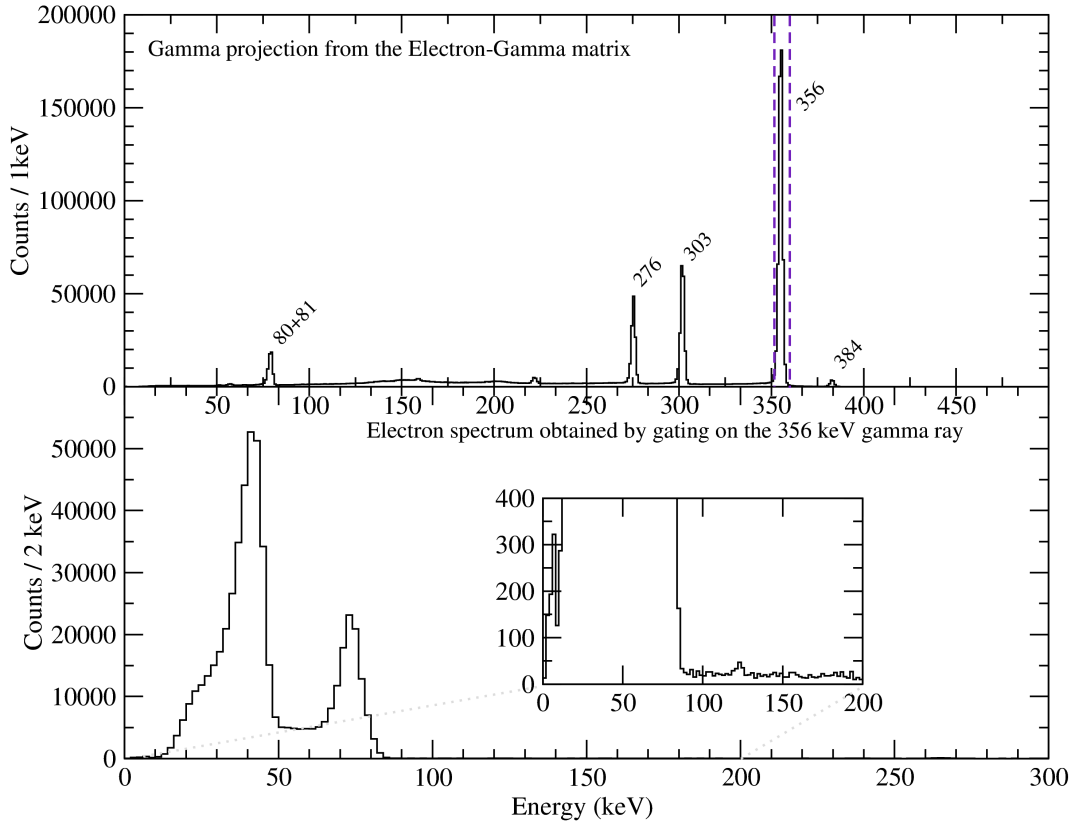


Figure 5.9: A projection of the gamma-ray energies in coincidence with the electron energies from the open  $^{133}\text{Ba}$  source with the HV barrier at  $-25$  kV voltage (up) and the resulting electron energy spectrum when a gate is placed at the 356 keV gamma-ray energy (down). The insert shows the low background relative to the 45 and 75 keV peaks.

emitted gamma ray and the electron. A similar equation for the number of events where the 356 keV gamma ray and 75 keV electron are detected in coincidence can be written.

Now, by taking the ratio of the number of counts in the peaks of the gamma-gated electron spectra, some of the factors cancel out and the efficiency to detect 45 keV electrons can be solved to be

$$\epsilon_e(45) = \frac{N_{e+\gamma}(45 + 356) \cdot I_{e+\gamma}(75 + 356)}{N_{e+\gamma}(75 + 356) \cdot I_{e+\gamma}(45 + 356)} \cdot \epsilon_e(75). \quad (5.5)$$

The electron detection efficiencies at 45 keV determined from the electron-gamma coincidence spectra and using Equation (5.5) are 4.6% (800 A, no HV, Run50) and 2.4% (800 A, HV  $-25$  kV, Run51). The values are about the same as were determined from the singles sum spectra in Figures 5.3 and 5.5 and in Table 5.1. The latter one using the electron-gamma method corresponds more closely to the simulated curve than the one in the figure.

### 5.3 The simulated and measured peak-to-total ratios of the JUROGAM II germanium detectors

As an example of the effect of Compton suppression, a measured  $^{60}\text{Co}$  spectrum using one of the Clover detectors of the JUROGAM II array is shown in Figure 5.10(a). The add-back method was used in the measurement. The spectrum is very similar to those obtained with a Phase 1 detector using Compton suppression shields as in [66, Fig. 2, pp. 529]. A simulated  $^{60}\text{Co}$  spectrum using  $1 \cdot 10^7$  events and one of the Clover detectors from the array is shown in Figure 5.10(b) for comparison. A realistic intrinsic detector resolution of about 3 keV at an energy of 1.3 MeV was applied to the simulated spectrum.

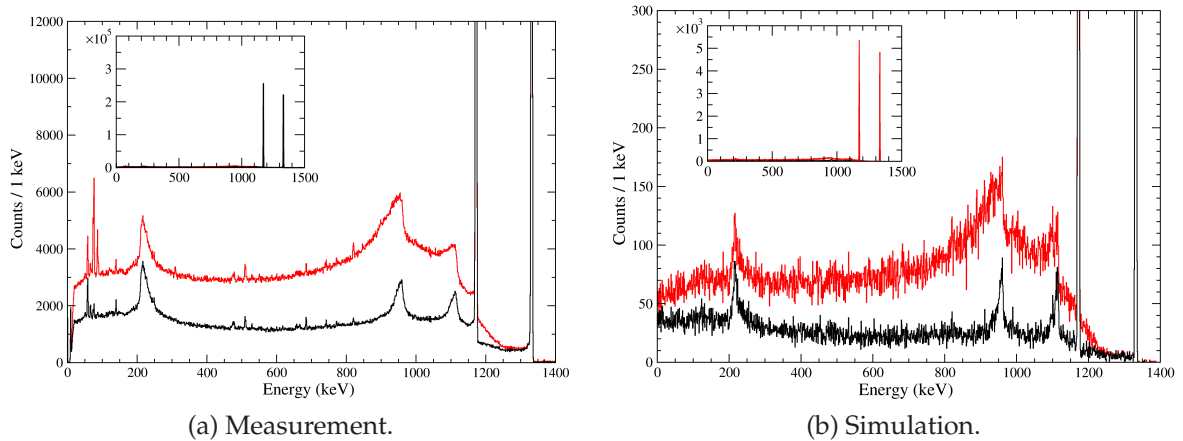


Figure 5.10: Unsuppressed (red) and suppressed (black)  $^{60}\text{Co}$  spectra obtained with a Clover detector using add-back from (a) a measurement and (b) a simulation. The y-axis has been rescaled to show the Compton continuum. The inserts show the photopeaks relative to the background.

The measured peak-to-total ratios were determined in a comprehensive study by looking at every JUROGAM II detector spectrum individually, with and without Compton suppression from the BGO shields, with and without pile-up rejection done by the ADC (analog-digital-converter) and with and without using add-back for the Clover detectors. At the same time, the peak efficiencies for the two gamma rays of  $^{60}\text{Co}$  were determined individually for each detector as well as for the whole array when using 10 Phase 1 and 24 Clover detectors. The efficiencies are presented in Figure 5.1.

The final results for the peak-to-total ratios were determined using Equation (2.19), and are given for the Phase 1 and Clover detectors using add-back, with pile-up rejection and Compton suppression enabled, and compared to the ratios without Compton suppression. The errors were estimated using Equation (2.28) obtained from the law of error propagation. Although the peak-to-total ratio is actually an individual property of each detector, an error weighted average using Equation (2.20) was taken of all the results for the detectors to be able to give one final result. The error for this average is given more realistically by the standard deviation of a single value in the ensemble, rather than the very small final error given by the uncertainty of the weighted average in Equation (2.22).

The measured values for the peak-to-total ratios using Compton suppression are for the Clover with add-back ( $0.43 \pm 0.03$ ) and Phase 1 ( $0.48 \pm 0.02$ ). Without Compton suppression the ratios are: Clover with add-back ( $0.237 \pm 0.012$ ) and Phase 1 ( $0.24 \pm 0.01$ ).

In the simulation,  $1 \cdot 10^7$  events of  $^{60}\text{Co}$  decays were used and the event data was analysed afterwards. The analysis program created the individual Clover histograms with and without BGO vetoes using add-back, and the peak areas and integrals were determined using Grain. There is an artificial 20 keV low-energy threshold for the BGO vetoes in the analysis program, which means that if the energy detected by the BGO crystal is lower than the threshold, the corresponding germanium is not vetoed in the corresponding event. All of the crystals inside one Clover BGO shield are used to veto events from every germanium crystal of that detector, as is currently done in the measurements. The spectra from the simulation are relatively simple, because the peak is essentially a discrete line and there are no other background sources present in the simulation, which makes the analysis of the histograms very simple. The uncertainties were estimated from the small statistical fluctuations of the results.

The simulated values for the peak-to-total ratios using Compton suppression are for the Clover with add-back ( $0.525 \pm 0.003$ ) and Phase 1 ( $0.487 \pm 0.003$ ). Without Compton suppression the ratios are: Clover with add-back ( $0.279 \pm 0.003$ ) and Phase 1 ( $0.229 \pm 0.003$ ). The values are presented in Table 5.2 with the measured values for ease of comparison.

Table 5.2: The peak-to-total ratios of the germanium detectors determined with and without Compton suppression from measurements and simulations of a  $^{60}\text{Co}$  source.

Detector	Simulation		Measurement	
	no veto	veto	no veto	veto
Phase 1	$0.229 \pm 0.003$	$0.487 \pm 0.003$	$0.24 \pm 0.01$	$0.48 \pm 0.02$
Clover	$0.279 \pm 0.003$	$0.525 \pm 0.003$	$0.237 \pm 0.012$	$0.43 \pm 0.03$

It should come as no surprise that the simulated values are usually slightly better than those obtained from real measurements. The results coincide very well for the Phase 1 detector, but not so well for the Clover detector with Compton suppression. It could be either that the germanium crystals of the Clover are modelled badly giving an efficiency which is too high or the BGO crystals have been modelled with a too large volume, giving too much Compton suppression. The simulation does not take into account any electronics, ageing or performance of the photomultiplier tubes, but it still does not give too optimistic results. Some adjustment was made by including the low-energy threshold in the simulation, because this is present to some extent in real life as well. Currently the simulation does not include false vetoes or pile-up detection due to only one decay created in an event, which means that the simulation keeps track of time only with the event numbers. The energies measured by the detectors are not timestamped inside one event. The peak efficiency of the detectors in the simulation is higher at all energies than in reality as can be seen in Figure 5.1. Therefore, the efficiency should not have such a large effect on the simulated peak-to-total ratios, and the more likely cause for the discrepancy is in the model of the Compton suppression shield.

The results obtained for the Phase 1 detector corresponds very well to reality, which can mean that the model of the BGO crystal shape and volume may be realistic in the simulation. On the other hand, earlier reports about the Phase 1 BGO shield performance give much better estimates for the peak-to-totals (0.55 to 0.58, see e.g. [67] and 0.57 in [23] and other EUROGAM related articles). For the Clover detector, a measured peak-to-total

without a BGO shield of 0.30 and with Compton suppression 0.55 are given in [24]. These values are better than those obtained from the measurements, but are close to the simulated values.

The location of the measurements are usually not given precisely in the literature. The environment contributes to the number of counts in the background because of scattered gamma rays, among other effects. If the measurement to determine a peak-to-total ratio is made in a large airplane hangar with the germanium detector hanging in the middle of it, the results are bound to be very optimistic compared to a real situation where tens of detectors are packed close to each other in a large solid block of steel acting as a supporting structure. In addition, the concrete walls of a laboratory can contain contaminants such as  $^{40}\text{K}$ , which contributes to the number of counts in the Compton continuum of the spectrum. Nevertheless, the measured ratios are worse than previously reported values for the similar EUROGAM arrays, which may be due to ageing of the PMTs or BGO crystals, parameters in the data acquisition, electronics or other issues.

## 5.4 The effect of the solenoid magnetic field on the performance of JUROGAM II

In order to verify that the magnetic field produced by the solenoid coils does not affect the operation of the photomultiplier tubes in the Compton suppression shields of the Phase 1 detectors, measurements of a  $^{60}\text{Co}$  source were carried out using different currents in the coils. All of the measurements performed with the weak  $^{60}\text{Co}$  source and varying the magnetic field were measured for the same length of time (20 min 15 s). This makes the results directly comparable. The currents in the coils were 0, 250, 500 and 700 A and the passive shielding was in place around the coils. The Compton-suppressed sum spectra of the first ring of Phase 1 detectors located closest to the main coil are presented overlaid in the same plot in Figure 5.11 and in Figure 5.12 the same spectra are arranged separately. It can be seen that there are no major differences in the spectra, which means that the performance of the Compton suppression shields is not weakened at all by the magnetic field produced by the solenoid coils of SAGE.

There is really no need to determine any numerical values for the peak-to-totals in this case, because the values would be almost exactly the same. Using the weak source leaves a lot of background peaks in the spectrum such as the 1461 keV peak of  $^{40}\text{K}$ , that shows up very well in Figures 5.11 and 5.12, due to the use of the logarithmic scale. There are also  $^{133}\text{Ba}$  peaks due to some contamination (few hundred becquerel) that was present in the target chamber, probably originating from the use of the open source at some earlier time.



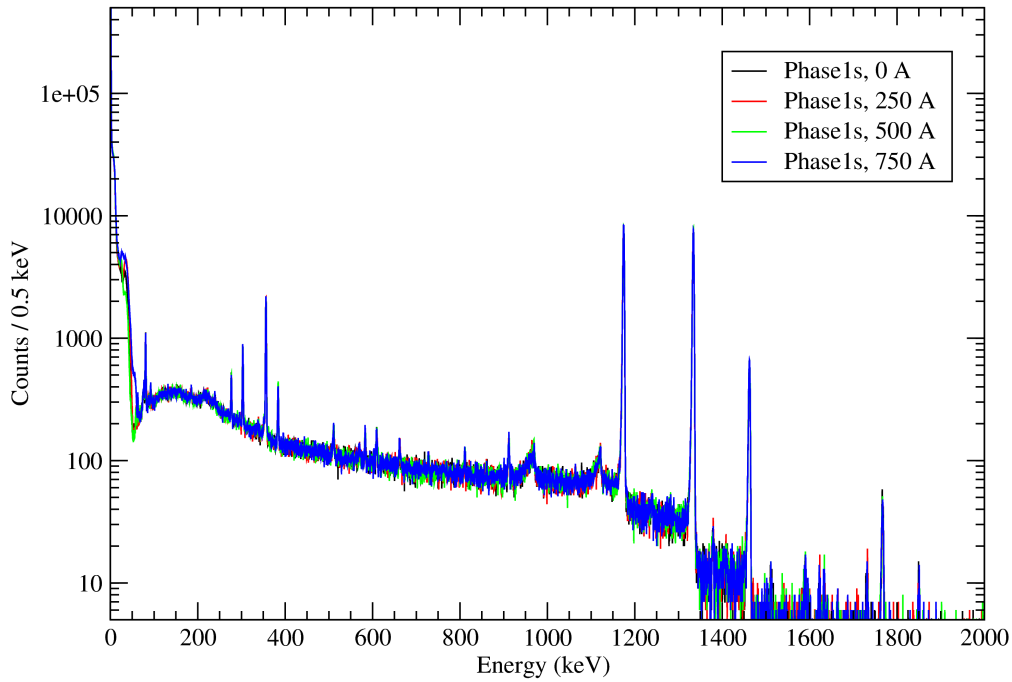


Figure 5.11: The Compton-suppressed sum spectra of the first ring of 10 Phase 1 detectors with different currents in the coils from a measurement of a weak  $^{60}\text{Co}$  source overlaid. Measurement time was the same in every case, see text for details.

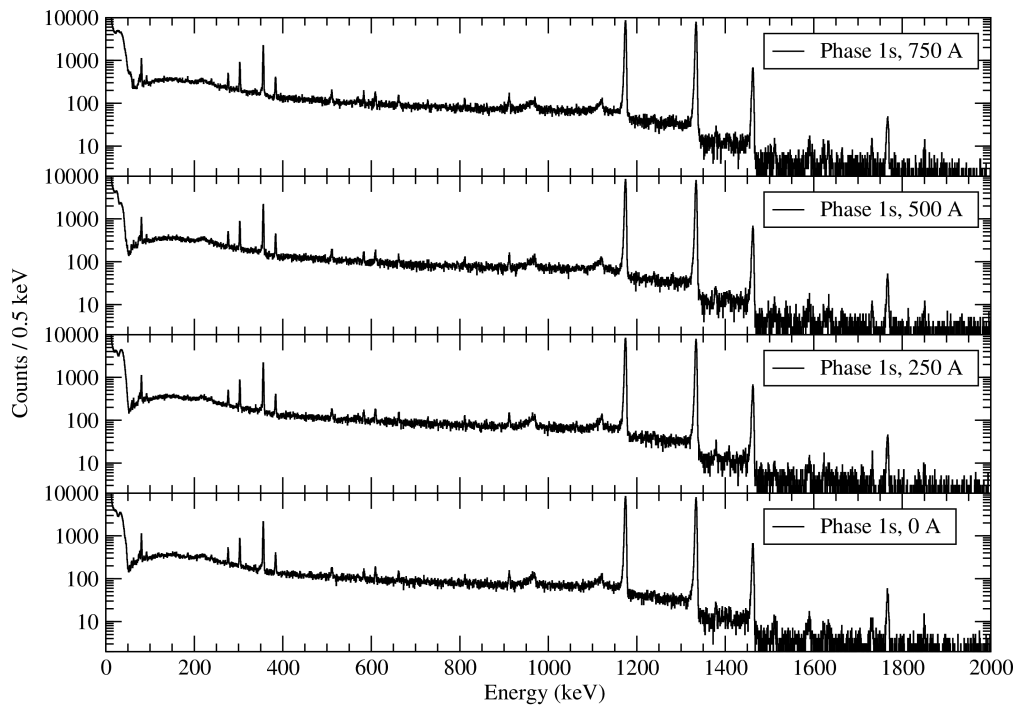


Figure 5.12: The Compton-suppressed sum spectra of the first ring of 10 Phase 1 detectors with different currents in the solenoid coils from a measurement of a weak  $^{60}\text{Co}$  source. The measurement time was the same in every case, see text for details.



## 5.5 Simulations of electron distributions at the detector and the effect of passive shielding

It was known from the SAGE commissioning run of 2010 and from the source measurement tests performed during the summer of 2011, that the electron distribution was not properly focused at the centre of the detector. The centre of the distribution was always somewhat to the south-west, even if the detector was properly aligned. This would cause problems with high count rates, because the larger pixels are hit by the high background of low-energy electrons.

When the Geant4 simulation package of SAGE became operational along with the tracking of electrons in the simulated electromagnetic field profiles, one of the first things to notice was that the electron distribution from the simulation was not focused at the centre of the silicon detector either. This was a remarkable achievement for the simulation, because it showed that the simulation functioned correctly as it reproduces the experimental result. Frankly, this result was not quite the one that was expected i.e. there was a minor error in the design or construction of the device.

In order to find out what was the main cause for the electron distribution being off-centre, the new Geant4 simulation could be easily used to try out different field profiles produced from *OPERA 3D*. Hitmaps as in Figures 5.13(a) and 5.13(b) were used to determine the centroids of the distributions, and the  $x$ -coordinates (measured from the beam axis) were extracted by fitting gaussian peaks to the distributions.

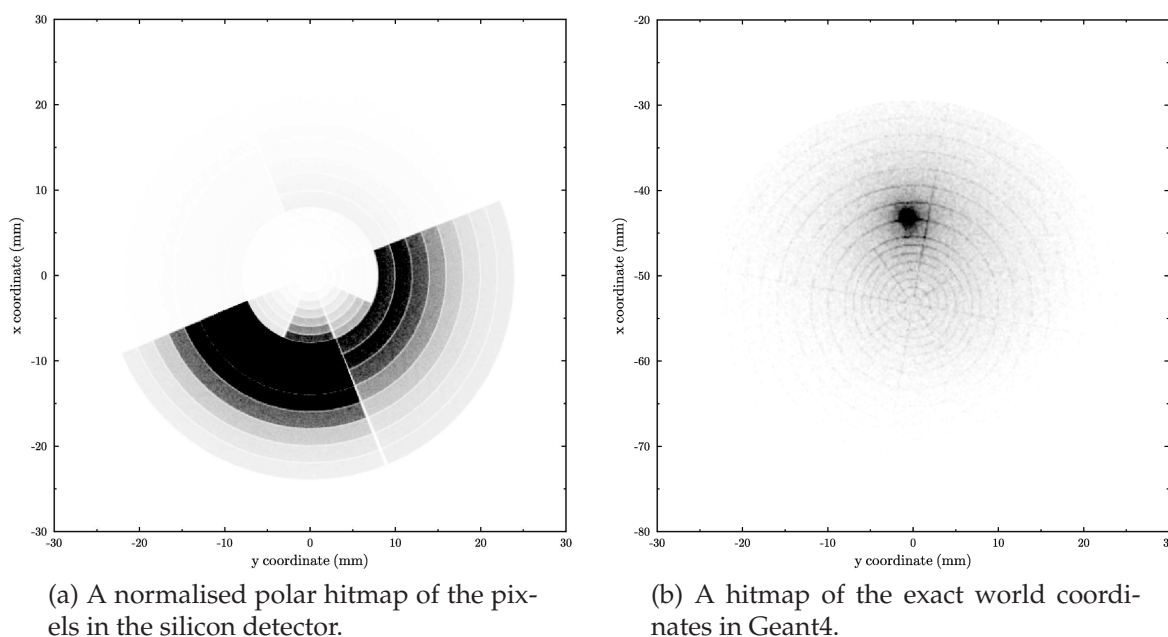


Figure 5.13: Two types of hitmaps from a simulation of a  $^{133}\text{Ba}$  source with the detector positioned at an angle of  $3.2^\circ$  to the beam axis. Coordinates are (a) with respect to the detector center, (b) with respect to the beam axis, the beam axis being at  $x = 0$ .

Many different kinds of slightly modified versions of the original field designs were investigated by simulating the emission of 300 keV electrons at the target location uniformly in every direction. 50 000 events were used in each case to give a reasonable level of statistics to be able to determine the  $x$ -coordinates of the distribution centroids as well as an

estimate of the detection efficiency at an energy of 300 keV. All the results are presented in Table 5.3. In the simulations, the electric field produced by the HV barrier was set to 0 V and the CF unit and helium were not present in the chamber. In all cases, the silicon detector was at an angle of  $3.2^\circ$  with respect to the beam axis and 954.9 mm from the target, except in the tests with a collinear geometry (detector and whole geometry rotated to coincide with the beam axis). The centre of the detector was at  $x$ -coordinate  $-53.3$  mm (beam axis goes through  $x = 0.0$ ). It can be seen from the table that the electron distribution is focused about 10 mm off from the centre of the detector, towards the beam axis when all shields are in use. The  $x$ -coordinate of the focus point of about  $-43$  mm corresponds to having the detector at an angle of about  $2.6^\circ$ . A large drop in efficiency was also noticed in a measurement when no current was put through the downstream coil.

Table 5.3: Results for the distribution centroids, distance of the centroid to the centre of the detector  $\Delta$  and efficiencies at an energy of 300 keV from the simulations of various field profiles. Electric currents in the coils used in the field simulations are given with a description of what kind of passive shielding was used.

Main (A)	Down (A)	Up (A)	Shields	Eff. @ 300 keV (%)	Focus X (mm)	$\Delta$ (mm)
1000	1000	1000	all, collinear	–	–1.7	1.7
1000	1000	1000	no, collinear	–	0.0	0.0
1000	1000	1000	no	7.9	–48.4	4.9
1000	1000	1000	all	7.0	–42.9	10.4
1000	1000	1000	all	6.6	–42.6	10.4
700	700	700	all	3.9	–43.3	10.0
750	750	750	all	4.4	–43.7	9.6
800	800	800	all	5.3	–43.1	10.2
850	850	850	all	5.9	–43.1	10.2
900	900	900	all	6.0	–43.0	10.3
1000	1000	1000	no, continuous B	27.1	–48.6	4.7
1000	1000	1000	all, continuous B	30.9	–58.4	5.1
1000	750	1000	no main	3.3	–43.2	10.1
1000	1000	750	all	6.7	–40.1	13.2
1000	1000	750	no main	8.0	–39.2	14.1
1000	1000	1000	no main	6.3	–39.6	13.7
1000	500	500	all	1.6	–43.6	9.7
1000	500	500	no main	1.7	–41.3	12.0
1000	750	750	all	3.5	–43.6	9.7
1000	750	750	all	3.9	–39.3	14.0
1000	1000	1000	all, $2\times$ main	6.8	–46.4	6.9
1000	1000	1000	only dst.	7.9	–48.9	4.4
1000	1000	1000	only upst.	6.3	–39.4	13.9
1000	0	1000	all	0.6	–44.7	8.6
1000	0	1000	no main	0.7	–42.4	10.9
1000	1000	1000	all, rot. upstream	6.5	–51.3	2.0
1000	1000	500	all	8.7	–42.2	11.1
1000	1000	500	all, rot upstream	1.7	–53.3	0.0
1000	1000	1000	all, rot. on sol. axis	6.8	–51.0	2.3
1000	1000	1000	all, sol. axis, conic ds	6.6	–50.8	2.5

## 5.6 Simulations of the distribution centroid and the source location

One possibility to centre the electron distribution at the detector is to move the location of the target (i.e. source). The location of the source could be easily and accurately moved within the simulation, so the relationships between the distribution centroid and the  $x$ - and  $y$ -coordinates of the source were inspected. 10 000 events of 300 keV electrons emitted in random directions were used in these simulations and the source was moved in 1 mm steps first along the  $x$ -axis ( $y = 0$  constant) and then along the  $y$ -axis ( $x = 0$  constant). The detector was placed at an angle of  $3.2^\circ$ , which means that the centre of the detector was at  $x$ -coordinate  $-53.3$  (beam axis goes through  $x = 0.0$ ) in the current Geant4 coordinate system that is used in the simulation. No voltage was applied at the high-voltage barrier and the vacuum conditions were made nearly perfect in these simulations.

The results are presented in Figures 5.14 and 5.15. A linear relationship could be found in both cases near the center, so a linear fit was made to the linear part of the data points. From the simulations it can be seen that when the target is placed at the origin (0,0,0), the distribution centroid is at around  $x = -42$  mm and  $y = 0$  mm. This means that the centroid is hitting pixels 65 and 69 in the south-west corner of the detector as seen from the target position looking at the detector, because the detector is rotated slightly clockwise ( $10^\circ$ ) around its centre axis. These two channels were usually the two pixels with the highest count rate in the source measurements when the distribution was not perfectly centred. It was also noted that moving the source in the  $x$ -direction in such a way that the distribution is centred at  $-42... -55$  mm had very little effect on the detection efficiency, which was 5.0-5.8% in each case. At the both extreme ends, the distribution starts to fall off the edge of the detector, so the source was not moved any further away.

From the figures, it can also be deduced that in order to get the distribution centred at the detector, the source location would have to be moved by 6 mm in the same direction as the detector from the beam axis. This amount of adjustment is not possible by moving the source location alone. The detector could also be moved towards the collimator and closer to the beam axis by 11 mm to get the distribution centred, but here the restriction was the thick steel collimator that was almost touching the printed circuit board (PCB) of the silicon detector already. It was therefore necessary to design and construct a new, thinner collimator. Now, by moving both the target location only very little and the detector together, it was possible to achieve a horizontally centred distribution.

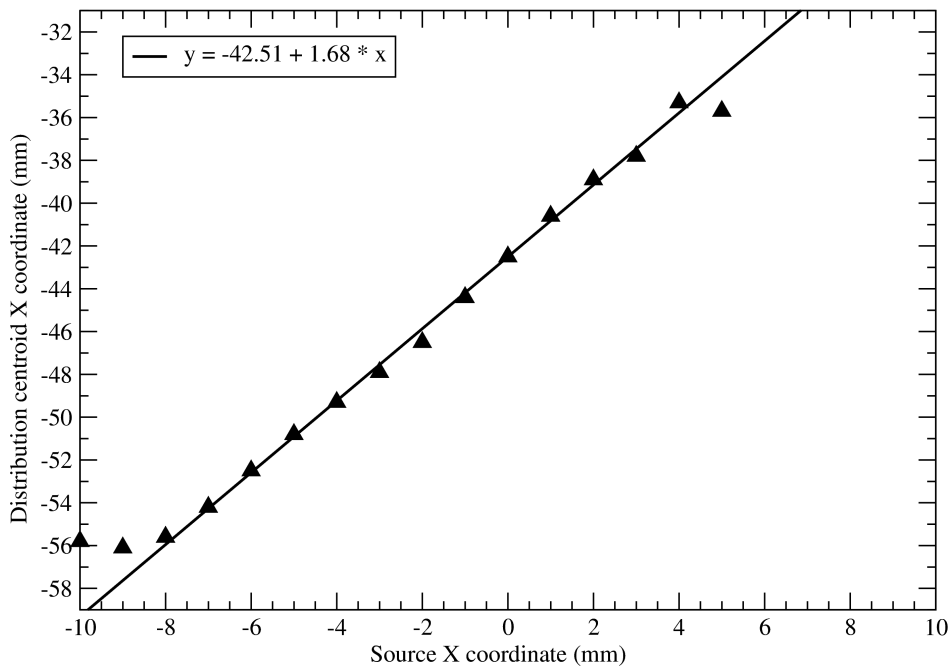


Figure 5.14: The relationship between the source  $x$ -coordinate the  $x$ -coordinate obtained for the centroid of the electron distribution. A linear fit was made to the clearly linear part of the data points.

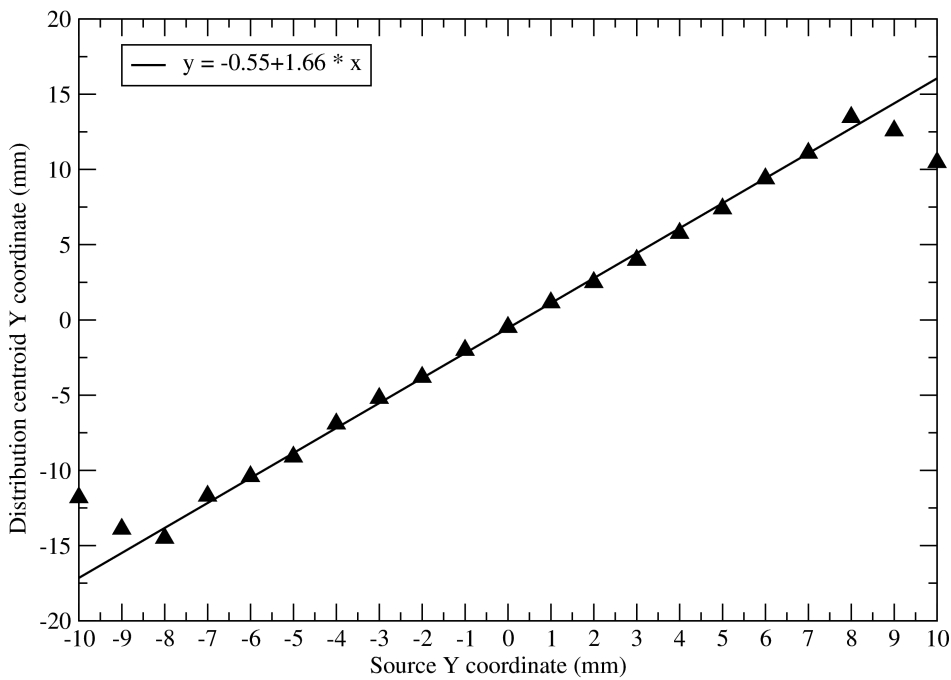


Figure 5.15: The relationship between the source  $y$ -coordinate and the  $y$ -coordinate obtained for the centroid of the electron distribution. A linear fit was made to the clearly linear part of the data points.

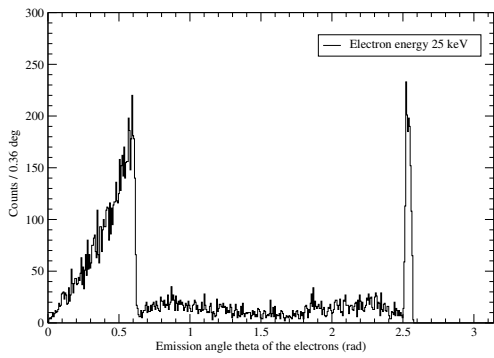
## 5.7 Simulated angular distributions of the electrons

It is unfortunate that it is not possible to determine the initial angular distributions of the emitted electrons, because they are measured at the silicon detector and the timing resolution of the system is not good enough. Currently, there is no way to get a signal for the emission of the electron at  $t = 0$  to be able to determine the time-of-flight. In addition, the magnetic bottle effect complicates things even more. However, in a Geant4 simulation it is possible to save the information about, for example, the initial direction and energy of the emitted electron. After the simulation, it is then possible to make various types of histograms in the analysis programs such as the sum of initial angles of the electrons that were detected by the silicon detector, matrices of the initial energy versus detected energy and more.

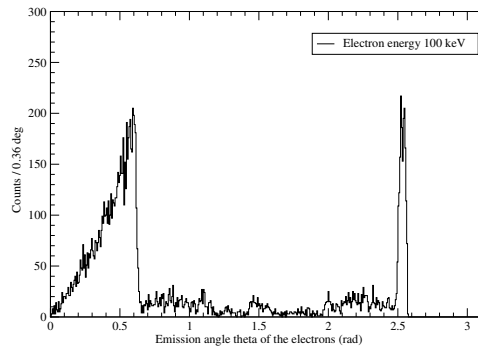
In order to get an idea of what the initial angular distribution of the electrons is, the initial  $\theta$  and  $\phi$  angles were saved with the event data whenever the electron was detected at the silicon detector. Energies from 25 to 1000 keV in 25 keV steps were used and 100 000 events per each energy were created and analysed individually for each energy. Some of the resulting initial angular distribution plots for different electron energies are shown in Figures 5.16(a)-5.16(f). In addition, the model of the source geometry similar to the one that is the container of the open  $^{133}\text{Ba}$  source was included at the target location. This is done to display the effect that the source material can have on the angular distribution and efficiency.

Including the source material in the simulation removes the rough edges in the angular distributions and makes them more smooth as can be seen in Figures 5.17(a)-5.17(f). The sum of the  $\theta$  and  $\phi$  angles from all energies that were detected are shown without using the model of the source geometry in Figures 5.18(a) and 5.18(b), and including the model in Figures 5.18(c) and 5.18(d). Notice, that the angle  $\theta$  is measured from the beam axis pointing upstream from the target (not the beam direction). It should also be noted that the histograms were incremented if the silicon detector detected any energy deposition in the events, so also the backscattered and other background events are included. The detection efficiency of the electrons (in the peak) is higher when the source geometry is not used, but there is about 40% more counts in the total spectrum when the source geometry is included in the simulation. This implies that the physical source creates more background events into the spectra.

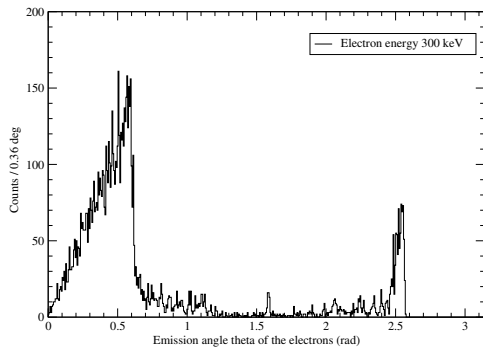
In all cases about 50% of the total number of detected electrons had the emission angle  $\theta$  in the peak on the left-hand side of the distributions of Figures 5.16(a)-5.17(f), 5.18(a) and 5.18(c). This angle corresponds to about  $\theta = 160^\circ$  measured from the beam direction for every energy of the emitted electron. This implies that it would be justified to use this angle as an average angle in the Doppler correction Equation (2.5) to determine the unshifted electron energies from in-beam measurements. The other angle,  $\phi$ , does not have such a preferred angle to be detected as can be seen in Figure 5.18(b). By including the source geometry, some structure is formed as can be seen in Figure 5.18(d) where 4 peaks are appearing, but still the distribution remains almost flat. The effect that the source geometry seems to have is not yet fully understood.



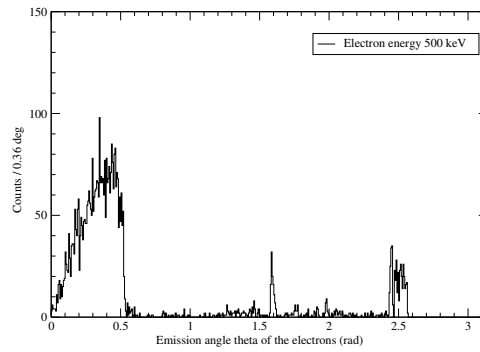
(a) 25 keV



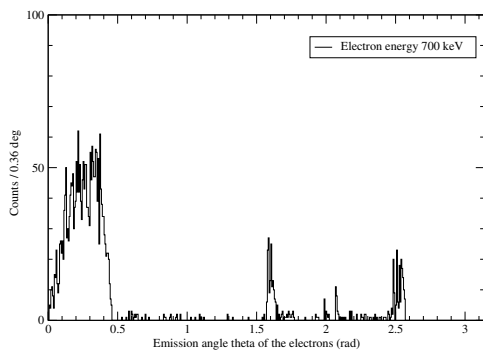
(b) 100 keV



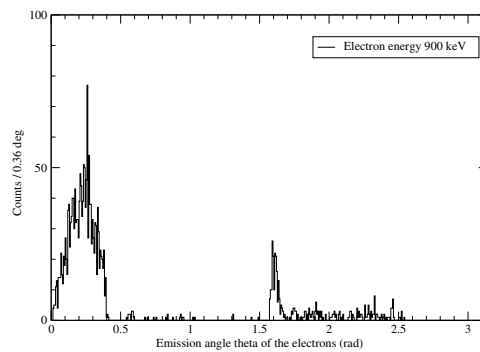
(c) 300 keV



(d) 500 keV

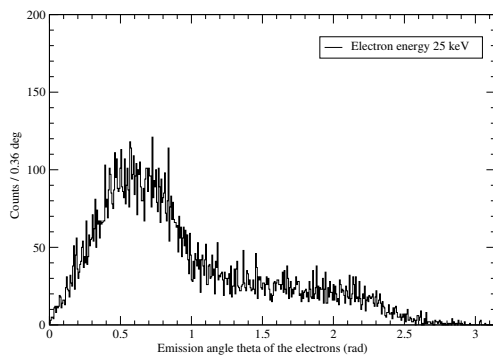


(e) 700 keV

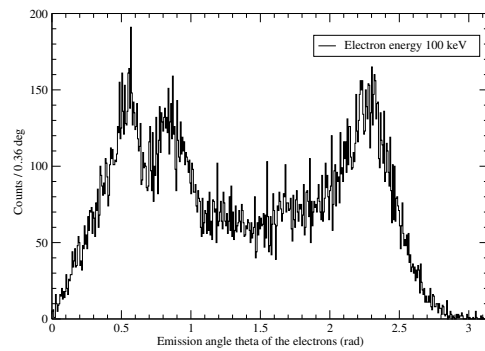


(f) 900 keV

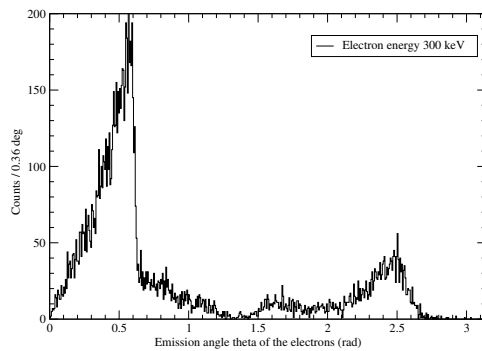
Figure 5.16: The angular distributions of the detected electrons with initial energies of 25, 100, 300, 500, 700 and 900 keV emitted at the target position. The angle  $\theta$  is the angle between the direction of the emitted electron and the beam axis when pointing towards the SAGE silicon detector chamber. This simulation did not have the source geometry modelled.



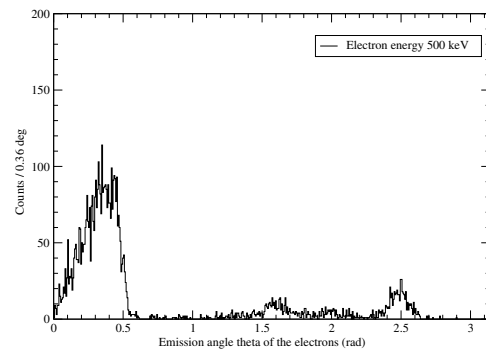
(a) 25 keV



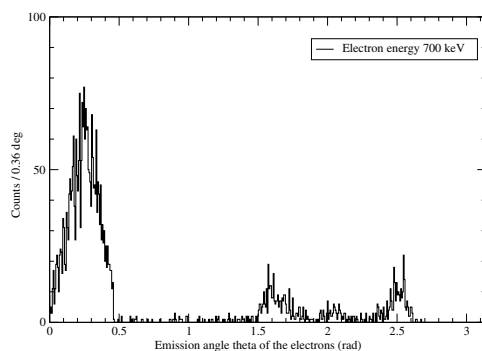
(b) 100 keV



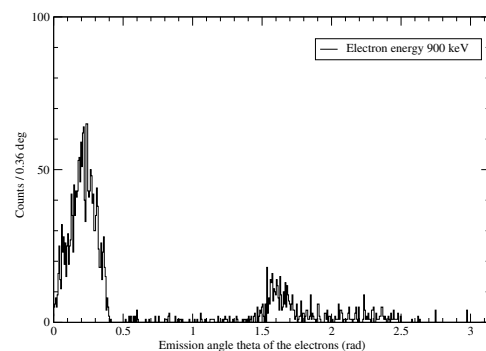
(c) 300 keV



(d) 500 keV

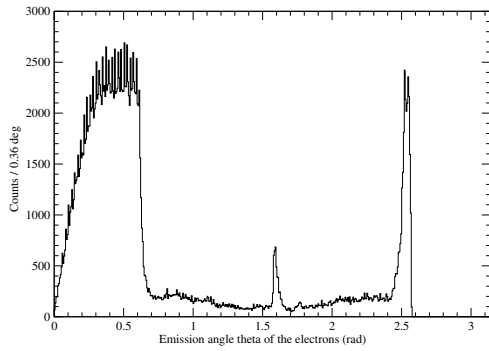


(e) 700 keV

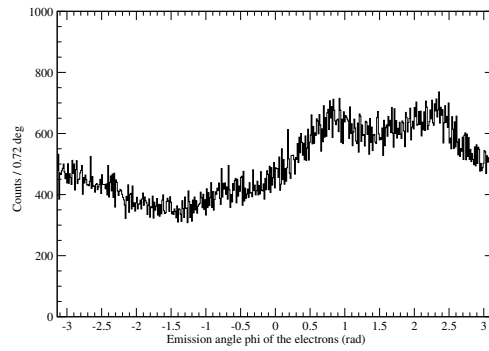


(f) 900 keV

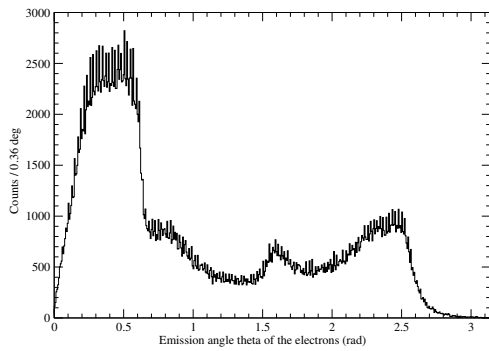
Figure 5.17: The angular distributions of the detected electrons with initial energies of 25, 100, 300, 500, 700 and 900 keV emitted at the target position. The angle  $\theta$  is the angle between the direction of the emitted electron and the beam axis when pointing towards the SAGE silicon detector chamber. This simulation had the source geometry modelled.



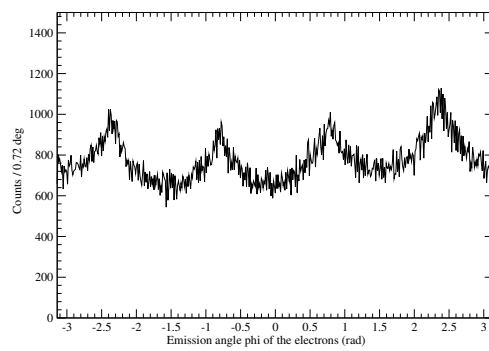
(a) Sum of angles  $\theta$ , no source



(b) Sum of angles  $\phi$ , no source



(c) Sum of angles  $\theta$ , source



(d) Sum of angles  $\phi$ , source

Figure 5.18: Sum of the angular distributions of the detected electrons with initial energies of 25–1000 keV in 25 keV steps emitted at the target position. The angle  $\theta$  is the angle between the direction of the emitted electron and the beam axis when pointing towards the SAGE silicon detector chamber. The upper figures are without the source geometry modelled, the lower ones with.



## 5.8 Simulated detection efficiencies of 0-1000 keV electrons

In the Geant4 simulation package of SAGE, it is easy to estimate how changes in the geometry and different field settings affect the electron transport and detection efficiency of the spectrometer. A few examples of the simulations of the absolute electron detection efficiencies that have been performed are presented here.

Simulated electron detection efficiency curves are presented in Figure 5.19, where the coil current used in the field simulations was 1000 and 800 A and the voltage at the HV barrier was  $-30$  kV. The carbon foil unit was placed inside the target chamber. In the Geant4 simulation, He at 1 mbar pressure was placed in a volume inside the target chamber. The efficiency curve obtained using the SOLENOID code [2] is presented for comparison (1000 A and  $-30$  kV was used). The curves deviate quite a lot from each other, even though the conditions should be similar. The results agree only at around 300 keV. At higher energies the Geant4 simulation gives about 1-2% less efficiency than the other code. At low energies the curve from Geant4 is quite high at around 100-200 keV, but the values have high error bars, due to the method of determining the peak areas. An integral over a 5 keV area around the peaks was used, but at low energies the peaks can be wide and have a lot of background, which was not subtracted. This analysis method will give slightly higher efficiencies than are actually possible to achieve, but the simulations are supposed to give an upper limit for the efficiency. The low-energy efficiency is worse in a real experiment due to e.g. losses in the target material, which were not included in these simulations.

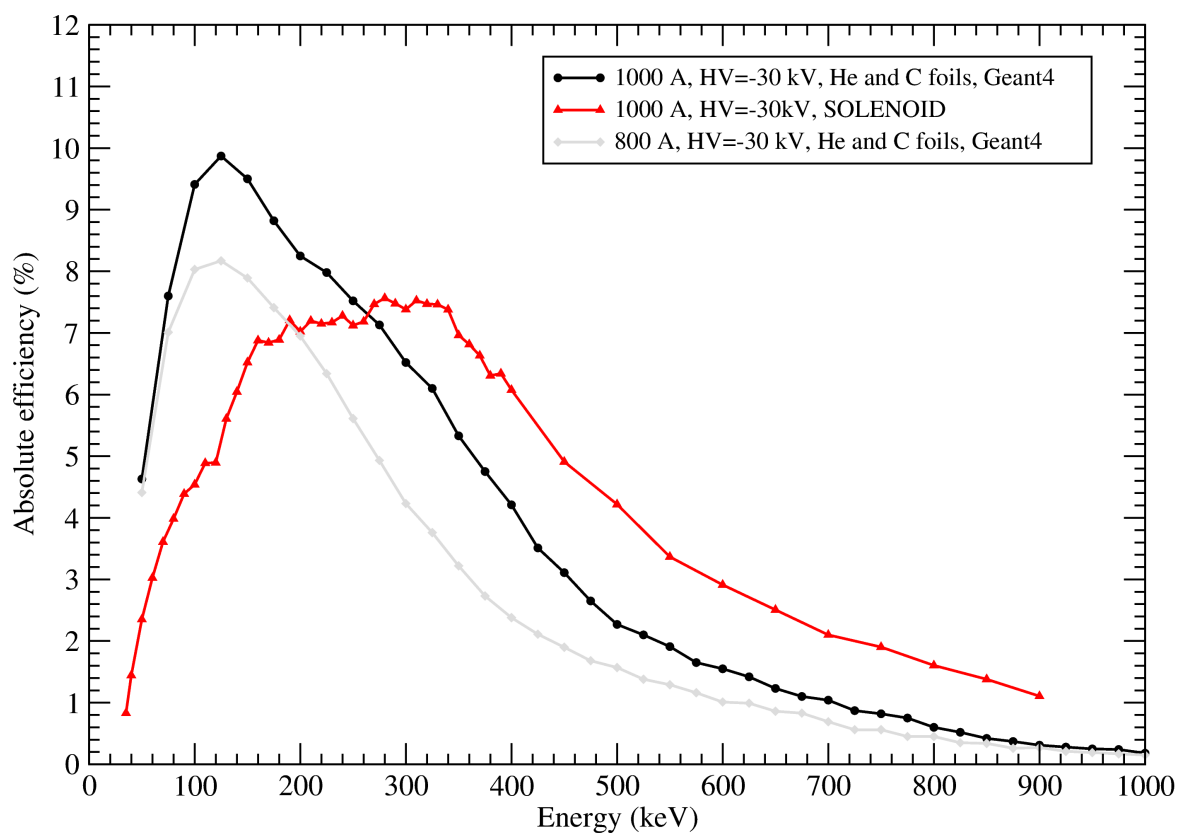


Figure 5.19: The simulated electron detection efficiencies for the coil currents 1000 and 800 A and  $-30$  kV at the HV barrier including He and CF unit in the target chamber from Geant4. The efficiency curve obtained from the SOLENOID code is presented for comparison.

Sum spectra of all the silicon pixels from a measurement of  $^{133}\text{Ba}$  source showing the effect of the electric current in the coils on the electron detection efficiency at 200-300 keV for the coil currents 700, 800, 850 and 900 A can be seen in Figure 5.20. The HV barrier was not used in these measurements. The overlaid spectra indicate an increase in efficiency when the current in the solenoid coils is increased from 700 to 800 A, and after that there is no dramatic increase in the efficiency. However, at low energies, this effect is reversed as can be seen in Figure 5.21, where the low-energy part of the spectra are overlaid. In that case, the lowest current gives the highest efficiency at 45 keV. The distribution was not perfectly centred at the detector in the measurements, but the same measurement time was used in all of them to make them directly comparable.

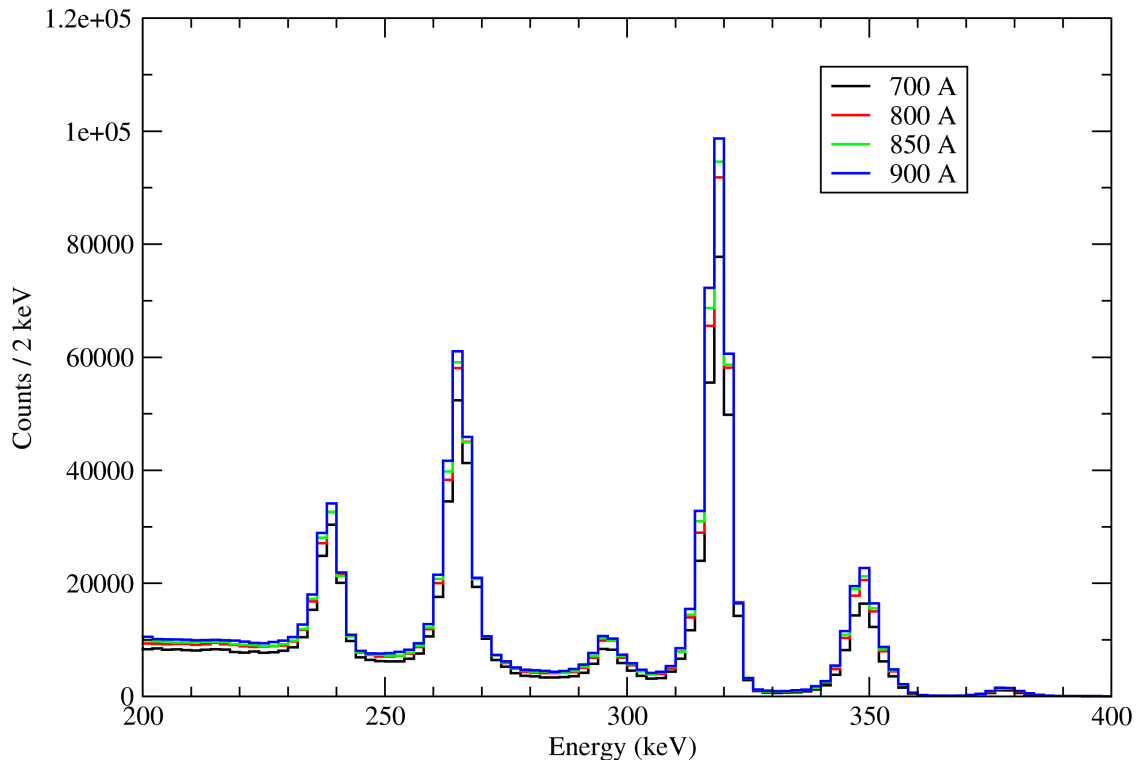


Figure 5.20: The measured  $^{133}\text{Ba}$  spectra for coil currents of 700, 800, 850 and 900 A, demonstrating the effect on the electron detection efficiency.

The behaviour of the efficiency to produce measured spectra in Figure 5.20 and to some extent the reverse effect in Figure 5.21 can be easily explained with simulated efficiency curves presented in Figure 5.22. In the simulation, the efficiency for detecting 300 keV electrons is about the same when using 850 and 900 A in the coils, but lower for 700 and 750 A. For higher energies than 300 keV and up to about 900 keV, the simulations suggest an increase in efficiency for higher currents. On the contrary, for the lower energies at around 75 keV, a lower current in the coils can produce a somewhat higher detection efficiency. 100 000 events per each energy in each field simulation were used.

Essentially, the transmission efficiency has to be calculated separately for every SAGE experiment, because it depends on the thickness of the target material, the carbon foils, vacuum and helium pressure conditions, recoil energy, electron emission angles, Doppler shift and the settings that are used for the magnetic and electric fields.

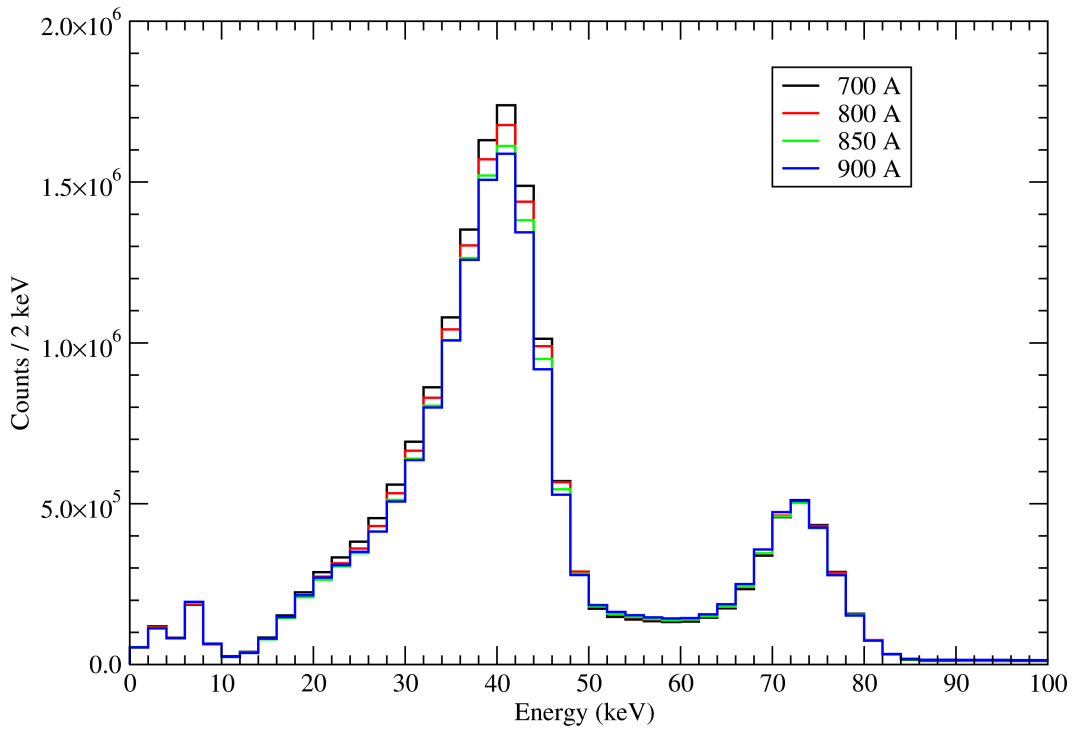


Figure 5.21: The low-energy part of the measured  $^{133}\text{Ba}$  spectra for coil currents of 700, 800, 850 and 900 A, demonstrating the effect on the electron detection efficiency.

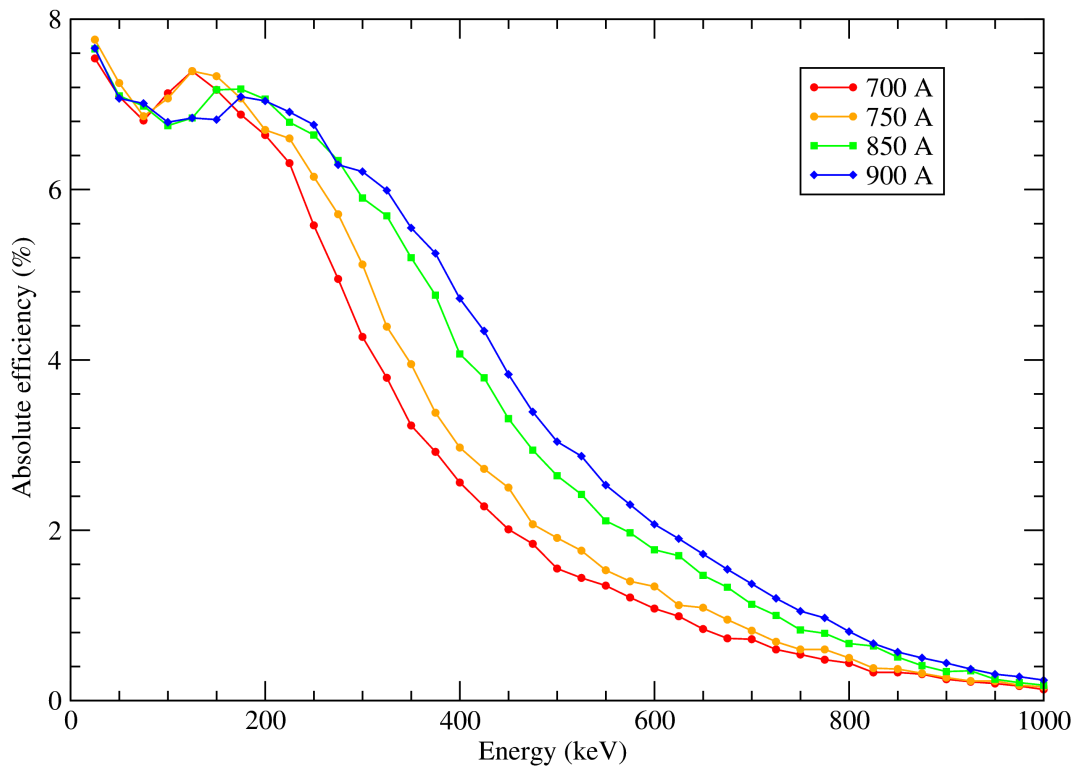


Figure 5.22: The simulated electron detection efficiency curves for coil currents of 700, 750, 850 and 900 A.

## 5.9 Examples of simulated spectra using realistic detector energy resolutions

The validity of the Geant4 simulation and the models of physics processes can be tested by comparing the measured  $^{133}\text{Ba}$  source spectra to the spectra obtained from simulations. Such a comparison is presented in Figure 5.23. Both of the spectra were taken from the same detector pixel that is indicated in the figure (pixel 69). This pixel was the highest counting pixel in both the measurement and the simulation due to the off-centred electron distribution. In this measurement the current in the solenoid coils was 750 A and the HV barrier was not used. The intrinsic resolution of the detector was considered to be 4 keV in the analysis of the simulation data, to make the peaks more realistic. The two spectra were normalised with respect to the area of the 320 keV peak, by scaling up the simulated spectrum. In this case the scaling factor was about 42. The normalisation has to be done, because the calculation time of a full length measurement of tens of minutes takes a very long time. The overall agreement between the spectra is very good considering the peaks and energies, but the background in the tails of the peaks is higher on the measured one. This could mean that the amount of backscattering is underestimated in the simulation, or the intensities of the simulated decay scheme are incorrect, because the peak efficiencies are quite well reproduced by the simulation. At lower energies, the measured spectrum again shows much more background than the simulated one, which makes the 45 keV peak appear much wider.

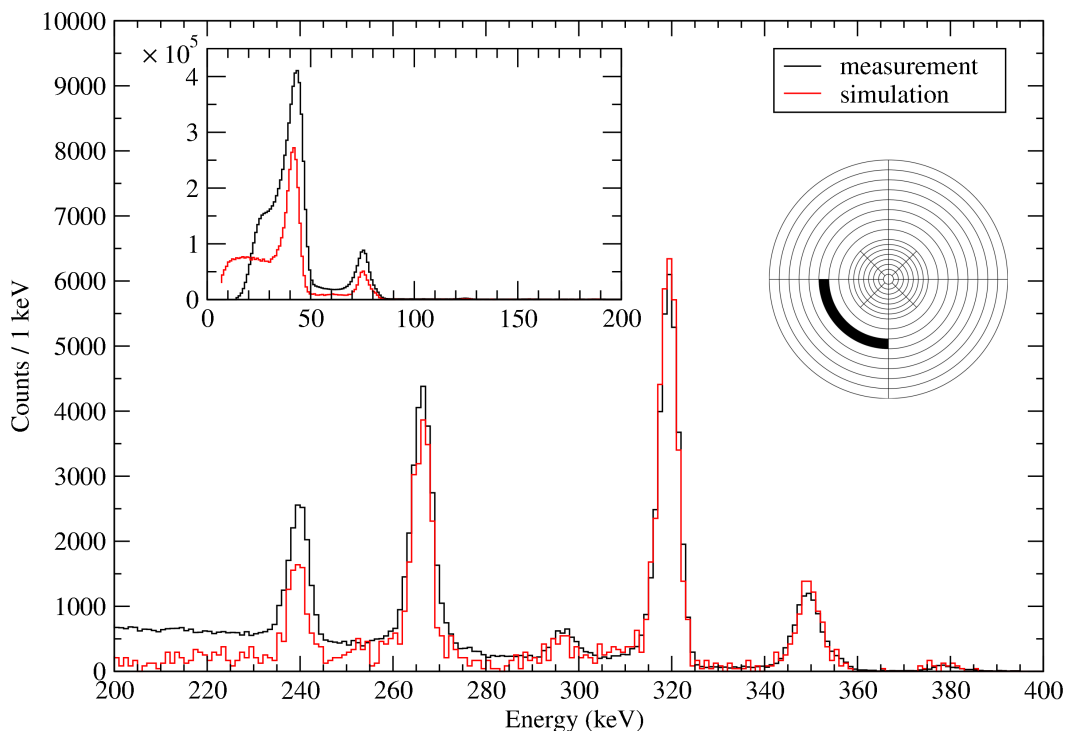


Figure 5.23: A comparison of the measured (black) and simulated (red)  $^{133}\text{Ba}$  spectra obtained from the same detector pixel, which is marked in the diagram of the detector pixels on the right. The insert shows the low energy peaks.

As an example of a long simulation run, a sum spectrum from a simulation of a  $^{133}\text{Ba}$  source using 750 A current in the coils without the HV barrier and no helium or carbon

foils in the target chamber is shown in Figure 5.24. An intrinsic detector resolution of 4 keV was applied to the deposited energies in the analysis phase to the simulation data. A total of  $91.43 \cdot 10^6$  events of  $^{133}\text{Ba}$  decays were simulated and the total calculation time was 4-5 days using the low-energy electromagnetic physics list. This number of events roughly corresponds to a 10 minute real measurement of the open  $^{133}\text{Ba}$  source (JYFL-90). The measurement data in the plot is from a run with 800 A in the coils (Run50), and was normalised down to match the simulated spectrum using the 320 keV peak. The resolution in the simulated spectrum is better than in the measured spectrum, making the peaks appear slightly taller than in the measured one. It can be seen from the insert that there are more peaks appearing at the low energies in the simulated spectrum below the 45 keV peak, that are not visible in the measured spectrum. These are e.g. low-energy Auger electrons from  $^{133}\text{Cs}$ , that do not appear in the measured spectra because of noise and background that make the resolution and efficiency worse at very low energies. As in Figure 5.23, the backscattering could be greatly underestimated in Geant4 using the same arguments as before. However, at very low energies, the tail is much higher in the simulation with the low-energy electromagnetic physics list enabled than in Figure 5.23 or from the measurement. In the measurement, the thresholds and gains set to the channels do not allow the low-energy tail to form. Some of the pixels only show a small peak at energies lower than 45 keV, in both the measurements and the simulations. These pixels can not be usually calibrated properly. The low-energy peaks at 45 keV and 75 keV in the simulation appear to be higher than in the measurement, because of the better energy resolution in them.

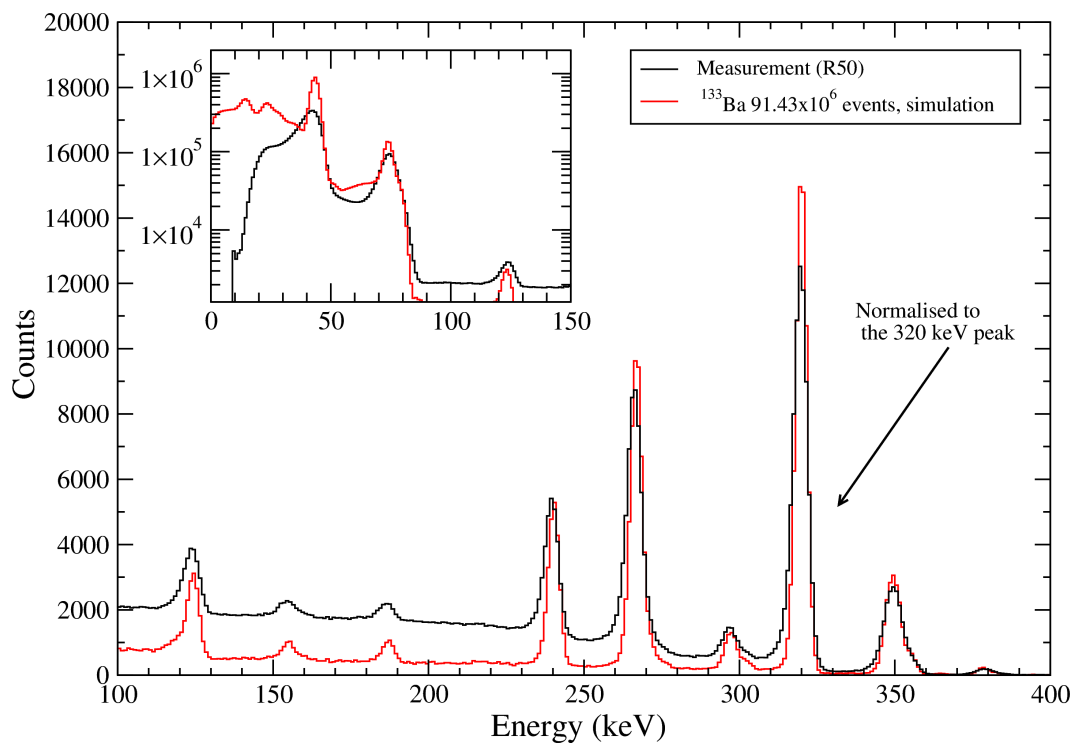


Figure 5.24: Sum spectrum of all the silicon pixels from a simulated  $^{133}\text{Ba}$  source using  $91.43 \cdot 10^6$  events with an intrinsic resolution of 4 keV applied and compared to a measurement by normalising the 320 keV peak areas. In the simulation the current in the coils was 750 A, HV barrier was off and no CF unit was used. The insert shows the low energy peaks on a logarithmic scale.



# 6

## Conclusions

An extensive set of measurements and demanding simulations have been performed to determine the performance characteristics of the combined electron and gamma-ray spectrometer SAGE. The electron detection efficiency of the SAGE spectrometer was successfully determined in this work from direct measurements of an open  $^{133}\text{Ba}$  electron source. During the testing phase in July 2011, it was shown that the magnetic field produced by the solenoid coils does not affect the performance of the photomultiplier tubes used in the Compton suppression shields of the Phase 1 germanium detectors, and the peak-to-total ratios remain the same when using the electron transport system of SAGE.

In the re-commissioning runs in October-November 2011, it was shown that the high-voltage barrier is working by seeing a clear suppression of the low-energy electrons from the barium source when a high-voltage is applied to the barrier. Unfortunately, something causes discharges at the barrier, because it was not possible to reach the designed  $-50$  kV voltage without clear signs of discharges appearing as a deterioration of the energy resolution of the silicon detector, because the discharging affects the baseline. However, voltages of around  $-35$  kV were used successfully in some of the source measurements and during in-beam runs of, for example,  $^{16}\text{O}$  beam on  $^{170}\text{Er}$  target,  $^{16}\text{O}$  on  $^{208}\text{Pb}$  and  $^{36}\text{Ar}$  on  $^{144}\text{Sm}$ . Helium and the carbon foil unit were also successfully used in the target chamber to enable the use of RITU and GREAT to detect the recoil nuclei.

A complete simulation package for the SAGE spectrometer was developed in a small group consisting of mostly people working with SAGE using the Geant4 simulation toolkit. The simulation package combines for the first time the JUROGAM II array of germanium detectors and their BGO Compton suppression shields with the electron transport and detection part in the same simulation. The simulation package was shown to give reasonable results right from the start by predicting the result concerning the slightly off-centred electron distribution (which was already known from the measurements of the previous tests). The simulation was also used to determine electron and gamma-ray detection efficiencies using various settings for the fields and geometry by employing the well-known Monte Carlo methods. Overall, the results agree very well with the measured data, but there are small differences here and there. Measurements of a radioactive source with internal conversion electron energies above  $400$  keV should be made to verify the behaviour of the simulated efficiency curve at higher energies. The data analysis methods of the simulation data should be made similar to the actual measurements if the results are expected to be nearly identical, but that will make the analysis of the simulation data slower and uncertainties will be higher. Everything has not been included in the simulation geometry, but on the other hand, it will never be possible to reproduce every single nut and bolt and the deviations that exist in the setup. The validity of the simulations are clear, but improvements and fine-tuning are needed in the future developments of the code.

The gamma-ray detection efficiency of JUROGAM II was determined in this work for a handful of useful energies using the activity method and calibrated  $^{133}\text{Ba}$  and  $^{60}\text{Co}$  point sources. The efficiency of the array obtained using the activity method, 4.4% at 1.3 MeV is lower than the usually reported value that is determined using the sum-peak method (5.5-6.0% for the full array). The activity method does not eliminate the effects of dead time, pile-up and other effects. The efficiencies obtained from the simulations are higher than the measured values using the activity method, but a better agreement could be reached if the sum-peak method is used to determine the measured efficiency.

The peak-to-total ratios of all the JUROGAM II germanium detectors and efficiencies using the activity method were determined individually with and without using the veto signals from the Compton suppression shields in a measurement of a  $^{60}\text{Co}$  source. This kind of analysis of the performance of the JUROGAM II array has not been done properly for a long time. A possible drop in performance of both the Phase 1 and Clover BGO shields was seen when compared to other values given for the EUROGAM PHASE I & II arrays in the past. The reason for this can be the ageing of the PMTs or the BGO crystals or the current settings used in the electronics for the BGO vetoes. A careful check and analysis of the PMT tubes, electronics settings and data acquisition should be made to verify the performance of the Compton suppression shields of the JUROGAM II array as soon as possible.

Until now, the simulation package has been mainly used to simulate offline measurements of radioactive sources. More simulations are needed, especially with the HV barrier on and using helium and the CF unit in the target chamber. Furthermore, the ultimate purpose of the SAGE simulation package is to be able to estimate and predict results from real in-beam experiments. More development of the simulation package is needed to make it possible. This includes adding Doppler shifts to the electron energies that are emitted from a moving recoil nucleus, better coincidence summing with a true sense of time by using timestamping of the events, adding false vetoes, adjusting the BGO shield veto efficiencies to match the measured peak-to-totals, production of delta-electrons and adding the possibility to read-in simple user created level and decay schemes. The model of the simulation geometry should be further improved by including the large steel support structure of JUROGAM II that causes Compton scattering of gamma rays, the target material that causes energy-losses for the electrons and alters the angular distributions of the detected electrons and the Cu and Ni foils in front of the germaniums that suppress X-rays.

When the simulation package can be used to estimate results that are obtained from in-beam experiments, another verification of the simulated results should be made by comparing to a fusion-evaporation reaction of nuclei with a high production cross-section, well-known level schemes and highly converted transitions in a reasonable energy range of 100-1000 keV. The verification should also be made using electron-gamma, gamma-gamma, electron-gamma-gamma and electron-electron-gamma coincidences. Only in this way, can the simulation code be verified to produce reliable results and predictions of new and exciting in-beam experiments in the future.



# References

- [1] P. Papadakis et al. Towards combining in-beam gamma-ray and conversion electron spectroscopy. *AIP Conference Proceedings*, 1090(1):14–20, 2009.
- [2] P. A. Butler et al. Electron spectroscopy using a multi-detector array. *Nuclear Instruments and Methods in Physics Research A*, 381(2-3):433–442, 1996.
- [3] H. Kankaanpää et al. In-beam electron spectrometer used in conjunction with a gas-filled recoil separator. *Nuclear Instruments and Methods in Physics Research A*, 534:503–510, 2004.
- [4] M. Leino et al. Gas-filled recoil separator for studies of heavy elements. *Nuclear Instruments and Methods in Physics Research B*, 99:653–656, 1995.
- [5] R. D. Page et al. The GREAT Spectrometer. *Nuclear Instruments and Methods in Physics Research B*, 204:634–637, 2003.
- [6] S. Agostinelli et al. Geant4—a simulation toolkit. *Nuclear Instruments and Methods in Physics Research A*, 506:250–303, 2003.
- [7] Vector Fields. Opera version 12. [www.vectorfields.com](http://www.vectorfields.com) [cited November 8, 2011].
- [8] P. Papadakis, D. M. Cox, **J. Konki**, et al. A Geant4 simulation package for the SAGE spectrometer. To be published in the conference proceedings of the Rutherford Centennial Conference on Nuclear Physics 2011, *Journal of Physics: Conference Series (JPCS)*.
- [9] J. Kantele. *Handbook of Nuclear Spectrometry*. Academic Press, Great Britain, 1995.
- [10] H. R. Hulme. The Internal Conversion Coefficient for Radium C. *Proceedings of the Royal Society A*, 138:643–664, May 1932.
- [11] J. Sarén et al. Absolute transmission and separation properties of the gas-filled recoil separator RITU. *Nuclear Instruments and Methods in Physics Research A*, 654:508–521, 2011.
- [12] C. Kelbch et al. Delta-electron emission in fast heavy ion - atom collisions: observations of new phenomena and breakdown of common scaling laws. *Zeitschrift fur Physik D: Atoms, Molecules and Clusters*, 22:713–721, 1992.
- [13] H. Schmidt-Böcking et al.  $\delta$ -electron emission in fast heavy ion atom collisions. *Advances in space research*, 12(2–3):(2)7–(2)15, 1992.
- [14] N. Stolterfoht et al. *Electron Emission in Heavy Ion-Atom Collisions*. Springer-Verlag, Berlin, 1997.
- [15] U. Bechthold et al. Intra-atomic double scattering of binary encounter electrons in collisions of fast heavy ions with atoms and molecules. *Physical Review Letters*, 79, 1997.
- [16] D. Griffiths. *Introduction to Quantum Mechanics*. 2<sup>nd</sup> edition, 2005.
- [17] S. Eeckhaudt et al. In-beam gamma-ray spectroscopy of  $^{254}\text{No}$ . *The European Physical Journal A - Hadrons and Nuclei*, 25:605–607, 2005.

- [18] S. Eeckhaudt. *Spectroscopy in the transfermium region : probing rotational, non-yrast and isomeric structures in  $^{253,254}\text{No}$* . PhD thesis, Department of Physics, University of Jyväskylä, 2006.
- [19] Geant4 Physics Reference Manual, version 9.4. <http://geant4.cern.ch> [cited November 15, 2011].
- [20] J. R. Reitz, J. F. Milford, and R. W. Christy. *Foundations of Electromagnetic Theory*, 4<sup>th</sup> edition. Addison-Wesley, USA, 1993.
- [21] R. J. Goldston and P. H. Rutherford. *Introduction to Plasma Physics*. Institute of Physics Publishing, Bristol, UK, 2000.
- [22] J. R. Taylor. *An Introduction to Error Analysis*, 2<sup>nd</sup> edition. University Science Books, CA, USA, 1997.
- [23] C. W. Beausang et al. Measurements on prototype Ge and BGO detectors for the Eurogam array. *Nuclear Instruments and Methods in Nuclear Physics Research A*, 313:37–49, 1992.
- [24] G. Duchêne et al. The Clover: a new generation of composite Ge detectors. *Nuclear Instruments and Methods in Nuclear Physics Research A*, 432:90–110, 1999.
- [25] F. A. Beck. EUROBALL: Large gamma ray spectrometers through european collaborations. *Progress in Particle and Nuclear Physics*, 28:443–461, 1992.
- [26] J. Eberth and J. Simpson. From Ge(Li) detectors to gamma-ray tracking arrays — 50 years of gamma spectroscopy with germanium detectors. *Progress in Particle and Nuclear Physics*, 60:283–337, 2008.
- [27] P. Papadakis. *Combining in-beam  $\gamma$ -ray and conversion electron spectroscopy*. PhD thesis, University of Liverpool, 2010.
- [28] J. Uusitalo et al. In-beam spectroscopy using the JYFL gas-filled magnetic recoil separator RITU. *Nuclear Instruments and Methods in Physics Research B*, 204:638–643, 2003.
- [29] J. Sarén. RITU:n kehittäminen ja kaasutäytteisiin separaattoreihin liittyvää ionioptiikkaa. Master's thesis, Jyväskylän yliopisto, fysiikan laitos, 2004.
- [30] K.-H. Schmidt et al. Gamma-spectroscopic investigations in the radiative fusion reaction  $^{90}\text{Zr} + ^{90}\text{Zr}$ . *Physics Letters B*, 168(1-2):39–42, 1986.
- [31] E. S. Paul et al. In-beam  $\gamma$ -ray spectroscopy above  $^{100}\text{Sn}$  using the new technique of recoil decay tagging. *Phys. Rev. C*, 51:78–87, 1995.
- [32] W. Korten and the JUROSPHERE collaboration. In-beam Spectroscopy of Exotic Nuclei using Recoil-Decay-Tagging. *Nuclear Physics A*, 654:677c–686c, 1999.
- [33] I. H. Lazarus et al. The GREAT Triggerless Total Data Readout Method. *IEEE Transactions on Nuclear Science*, 48:567–569, 2001.
- [34] P. Rahkila. Grain — A Java data analysis system for Total Data Readout. *Nuclear Instruments and Methods in Physics Research A*, 595:637–642, 2008.

- [35] A. Georgiev and W. Gast. Digital pulse processing in high resolution, high throughput, gamma-ray spectroscopy. *IEEE Transactions on Nuclear Science*, 40(4):770–779, 1993.
- [36] A. Georgiev, W. Gast, and R.M. Lieder. An analog-to-digital conversion based on a moving window deconvolution. *IEEE Transactions on Nuclear Science*, 41(4):1116–1124, 1994.
- [37] M. Lauer. *Digital Signal Processing for segmented HPGe Detectors Preprocessing Algorithms and Pulse Shape Analysis*. PhD thesis, Ruperto-Carola University of Heidelberg, Germany, 2004.
- [38] J. Eberth et al. MINIBALL – a Ge detector array for radioactive ion beam facilities. *Progress in Particle and Nuclear Physics*, 46:389–398, 2001.
- [39] J. F. Ziegler, M. D. Ziegler, and J. P. Biersack. SRIM – the stopping and range of ions in matter (2010). *Nuclear Instruments and Methods in Physics Research B*, 268(11–12):1818–1823, 2010. 19th International Conference on Ion Beam Analysis.
- [40] J. Allison et al. Geant4 developments and applications. *IEEE Transactions on Nuclear Science*, 53(1):270–278, 2006.
- [41] P. Rodrigues et al. Geant4 applications and developments for medical physics experiments. In *Nuclear Science Symposium Conference Record, 2003 IEEE*, volume 3, pages 1751–1755, 2003.
- [42] A. Lechner and V. Ivanchenko. Recent developments of electronic stopping models for heavy ions in Geant4. In *Nuclear Science Symposium Conference Record, 2008. NSS '08. IEEE*, pages 837–840, 2008.
- [43] A. Lechner, M. G. Pia, and M. Sudhakar. Validation of Geant4 low energy electromagnetic processes against precision measurements of electron energy deposition. *IEEE Transactions on Nuclear Science*, 56(2):398–416, 2009.
- [44] K. Amako et al. Comparison of Geant4 electromagnetic physics models against the NIST reference data. *IEEE Transactions on Nuclear Science*, 52(4):910–918, 2005.
- [45] G. Cosmo. The Geant4 geometry modeler. In *Nuclear Science Symposium Conference Record, 2004 IEEE*, volume 4, pages 2196–2198, 2004.
- [46] General Particle Source module for Geant4. <http://reat.space.qinetiq.com/gps/> [cited November 8, 2011].
- [47] Evaluated Nuclear Structure Data File, National Nuclear Data Center (NNDC). <http://www.nndc.bnl.gov/ensdf/> [cited November 8, 2011].
- [48] P. J. Mohr, B. N. Taylor, and D. B. Newell. The 2010 CODATA recommended values of the fundamental physical constants. National Institute of Standards and Technology (NIST). <http://physics.nist.gov/constants> [cited November 8, 2011].
- [49] S. Chauvie et al. Geant4 low energy electromagnetic physics. In *Nuclear Science Symposium Conference Record, 2004 IEEE*, volume 3, pages 1881–1885, 2004.

- [50] V. V. Golovko, V. E. Jacob, and J. C. Hardy. The use of Geant4 for simulations of a plastic  $\beta$ -detector and its application to efficiency calibration. *Nuclear Instruments and Methods in Physics Research A*, 594:266, 2008.
- [51] M. Capogni et al. Simulation of radioactive decay in GEANT Monte Carlo codes: Comparison between spectra and efficiencies computed with sch2for and G4RadioactiveDecay. *Applied Radiation and Isotopes*, 68:1428–1432, 2010.
- [52] W. H. Press. *Numerical Recipes in C – The Art of Scientific Computing*, 2<sup>nd</sup> edition. Cambridge University Press, CA, USA, 1997.
- [53] AIDAJNI adapter package for C++. <http://java.freehep.org/aidajni/> [cited November 15, 2011].
- [54] JAIDA, a Java implementation of the Abstract Interfaces for Data Analysis – AIDA. <http://java.freehep.org/jaida/> [cited November 15, 2011].
- [55] D. C. Radford. ESCL8R and LEVITSR: Software for interactive graphical analysis of HPGe coincidence data sets. *Nuclear Instruments and Methods in Physics Research A*, 361:297–305, 1995.
- [56] D. C. Radford. Radware – a software package for interactive graphical analysis of gamma-ray coincidence data. Physics Division, Oak Ridge National Laboratory, <http://radware.phy.ornl.gov/> [cited November 15, 2011].
- [57] S. H. Byun et al. Efficiency calibration and coincidence summing correction for a  $4\pi$  NaI(Tl) detector array. *Nuclear Instruments and Methods in Physics Research A*, 535:674–685, 2004.
- [58] T. Vidmar et al. Close-geometry efficiency calibration in gamma-ray spectrometry using radio-nuclides with a two-step cascade decay. *Nuclear Instruments and Methods in Physics Research A*, 508:404–413, 2003.
- [59] G. A. Brinkman et al. Absolute Standardization with a NaI(Tl) Crystal-I. *International Journal of Applied Radiation and Isotopes*, 14:153–157, 1963.
- [60] I. J. Kim et al. Absolute calibration of  $^{60}\text{Co}$  by using sum-peak method and an HPGe detector. *Applied Radiation and Isotopes*, 58:227–233, 2003.
- [61] T. Vidmar et al. Application of the sum-peak method to activity standardizations of extended  $^{60}\text{Co}$  sources. *Applied Radiation and Isotopes*, 67:160–163, 2009.
- [62] R. B. Firestone et al. *Table of Isotopes CD-ROM*. John Wiley & Sons, Inc., 8th edition, 1996.
- [63] W. H. Trzaska. Recommended data on selected gamma-ray and conversion-electron calibration sources. *Nuclear Instruments and Methods in Physics Research A*, 297:223–229, 1990.
- [64] G. A. Warren et al. Determining activities of radionuclides from coincidence signatures. *Nuclear Instruments and Methods in Physics Research A*, 560:360–365, 2006.
- [65] C. Hurtgen, S. Jerome, and Woods M. Revisiting currie — how low can you go? *Applied Radiation and Isotopes*, 53:45–50, 2000.

- [66] C. W. Beausang and J. Simpson. Large arrays of escape suppressed spectrometers for nuclear structure experiments. *Journal of Physics G: Nuclear and Particle Physics*, 22:527–558, 1996.
- [67] J. Eberth et al. Development of a composite Ge detector for EUROBALL. *Progress in Particle and Nuclear Physics*, 28:495–504, 1992.